

2016/07/18
 Head Id: 356418
 Archive Id: 356524
 Archive Date: 2016/07/17
 Archive Tag: trunk

Search for new physics in the diphoton spectrum at high mass at 13 TeV (2016 data)

D. Anderson¹, J. Bendavid¹, A. Beschi², A. Buccilli³, O. Charaf³, V. Ciriolo², S. Cooper³, L. Corpe⁴, M. Donegà⁵, G. Fasanella⁷, F. Ferri⁸, C. Henderson³, B. Marzocchi⁶, M. Machet⁸, M. Malcles⁸, M. Malberti², P. Meridiani⁶, P. Musella⁵, S. Nourbakhsh⁹, R. Paramatti⁶, C. Pena¹, S. Pigazzini², M. Quitnat⁵, C. Rovelli⁶, P. Rumerio³, L. Soffi¹⁰, T. Tabarelli de Fatis², J. Wright⁴, S. Xie¹, Z. Zhang¹, and S. Zenz⁴

¹ Caltech

² Università di Milano Bicocca and INFN

³ University of Alabama

⁴ Imperial College London

⁵ ETH Zurich

⁶ Università La Sapienza Rome and INFN

⁷ INFN-Rome and Université libre de Brussels

⁸ CEA Saclay

⁹ University of Minnesota

¹⁰ Cornell University

Abstract

We describe the search for new physics in the diphoton invariant mass spectrum using the data collected in 2016 at $\sqrt{s} = 13$ TeV by the CMS experiment. Excesses for events compatible with the resonant production of two photons are searched for. The results are interpreted in term of spin0 or spin2 resonances.

This box is only visible in draft mode. Please make sure the values below make sense.

PDFAuthor:

Various authors

PDFTitle:

Search for new physics in the diphoton spectrum at high mass at 13 TeV
 "(2016 data")

PDFSubject:

CMS

PDFKeywords:

CMS, physics, software, computing

Please also verify that the abstract does not use any user defined symbols

1 Contents

2	1	Introduction	3
3	2	Data and MC samples	4
4	2.1	Analyzed data	4
5	2.2	Monte Carlo samples	4
6	3	Event selection	7
7	3.1	Trigger selection	7
8	3.2	Events preselection	9
9	3.3	Photon identification and isolation requirements	10
10	4	Selected sample	13
11	4.1	Comparison with 2015 results	13
12	5	Energy scale and resolution corrections	16
13	5.1	Scale uncertainty related to the energy extrapolation	18
14	6	Selection efficiency control from data	24
15	7	Background composition control from data	33
16	8	Parametric Signal Model	42
17	8.1	Parametric Signal Shape comparison 76X/80X	44
18	8.2	Expected limits comparison with and without the parametric signal model	44
19	9	Non-parametric Signal Model	49
20	10	Background model	52
21	10.1	Background parametrization and bias estimation	52
22	10.2	Inclusion of bias term in hypothesis testing	59
23	11	Systematic uncertainties	62
24	12	Alternative Analysis	63
25	13	Results	66
26	14	Conclusions	69
27	A	Combination with previous results	70
28	B	Control plots for luminosity top-up to 7.6 fb^{-1}	73
29	C	Comparison of control plots with 2015 results	76
30	D	Comparison between the first 2.6 fb^{-1} the subsequent 1.4 fb^{-1}	81
31	E	Analysis optimization studies	83
32	E.1	Photon ID MVA	83
33	E.2	Spin Studies	83
34	F	Further studies on the background model accuracy	86
35	F.1	Alternative background parametrization	86
36	F.2	Alternative bias parametrization	86
37	G	Systematic uncertainties for the background control	89
38	G.1	Closure in Monte-Carlo dataset	89
39	G.2	Bias of templates construction due to statistical limitations	89
40	G.3	Systematic error on background fractions	90
41	H	Discrete profiling method for background modelling	92
42	H.1	Introduction to the discrete profiling or ‘envelope’ method	92
43	H.2	Alternative bias study	94

44	H.3 Conclusions about the use of the Envelope method	95
----	----------------------------------------------------------------	----

DRAFT

45 1 Introduction

- 46 The resonant production of high mass diphoton pairs is a generic prediction of several exten-
 47 sions of the Standard Model (SM). From very general assumptions [1, 2], the spin of a resonance
 48 decaying to two photons can be restricted to be either 0 or an integer greater or equal to 2. The
 49 production of heavy scalar resonances decaying to two photons is predicted by SM extensions
 50 with non-minimal Higgs sectors, while the production of spin-2 resonances is predicted by
 51 models postulating the existence of additional space-like dimensions.
- 52 Theories that introduce additional space-like dimensions provide an approach to solve the so-
 53 called hierarchy problem, which has its origin in the large difference between the scale of the
 54 electroweak and of the gravitational interactions. The existence of additional dimensions has
 55 the effect of ‘diluting’ gravity and thus allows lowering of the scale of the gravitational interac-
 56 tion and avoidance of the hierarchy problem. Two families of models, introduced by Arkani-
 57 Hamed, Dimopoulos and Dvali (ADD) [3], and by Randall and Sundrum (RS) [4] have been
 58 developed. We use the RS model as a reference model for the spin-2 part of the results dis-
 59 cussed here. It postulates the presence of two brane-worlds and the SM fields are allowed to
 60 propagate in only one of the two. The further assumption of a warped space-time metric al-
 61 lows the difference between the electroweak and Planck scales to be accounted for. From the
 62 phenomenological point of view, it predicts that the excitations of the gravitational field lead
 63 to ‘towers’ of spin-2 resonances, commonly denoted as gravitons, separated by a characteristic
 64 mass scale [5–9]. Such mass separation is large enough to allow the independent observation
 65 of each resonance.
- 66 The simplest extension of the SM Higgs sector consists in the addition of a second doublet of
 67 scalar fields to the theory. Models of this kind, known as two-Higgs-doublet models (2HDM) [10]
 68 feature the presence of a total of five scalar or pseudo-scalar resonances in the spectrum of the
 69 theory. Identifying one of the scalars as the 125 GeV Higgs boson discovered by the CMS and
 70 ATLAS collaborations [11, 12], and assuming that its couplings correspond to those of the SM
 71 Higgs boson, forces the 2HDM in the so-called alignment limit [13] where some of the addi-
 72 tional resonances can decay to a diphoton pair at a non-negligible rate.
- 73 ATLAS [14] and CMS [15] collaborations reported results on searches for diphoton resonances
 74 at $\sqrt{s} = 13$ TeV, in a large mass range, based on LHC 2015 data. Both analyses reported the
 75 observation of modest deviations from the background-only expectations, compatible with the
 76 resonant production of two photons.
- 77 In this note we describe a search for new physics in the diphoton invariant mass spectrum at
 78 13 TeV. The analysis employs 7.6 fb^{-1} of pp collisions collected by the CMS experiment in 2016
 79 at $\sqrt{s} = 13$ TeV. The analysis strategy is unchanged compared to the analysis of 2015 data. It
 80 makes use of the same HLT path (with a minor addition) and offline photon selection criteria.
 81 The background model is unchanged, but an alternative one is also being tested. A fully-
 82 parametric signal model is now used, and the one from 2015 is kept as a cross-check. Energy
 83 scale and resolution corrections are derived on the 2016 dataset using the same technique as
 84 in 2015. The selection efficiencies and background purities are also re-derived. An end-to-end
 85 cross-check analysis is also run and documented.
- 86 The results of the analysis were unblinded after the pre-approval. In this version of the note we
 87 document the results of the second top-up of the dataset, performed after some basic checks on
 88 the $Z \rightarrow ee$ control region and on some diphoton distributions were passed.

89 2 Data and MC samples

90 2.1 Analyzed data

91 The data considered in this analysis corresponds to an integrated luminosity of 7.6 fb^{-1} col-
 92 lected by the CMS experiment in 2016. Prompt calibration and alignment conditions were used
 93 to reconstruct the used data. The analyzed sample fulfilled standard data quality criteria for all
 94 components of the CMS detector ('golden json')

95 The list of datasets used in the analysis is reported in table 1, together with the corresponding
 96 integrated luminosity. The DoubleEG dataset is used for the nominal analysis. SingleElectron
 97 and SinglePhoton datasets are used for calibrations and background control studies.

Dataset	integrated luminosity
/DoubleEG/Run2016B-PromptReco-v2/MINIAOD	5.9 fb^{-1}
/DoubleEG/Run2016C-PromptReco-v2/MINIAOD	1.8 fb^{-1}
/SingleElectron/Run2016B-PromptReco-v2/MINIAOD	5.9 fb^{-1}
/SingleElectron/Run2016C-PromptReco-v2/MINIAOD	1.8 fb^{-1}
/SinglePhoton/Run2016B-PromptReco-v2/MINIAOD	5.9 fb^{-1}
/SinglePhoton/Run2016C-PromptReco-v2/MINIAOD	1.8 fb^{-1}

Table 1: List of analyzed datasets.

98 2.2 Monte Carlo samples

99 A set of full simulation samples was used to model the detector response to resonant pro-
 100 duction of two photons. Such samples were generated with PYTHIA and are summarized in
 101 table 2. RS gravitons were chosen as a reference for the spin-2 resonance search. SM-like
 102 Higgs bosons of high mass and fixed widths were used for the spin-0 case. For the narrow
 103 width hypothesis the samples were produced with a fine scan in mass:

- 104 • every 5 GeV from 740 GeV to 770 GeV
- 105 • every 250 GeV from 1000 GeV to 4000 GeV
- 106 • every 500 GeV elsewhere from 500 GeV to 7000 GeV

107 while for larger widths a coarser sampling was produced. An additional fine grid of particle-
 108 level event samples was used to model the signal spectrum at generator level and the accep-
 109 tance of the kinematic selections. In this case the signal samples were generated every 150 GeV
 110 in mass and for different couplings of the resonance ($kMpl=0.01, 0.05, 0.07, 0.1, 0.15, 0.2, 0.25, 0.3$).

Dataset
/RSGravToGG_kMpl-001_M-XXX_TuneCUEP8M1_13TeV-pythia8/
/RSGravToGG_kMpl-01_M-XXX_TuneCUEP8M1_13TeV-pythia8/
/RSGravToGG_kMpl-02_M-XXX_TuneCUEP8M1_13TeV-pythia8/
/GluGluSpin0ToGG_W-0p014_M-XXX_TuneCUEP8M1_13TeV-pythia8/
/GluGluSpin0ToGG_W-1p4_M-XXX_TuneCUEP8M1_13TeV-pythia8/
/GluGluSpin0ToGG_W-5p6_M-XXX_TuneCUEP8M1_13TeV-pythia8/

Table 2: Signal datasets. Masses between 500 GeV and 7000 GeV were generated. All samples belong to the RunIISpring16 campaign.

111

112 The main background processes to the search are the irreducible background from the direct
 113 production of two photons as well as the reducible components due to $\gamma + jets$ and multi-

jet final states, where the jet fragments are misidentified as photons. The Sherpa generator was used to generate the continuum diphoton background, while Madgraph and PYTHIA were used for the reducible components. These samples were used to check the goodness of the selection (that was optimized in 2015 on the same simulation backgrounds) and the background estimates from data. In addition, events samples corresponding to the Drell-Yan production of two electrons were used to study the identification criteria efficiency. The sample was produced using the aMC@NLO generator. The list of background samples used in the analysis is reported in Tab. 3.

Dataset	Cross section [pb]
/GGJets_M-60To200_Pt-50_13TeV-sherpa/	5.971
/GGJets_M-500To1000_Pt-50_13TeV-sherpa/	1.510e-01
/GGJets_M-1000To2000_Pt-50_13TeV-sherpa/	1.181e-02
/GGJets_M-2000To4000_Pt-50_13TeV-sherpa/	3.690e-04
/GGJets_M-4000To6000_Pt-50_13TeV-sherpa/	2.451e-06
/GGJets_M-6000To8000_Pt-50_13TeV-sherpa/	1.753e-08
/GGJets_M-8000To13000_Pt-50_13TeV-sherpa/	7.053e-11
/GJets_DR-0p4_HT-40To100_TuneCUETP8M1_13TeV-madgraphMLM-pythia8/	18420.0
/GJets_DR-0p4_HT-100To200_TuneCUETP8M1_13TeV-madgraphMLM-pythia8/	4881.0
/GJets_DR-0p4_HT-200To400_TuneCUETP8M1_13TeV-madgraphMLM-pythia8/	1092.0
/GJets_DR-0p4_HT-400To600_TuneCUETP8M1_13TeV-madgraphMLM-pythia8/	126.3
/GJets_DR-0p4_HT-600ToInf_TuneCUETP8M1_13TeV-madgraphMLM-pythia8/	44.75
/QCD_Pt-20to30_EMEEnriched_TuneCUETP8M1_13TeV_pythia8/	557600000
/QCD_Pt-30to50_EMEEnriched_TuneCUETP8M1_13TeV_pythia8/	6.876e+06
/QCD_Pt-50to80_EMEEnriched_TuneCUETP8M1_13TeV_pythia8/	2.180e+06
/QCD_Pt-80to120_EMEEnriched_TuneCUETP8M1_13TeV_pythia8/	4.140e+05
/QCD_Pt-120to170_EMEEnriched_TuneCUETP8M1_13TeV_pythia8/	7.517e+04
/QCD_Pt-170to300_EMEEnriched_TuneCUETP8M1_13TeV_pythia8/	1.899e+04
/QCD_Pt-300toInf_EMEEnriched_TuneCUETP8M1_13TeV_pythia8/	1.249e+03
/DYToEE_NNPDF30_13TeV-powheg-pythia8/	2008

Table 3: Background datasets with their cross-sections. All samples belong to the RunIISpring16 campaign.

The datasets include the simulation of pile-up interactions. An average of 20 interactions per bunch crossing is included in the simulation and the bunch spacing is 25 ns. The simulated pile-up distribution was reweighted to match the corresponding distribution in the analyzed data. For data, the pile-up reweighting was performed by using a ‘minimum bias cross section’ of $\sigma = 69$ mb. The average pileup in data is about 18, with an RMS of about 4. A comparison of the reweighted number of vertices distribution for a $Z \rightarrow ee$ sample and for the diphoton event selection is shown in Figure 1. It can be seen that in the latter case a good match between data and predictions is observed, while a worse agreement is seen in the former case. Since the main difference between these two sample is trigger used to select the data sample, we ascribe the missmodelling to an inefficiency of the electron trigger, which does not affect the analysis results.

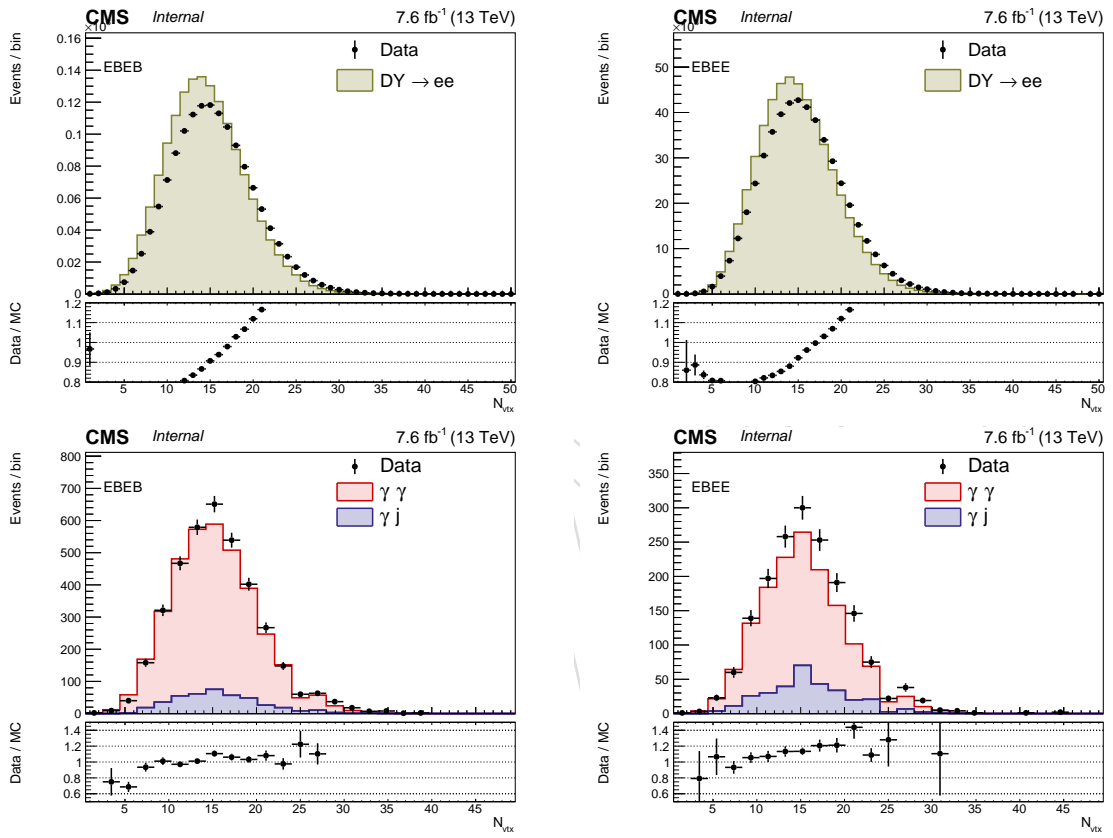


Figure 1: Number of vertices distribution for EBEB (left) and EBEE (right) after PU reweighting. The top row shows $Z \rightarrow e^+e^-$ events selected with the single electron trigger, while the bottom row shows diphoton events selected with the analysis trigger.

133 3 Event selection

134 The search strategy is very simple: the analysis selects photon pairs and looks for excesses over
 135 the SM continuum in the diphoton mass spectrum.

136 Events are required to satisfy the trigger selection described in section 3.1. For these events,
 137 pairs of photons are combined to form diphoton candidates which have to pass the preselec-
 138 tion detailed in section 3.2 and then the photon identification and isolation criteria which are
 139 described in section 3.3.

140 All the criteria were studied in 2015 and applied for the 2016 data as well after having verified
 141 the changes between the two datasets.

142 3.1 Trigger selection

143 A dedicated trigger path, requiring two photon candidates with a transverse momentum larger
 144 than 60 GeV, was developed for this analysis. The ratio of the hadronic and electromagnetic en-
 145 ergy deposit ('H/E ratio') is required to be below 0.15 and no other identification requirements
 146 are applied.

147 The efficiency of this trigger was studied in data using a di-electron control sample. The events
 148 used in this studies were required to be triggered by the SingleEle_35_WP Loose_Gsf path. Pairs
 149 of photon candidates compatibles with two clusters of pixel hits were then selected and re-
 150 quired to satisfy all the photon identification criteria used in the analysis (except the electron
 151 veto). The transverse momenta of the leading (sub-leading) photon candidate was required to
 152 be above 40(25) GeV. This sample is almost completely composed by events where a Z boson
 153 decays to a di-electron pair. The invariant mass of the selected pairs is shown in Figure 25.

154 To study the efficiency of the trigger selection, the leading photon candidate was required to
 155 match an HLT candidate associated with the SingleEle_35_WP Loose_Gsf path, as well as an
 156 e/γ level-1 trigger object with transverse energy above 26 GeV. In this way a sample of photon
 157 candidates unbiased from the trigger point of view can be selected. (**Note:** the results on the
 158 trigger efficiency are still based on 4.34 fb^{-1} of data and are being updated).

159 The HLT_DoublePhoton_60 path is seeded by the OR of three level-1 bits: SingleEG40, Single-
 160 Jet200, and DoubleEG_22_12. We studied the efficiency of the first bit by counting the frac-
 161 tion of subleading photon candidates that match an e/γ level-1 trigger object of transverse
 162 energy above 40 GeV. Figure 2 shows such a fraction as a function of the photon candidate
 163 p_T for photons in the barrel and endcaps regions. For photon candidates in the barrel with
 164 $75 < p_T < 300 \text{ GeV}$ the efficiency of the level-1 trigger is found to be above 97%. For transverse
 165 momenta below 400 GeV, the efficiency is estimated to be above 90% (at 68% CL). Assum-
 166 ing no correlated source of inefficiency between the two legs, we can therefore estimate a L1
 167 trigger efficiency higher than 99% for events with two photons in the barrel region and with
 168 $p_T < 400 \text{ GeV}$. A similar conclusion can be taken for events with at lease one photon in the
 169 endcaps region with $p_T < 300 \text{ GeV}$.

170 While more data are required to characterize the phase space with higher transverse momenta,
 171 the "H/E" requirement applied in the level-1 trigger (0.03 and 0.06 for barrel and endcaps re-
 172 spectively) is expected to reduce the efficiency of the SingleEG starting at $p_T \sim 500 \text{ GeV}$. In
 173 this case, the SingleJet200 seed is expected to recover most of the inefficiency. As a further
 174 precaution, the events accepted by the HLT_ECALHT800 path were also used for analysis.

175 The efficiency of the HLT selection is studied by counting the fraction of subleading photon
 176 candidates that match an HLT candidate associated with the HLT_DoublePhoton_60 path. The

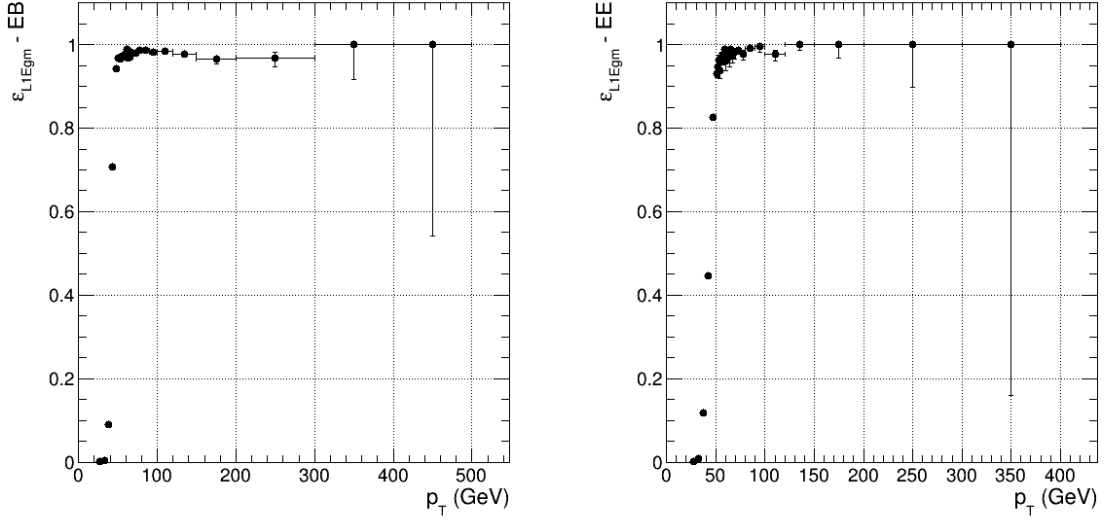


Figure 2: Efficiency for the subleading photon candidate to match an e/γ level-1 trigger object of transverse energy above 40 GeV. The left and right plots refer to photon candidates in the barrel and endcaps regions respectively.

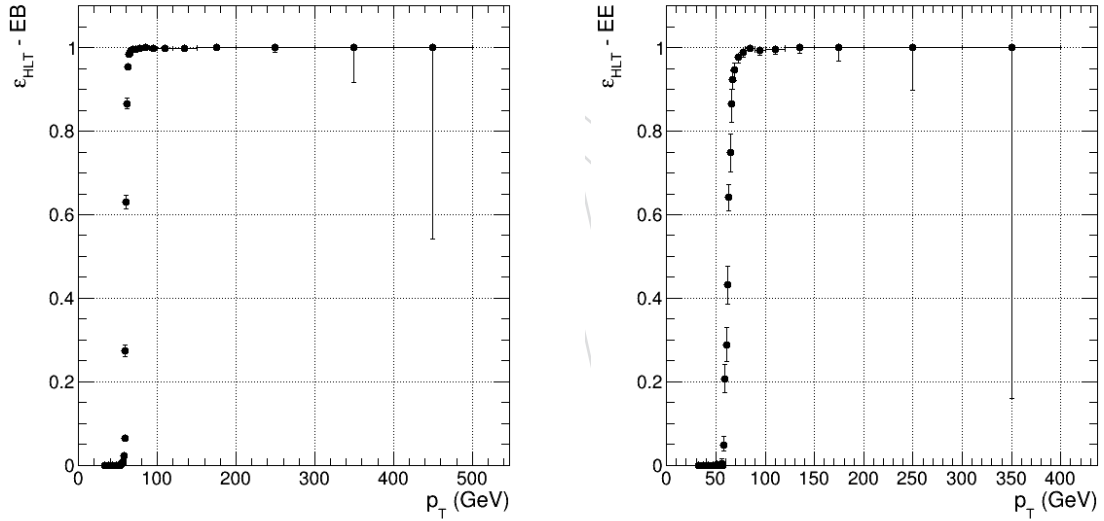


Figure 3: Efficiency for the HLT_DoublePhoton_60 bit to fire in di-electron events where SingleEle_27_WPLoose_Gsf has fired as a function of the subleading photon p_T . The left and right plots refer to photon candidates in the barrel and endcaps regions respectively.

resulting curves are shown in Figure 3, where it can be seen that the requirement is fully efficient for events where the sub-leading photon candidate p_T is above 65 GeV.

Assuming no correlation between the two legs, the HLT selection can be estimated to be fully efficient for all the events entering the final analysis selection, where the photon candidates are required to have a p_T of at least 75 GeV.

The trigger information is missing in Spring16 MC samples, therefore no explicit trigger requirement is applied to MC. Anyway since the efficiency measured in data is consistent with 1 no additional correction is applied to MC.

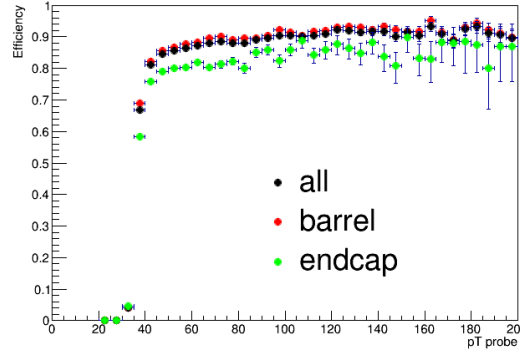


Figure 4: Efficiency for the SingleEle_35_WP Loose_Gsf bit to fire in di-electron events where HLT_Ele27_eta2p1_WP Loose_Gsf has fired as a function of the probe photon p_T .

185 3.1.1 Control paths

186 The trigger strategy described in the previous section refers to the selection of events for the
 187 analysis. Control single photon paths are used to model the fake photon background and single
 188 electron paths to determine efficiencies and energy scale. Since a perfect events normalization
 189 is not needed for these studies, we do not measure the trigger efficiency for those paths.

190 In the note we have several control plots based on a data sample enriched in $Z \rightarrow ee$ events.
 191 These events are requested to fire the SingleEle_35_WP Loose_Gsf path. We measure the effi-
 192 ciency of this HLT selection again with a tag-and-probe technique, in events which fire the
 193 HLT_Ele27_eta2p1_WP Loose_Gsf path. A tag electron must be present in these event, with
 194 $p_T > 40$ GeV. It must pass the ‘tight’ working point of the electron selection developed by the
 195 EGamma POG in 2015 and a proposed preselection to mimic the online working point, again as
 196 suggested by the POG. A match with an HLT candidate from HLT_Ele27_eta2p1_WP Loose_Gsf
 197 is requested for the tag. Since the SingleEle_35_WP Loose_Gsf path was prescaled towards the
 198 end of the considered data taking, to be sure that it was on we require the tag to also match
 199 an HLT candidate from it. The probe photon must have $p_T > 20$ GeV and pass the full photon
 200 selection detailed in Section 3.3. The invariant mass of the tag and probe system is required to
 201 be within 70 GeV and 110 GeV. The efficiency of the HLT selection is studied by counting the
 202 fraction of probes that match an HLT candidate associated with the SingleEle_35_WP Loose_Gsf
 203 path. The resulting curves are shown in Figure 4. These efficiencies are used to correct the
 204 simulation predictions.

205 3.2 Events preselection

206 The diphoton candidates are required to satisfy the following kinematic criteria:

- 207 • The p_T of both candidates has to be above 75 GeV.
- 208 • The absolute value of the pseudo-rapidity of both candidates, computed with re-
 209 spect to centre of the CMS detector and denoted η_{SC} in the following, is required to
 210 be below 2.5 and not between 1.4442 and 1.566.
- 211 • At least one of the photon candidates has to have η_{SC} below 1.4442 (i.e. events with
 212 both photon candidates in the endcaps regions are rejected).
- 213 • The invariant mass of the pair is required to be above 230 GeV. For events where one
 214 of the photon candidates was in the endcap region, the minimal invariant mass was
 215 asked to be 320 GeV.

216 Both photon candidates in each pair are then required to satisfy the identification criteria de-
 217 scribed in Sec. 3.3. If more than one diphoton candidate satisfies the set of selection criteria
 218 described, only the pair with the largest scalar sum of photon momenta is retained.

219 A primary vertex is assigned to each diphoton candidate and the photon candidates kinematic
 220 properties are computed under this assumption. The standard algorithm used in CMS ranks
 221 the primary vertices according to the sum of the squares of the tracks transverse momentum. In
 222 the case of events with neutral particles this algorithm may lead to suboptimal performances,
 223 while the vertex-finding performances can be improved through the analysis of the correlation
 224 between the tracks recoil and the diphoton system. Such algorithms have been successfully
 225 used in the search for the diphoton decay of the Higgs boson [16]. In this analysis we use the
 226 same algorithm used for the Higgs $\rightarrow \gamma\gamma$ search.

227 The events are split in two categories: one (EBEB) in which both photons are in the barrel and
 228 the other one (EBEE) where one photon is in the barrel and the other in the endcaps. Further
 229 categorizations based on the shower shape of the photons ('R9' variable) were also tested but
 230 the improvement was found to be negligible (1-3% on expected limit and significance)

231 3.3 Photon identification and isolation requirements

232 A dedicated set of photon identification criteria, targeting high p_T objects, has been developed
 233 for the analysis. The reason for developing a custom set is that the criteria developed by the
 234 E/gamma POG are typically tuned for objects of much lower transverse momenta than those
 235 used here. Therefore optimal analysis performances require dedicated tuning.

236 The variables used in the analysis are defined as follows:

- Iso_{Ch} : the scalar sum of the transverse momenta of the charged PF hadron candidates assigned to the chosen primary vertex for which

$$\Delta R = \sqrt{(\eta_\gamma - \eta_{cand})^2 + (\phi_\gamma - \phi_{cand})^2} < 0.3$$

237 .
 238 • Iso_γ : the scalar sum of the transverse energies of the PF photon candidates for which
 239 $\Delta R < 0.3$.

240 • H/E : the ratio of the energy deposited in the HCAL tower behind the photon can-
 241 didate and the energy of the candidate itself.

- $\sigma_{i\eta i\eta}$: the spatial second order moment of the photon candidate in the η direction, computed as

$$\sigma_{i\eta i\eta} = \sqrt{\frac{\sum_{i \in 5 \times 5} (\eta_i - \bar{\eta})^2 w_i}{\sum_{i \in 5 \times 5} w_i}}, \quad w_i = \max(0, 4.7 + \log(E_i/E_{5 \times 5}))$$

242 .
 243 • R_9 : the ratio between the energy of the 3x3 crystals around the most energetic crystal
 244 and the energy of the whole supercluster.

245 In all cases, the particle-flow candidates sharing part of the energy with the selected photon
 246 candidate are excluded from all isolation sums. This definition reflects the choices made by the
 247 E/gamma POG.

The dependence of the chosen identification variables as a function of pile-up and transverse momentum was studied. Only in the case of Iso_γ the observed effect was found to be sizable and specific corrections were applied. The latter were derived to correct in particular the

region	A (2015)	A (2016)
$\eta_{SC} < 0.9$	0.17	0.16
$0.9 < \eta_{SC} < 1.4442$	0.14	0.14
$1.566 < \eta_{SC} < 2.0$	0.11	0.11
$2.0 < \eta_{SC} < 2.2$	0.14	0.15
$2.2 < \eta_{SC} < 2.5$	0.22	0.18

Table 4: Effective areas computed on 2015 and 2016 Montecarlo samples. Given the good agreement, the 2015 numbers were used for corrections factors for the Iso_γ variable.

region	α (GeV)	A	κ (1/GeV)
$\eta_{SC} < 0.9$	2.5	0.17	4.5×10^{-3}
$0.9 < \eta_{SC} < 1.4442$	2.5	0.14	4.5×10^{-3}
$1.566 < \eta_{SC} < 2.0$	2.5	0.11	3×10^{-3}
$2.0 < \eta_{SC} < 2.2$	2.5	0.14	3×10^{-3}
$2.2 < \eta_{SC} < 2.5$	2.5	0.22	3×10^{-3}

Table 5: Corrections factors for the Iso_γ variable.

dependence of the 95% quantile of the signal Iso_γ . The general form of these correction is:

$$\bar{\text{Iso}}_\gamma = \alpha + \text{Iso}_\gamma - \rho \cdot A - \kappa \cdot p_T$$

Since the isolation variable is corrected to flatten the dependence of 95% quantile of the signal distribution, the pile-up and p_T corrections tend to over-subtract energy in the bulk of the distribution. The α term is added to bring back the median of the corrected distribution to a value of roughly 0.

Values of α , A and κ were derived separately for different rapidity regions. The coefficients were found to be consistent with the results of Refs. [17, 18] within about 5-10%. For a comparison, the values computed on the new Montecarlo samples for the effective areas are compared with the previous ones in Table 4. The agreement is fine. In order to have a uniform set of identification criteria for the 2015 and the 2016 dataset, the numerical values from Refs. [17, 18] were used. They are listed in Table 5.

As the reader may have noticed, the α term in the definition of the corrected photon isolation variable could be dropped and its value subtracted from the corresponding thresholds. The reason to introduce it is to maintain the intuitive meaning of the Iso_γ variable.

In fact, since the A and κ terms were chosen in order to correct the dependence of the 95% signal quantile, most of the signal photon receive an average correction which is larger than the uncorrected isolation (in other words, the slope of the 95% quantile is more steep than the one of the median).

The α term was then introduced such that the median of the $\bar{\text{Iso}}_\gamma$ would be roughly 0, as intuitively expected for isolated photon candidates.

photon category	Iso_{Ch} cut (GeV)	$\bar{\text{Iso}}_\gamma$ cut (GeV)	H/E cut	$\sigma_{i\eta i\eta}$ cut
$\eta_{SC} < 1.4442$ non-sat.	5	2.75	5×10^{-2}	0.0105
$\eta_{SC} < 1.4442$ sat.	5	2.75	5×10^{-2}	0.0112
$\eta_{SC} > 1.566$ non-sat.	5	2.0	5×10^{-2}	0.028
$\eta_{SC} > 1.566$ sat.	5	2.0	5×10^{-2}	0.030
conversion-safe electron veto applied for all categories				

Table 6: Photon identification criteria used in the analysis.

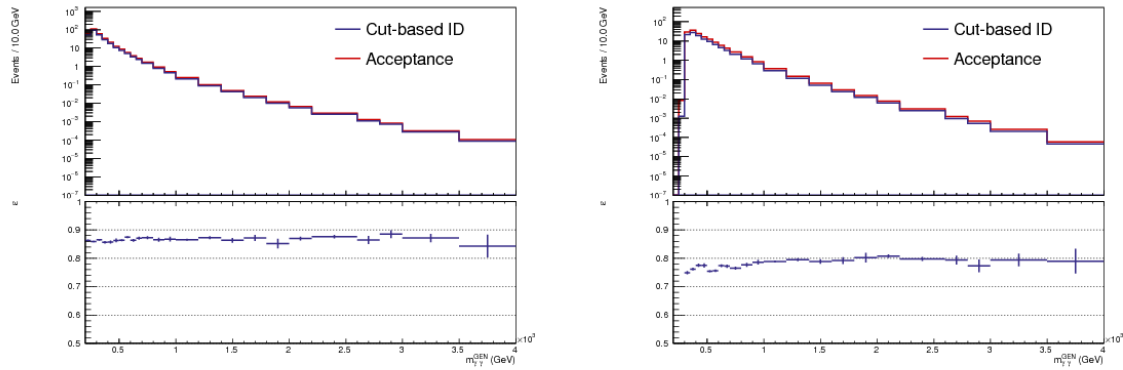


Figure 5: Diphoton identification efficiency as a function of the diphoton invariant mass at gen-level, evaluated on the $\gamma\gamma$ background. The efficiency is computed with respect to the diphoton candidates passing the preselection detailed in 3.2 and with two photons isolated at generator level. Events in the EB-EB (EB-EE) category are shown on the left (right).

- 267 The set of identification criteria used in the analysis was taken from Refs. [17, 18] and is shown
 268 in table 6. In addition to the criteria in Tab. 6, the photon candidates are required to satisfy the
 269 so-called “conversion-safe electron veto” criterion. The conversion-safe electron veto rejects
 270 electrons associated with tracks that have no missing hits.
- 271 The diphoton identification efficiency as a function of the diphoton invariant mass at gen-level
 272 is reported in figure 5. The overall diphoton identification efficiency is over 85% for diphoton
 273 candidates in the barrel-barrel category and it is about 80% in the barrel-endcap one.

process	$m_{\gamma\gamma} > 230\text{GeV}$	$m_{\gamma\gamma} > 320\text{GeV}$	$m_{\gamma\gamma} > 500\text{GeV}$	$m_{\gamma\gamma} > 500\text{GeV}$
	EBEB N_{ev}	EBEE N_{ev}	EBEB N_{ev}	EBEE N_{ev}
data	3782 ± 61	1740 ± 42	275 ± 17	499 ± 22

Table 7: Observed number of events in the two analysis categories.

274 4 Selected sample

275 The total number of selected events is reported in table 7.

The mass spectrum of the observed events is reported in Fig. 6 and 7 for the EBEB and EBEE categories, respectively. In both cases, the mass spectra are parametrized using the functional form

$$g(m_{\gamma\gamma}) = m_{\gamma\gamma}^{a+b \log(m_{\gamma\gamma})}$$

276 .

277 In Fig. 8 the diphoton invariant mass spectrum in data is compared with the simulation predictions for the two categories used in the analysis. The Montecarlo predictions are rescaled by a 278 factor 1.4 to account for higher order effects.

280 4.1 Comparison with 2015 results

281 The sample selected in 2016 in data and MC has been compared with the one from the 2015 282 analysis. In tables 8 and 9 we compare the number of events in the full analysis region and 283 in the search region for the two datasets, in the two analysis categories. A scale factor of 1.4 is 284 applied to the Montecarlo predictions for both years.

	$m_{\gamma\gamma} > 230\text{GeV}$	$m_{\gamma\gamma} > 500\text{GeV}$		
	2015	2016	2015	2016
$\gamma\gamma$	1050	3498	93	268
γjet	334	436	16	21
total	1384	3934	109	289
data	1236	3782	97	275

Table 8: Number of events selected in data and predicted from Montecarlo in the EBEB category. A scale factor of 1.4 is applied to the Montecarlo predictions. Numbers for 2016 refer to a luminosity of 7.6 fb^{-1} , numbers for 2015 to 2.7 fb^{-1} .

	$m_{\gamma\gamma} > 320\text{GeV}$	$m_{\gamma\gamma} > 500\text{GeV}$		
	2015	2016	2015	2016
$\gamma\gamma$	410	1279	128	354
γjet	222	335	61	86
total	632	1616	189	440
data	621	1740	184	499

Table 9: Number of events selected in data and predicted from Montecarlo in the EBEE category. A scale factor of 1.4 is applied to the Montecarlo predictions. Numbers for 2016 refer to a luminosity of 7.6 fb^{-1} , numbers for 2015 to 2.7 fb^{-1} .

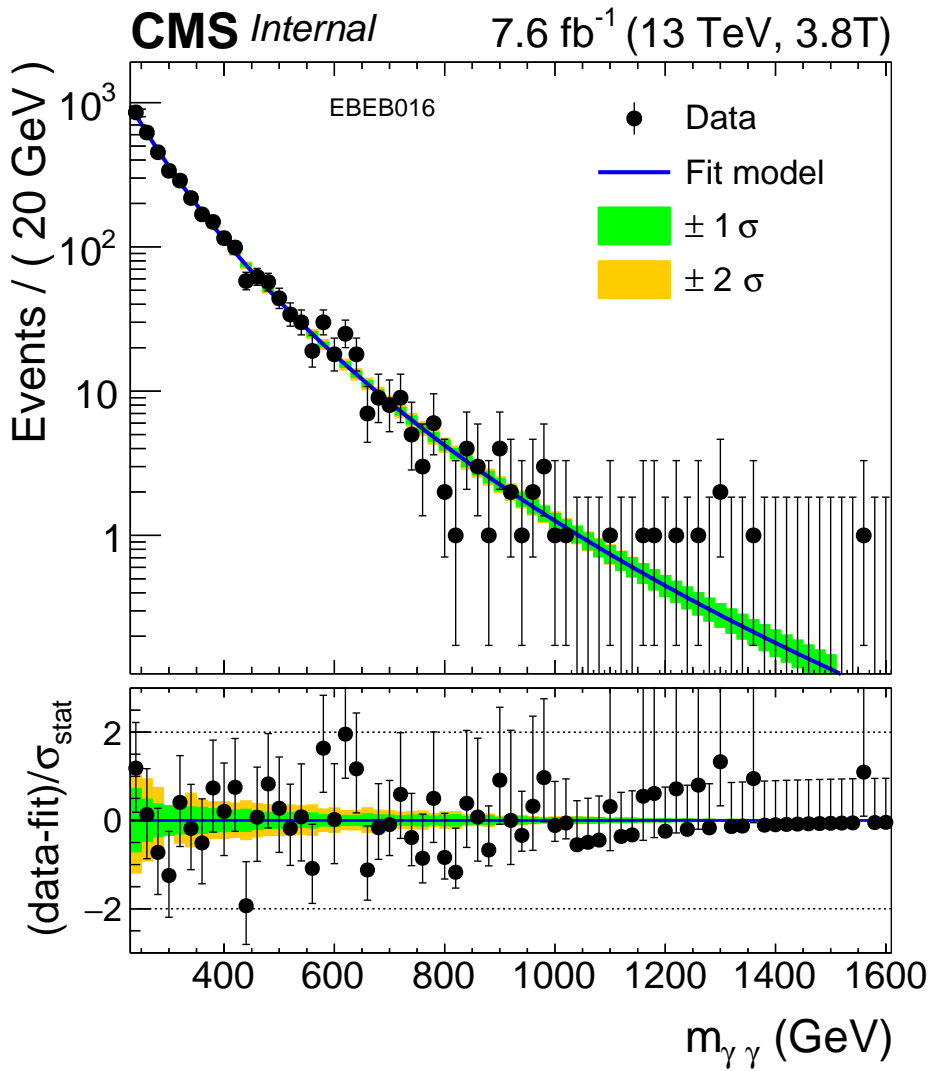


Figure 6: Observed mass spectrum in the EBEB category. The result of the parametric fit is superimposed to the points, together with bands representing the statistical uncertainties on the knowledge of the background shape.

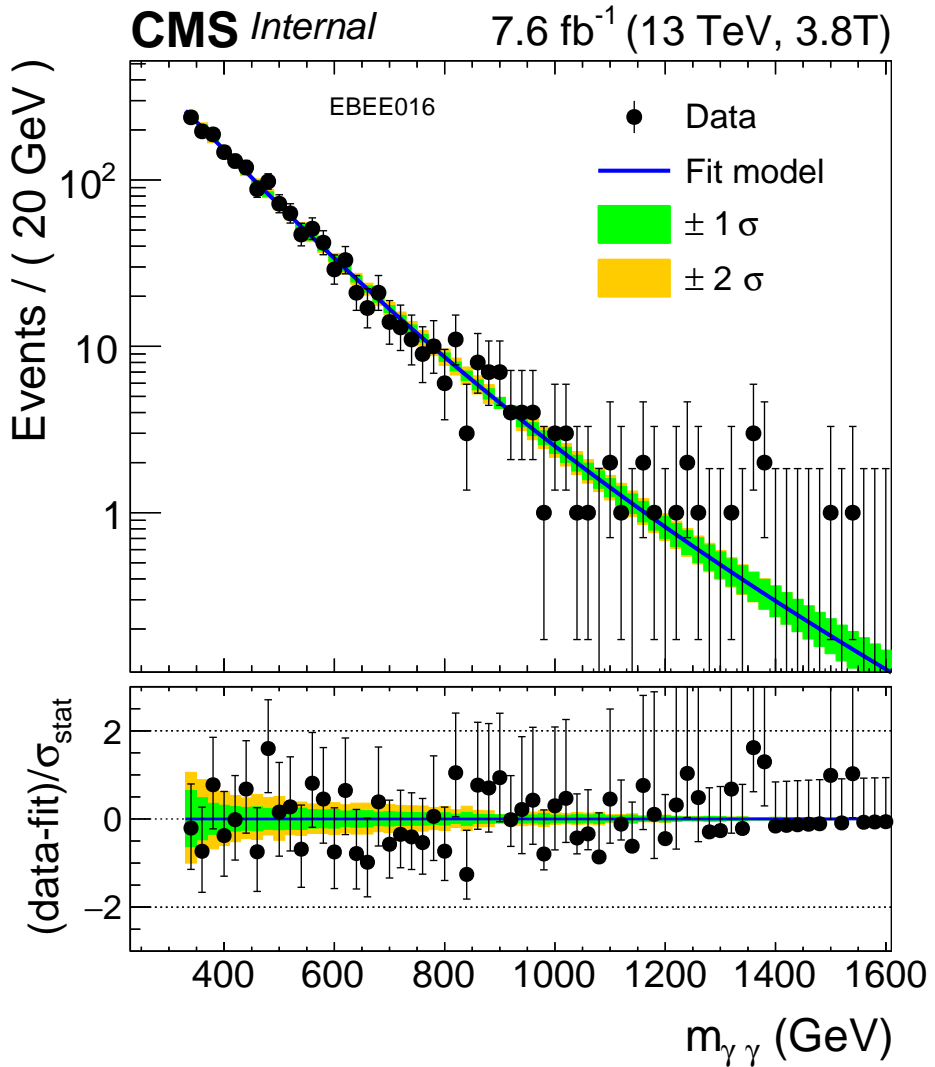


Figure 7: Observed mass spectrum in the EBEE category. The result of the parametric fit is superimposed to the points, together with bands representing the statistical uncertainties on the knowledge of the background shape.

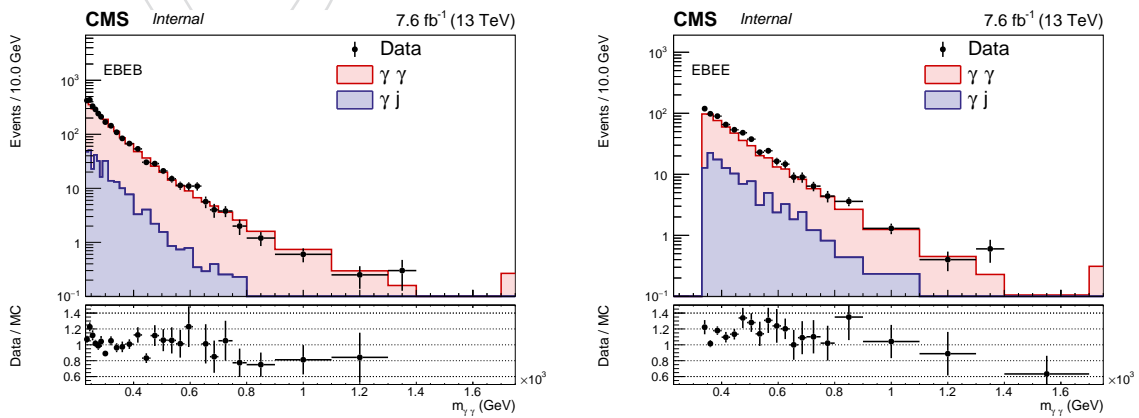


Figure 8: Data-MC comparison of the diphoton invariant mass distribution for EBEB (left) and EBEE (right).

285 5 Energy scale and resolution corrections

286 Data-driven scale factors for the photon energy scale and resolution are extracted from $Z \rightarrow e^+ e^-$
 287 decays. For the measurement technique we refer to [18] and [17].

288 The only change with respect to what is documented in [18] is the fact we have derived new
 289 corrections on the 80X Prompt-reco data and 80X MC samples. In the first step of the calibration
 290 procedure run dependent energy corrections are applied to correct for possible time dependent
 291 energy scale variations during the data-taking; while the overall behavior of the scale in EB is
 292 rather stable, we observe some significant variations in EE as can be seen in Figure 9. The effect
 293 is particularly evident for the high- η region of EE, where a variation of about 1% is observed.

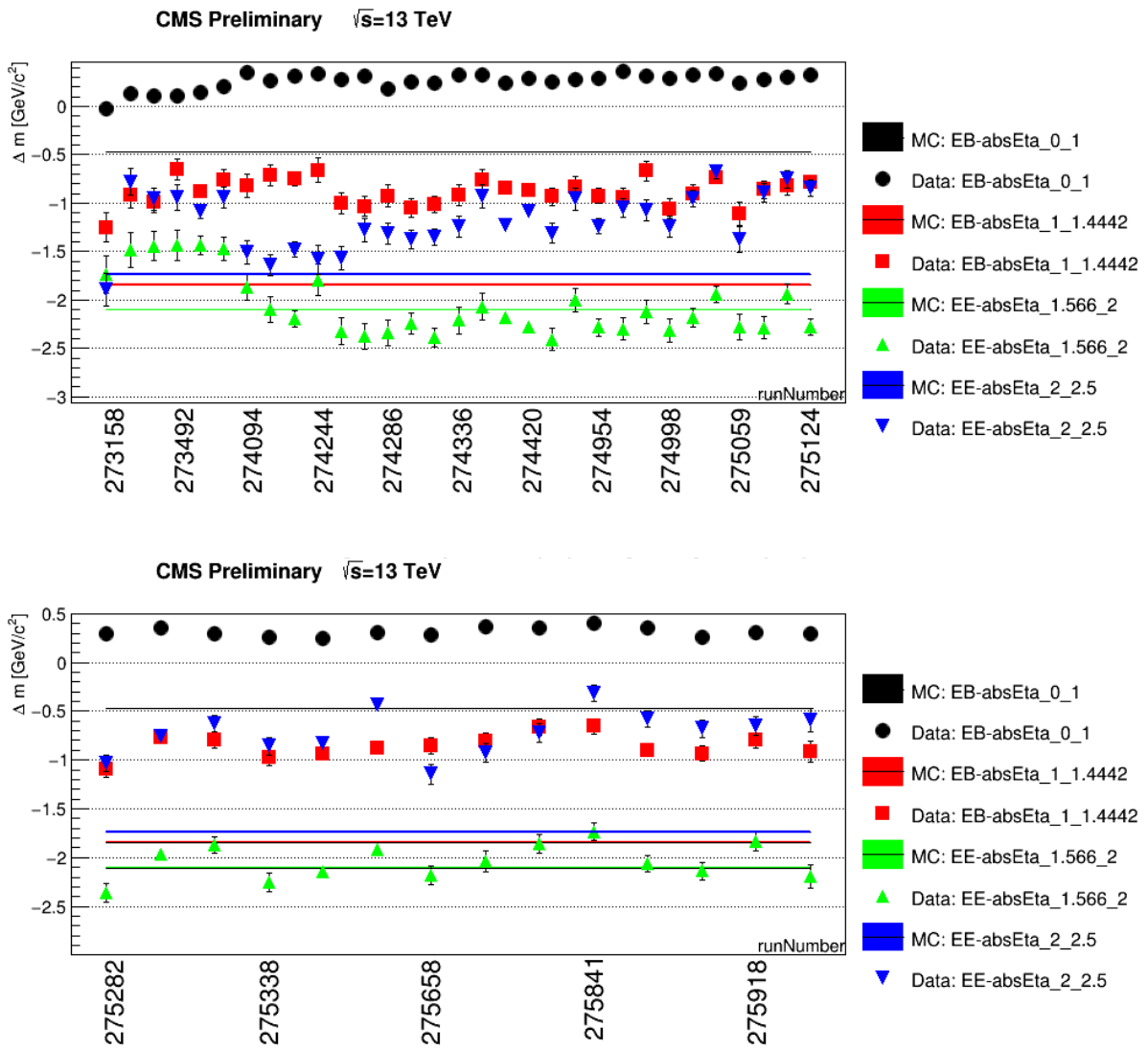


Figure 9: $Z \rightarrow e^+ e^-$ lineshape peak values in several run ranges for 4 η categories: 2 categories in EB, 2 categories in EE. MC value is displayed as a continuous line. The top and bottom plots refer to the first 4.3 fb^{-1} and the second 3.3 fb^{-1} data respectively.

294 Both data and MC invariant mass distributions are fitted with a Breit-Wigner function convo-
 295 luted with a Crystal Ball. The mean parameter fitted in data is then corrected in order to match
 296 the mean parameter fitted in MC, bin per bin in run ranges. Data/MC run dependent energy

297 scale factors are hence applied to the data. After applying the time-dependent corrections to
 298 the data scale, we obtain a much more stable behavior over time, as can be seen in fig. 10.

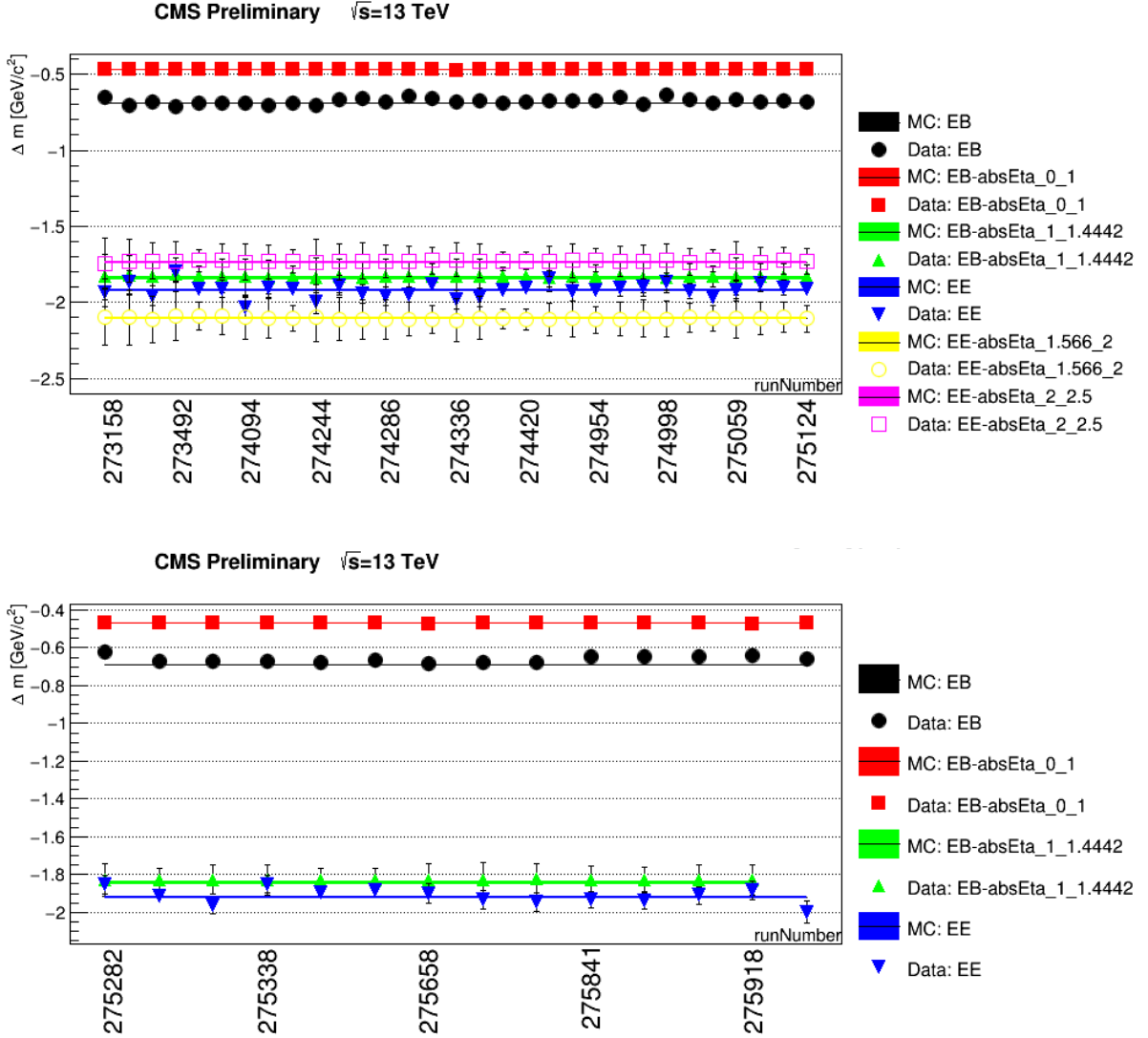


Figure 10: $Z \rightarrow e^+e^-$ lineshape peak values in several run ranges after applying the time-dependent scale corrections to data. MC value is displayed as a continuous line. The top and bottom plots refer to the first 4.3 fb^{-1} and the second 3.3 fb^{-1} data respectively.

299 In the second step of the procedure, we derive a set of smearing corrections in 8 categories
 300 ($4\eta \times 2R_9$) minimizing the likelihood between the smeared MC and the data. We also correct
 301 for the eventual residual energy shifts needed to align the data to the MC. Hence, the set of
 302 scale corrections is run-, η - and R_9 -dependent, while the smearing corrections are only η - and
 303 R_9 -dependent. The latter can be found in table 10, where the smearing corrections are called
 304 ΔC and their statistical errors are labeled as $\Delta_{\text{stat}} C$. The data energy scale corrections are not
 305 reported in the table simply due to the large amount of run-, η - and R_9 -bins which have been
 306 defined.

307 The results of the energy scale and resolution adjustment are shown in Fig. 11 for 2 categories:
 308 2 electrons in EB with $|\eta| < 1$ $R_9 > 0.94$, and 2 electrons in EE with $|\eta| < 2$ $R_9 < 0.94$. Figure 25

Category	$\Delta C[\%]$	$\Delta_{stat} C[\%]$
$ \eta < 1 R_9 < 0.94$	0.91	0.02
$ \eta < 1 R_9 > 0.94$	0.75	0.02
$ \eta > 1 R_9 < 0.94$	1.52	0.03
$ \eta > 1 R_9 > 0.94$	1.08	0.18
$ \eta < 2 R_9 < 0.94$	2.01	0.04
$ \eta < 2 R_9 > 0.94$	1.78	0.08
$ \eta > 2 R_9 < 0.94$	2.31	0.05
$ \eta > 2 R_9 > 0.94$	2.11	0.04

Table 10: MC energy smearing factors for 80X Prompt-reco obtained using $Z \rightarrow e^+e^-$ events in 8 categories: ($4\eta \times 2R_9$).

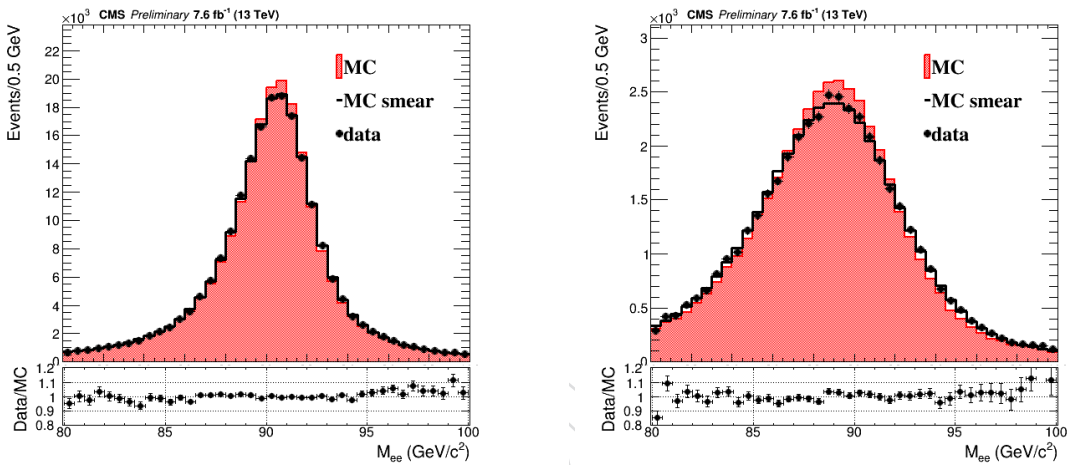


Figure 11: Data to MC agreement before and after the energy scale and smearing adjustments for the $Z \rightarrow e^+e^-$ selection for 2 example event categories: 2 electrons in EB with $|\eta| < 1 R_9 > 0.94$ (left), and 2 electrons in EE with $|\eta| < 2 R_9 < 0.94$ (right).

309 illustrates the application of these corrections for the event categories used in the analysis while
310 the same categories splitted in R_9 regions are shown in fig. 12.

311 Keeping the same approach as described in [18], we further check that the derived energy
312 corrections are still meaningful when computed as a function of the transverse energy of the
313 electrons. In particular, we apply the derived set of scale corrections and we inspect if there is
314 a need for extra corrections for different E_T bins, with special concern for the highest E_T bin,
315 defined as $E_T > 150$ GeV. The data-MC comparison for EB (EE) are shown in fig. 13 (14), as
316 well as the likelihood profiles for the highest bin of $E_T > 150$ GeV. From the likelihood it can
317 be seen that the extra scale corrections do not exceed the systematic uncertainty of 1% assigned
318 to the energy scale, being at the level of 0.3 (0.8)% for EB (EE).

319 5.1 Scale uncertainty related to the energy extrapolation

320 Still to be updated

321 The linearity of the energy response is studied using boosted Z-boson events and checking the
322 stability of the dielectron invariant mass as a function of the scalar sum of the transverse ener-
323 gies of the two electrons, i.e., $H_T = E_T^1 + E_T^2$. In this analysis, the dielectron invariant mass in
324 bins of H_T from MC simulation – tuned to match the resolution observed in data – are fitted to
325 the corresponding distributions in data. A scale factor is extracted from each fit, whose differ-

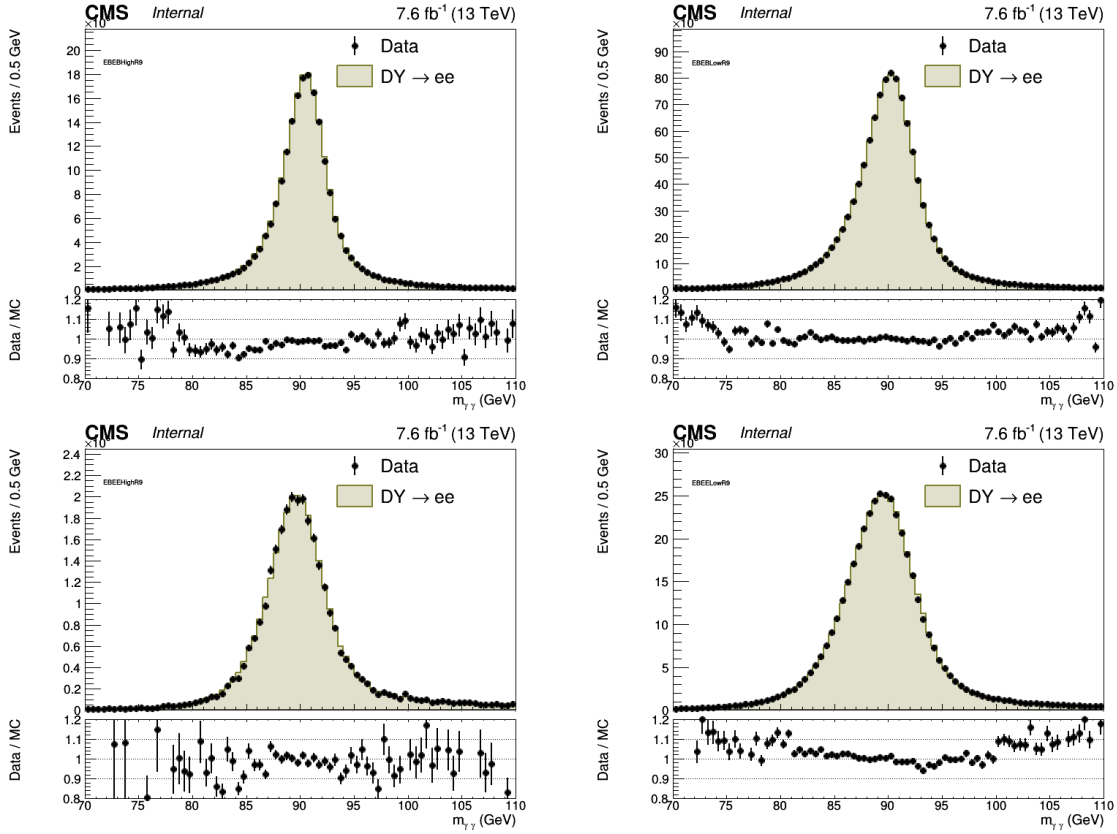


Figure 12: Comparison between the predicted and observed invariant mass distribution of electron pairs obtained after the application of energy scale and resolution corrections. Distributions are shown for events where both electrons are reconstructed in the barrel, with at least one having $R_9 > 0.94$ (top left) and at least one having $R_9 < 0.94$ (top right), as well as where one electron is reconstructed in barrel and the other in the endcap with at least one having $R_9 > 0.94$ (bottom left) and at least one having $R_9 < 0.94$ (bottom right). The simulation predictions are scaled to match the number of events observed in data.

326 ence from unity measures the residual non-linearity of the energy response in data relative to
 327 the MC samples. Alternatively, a recursive mean method has been used to estimate the dielec-
 328 tron invariant mass peak positions. The two methods give consistent results.
 329

330 The dielectron analysis is restricted to events where both the electrons belonged to the same
 331 photon identification category. Results are shown in Fig. 15. The four panels indicate results
 332 for the four different categories of photon identification. The statistical uncertainty on the scale
 333 factor at each H_T point (black error bars) is extracted from the fit of the reference MC distribu-
 334 tions to data. The distribution of the χ^2 values of all the fits matches the expectation for a χ^2
 335 distribution and provides confidence that the statistical uncertainties are correctly estimated.
 336 The differential non-linearity is estimated from a linear fit through the points (blue line). To
 337 account for possible deviation from a linear response, the uncertainties on the fit parameters
 338 of a linear response model is inflated by adding a common systematic uncertainty to all the
 339 points so that the χ^2/ndf of the fits is exactly equal to unity. The total uncertainty on the points
 340 is indicated by the red error bars in the plots, while the 68% C.L. region on the parameters is
 341 indicated by the light blue area.
 342

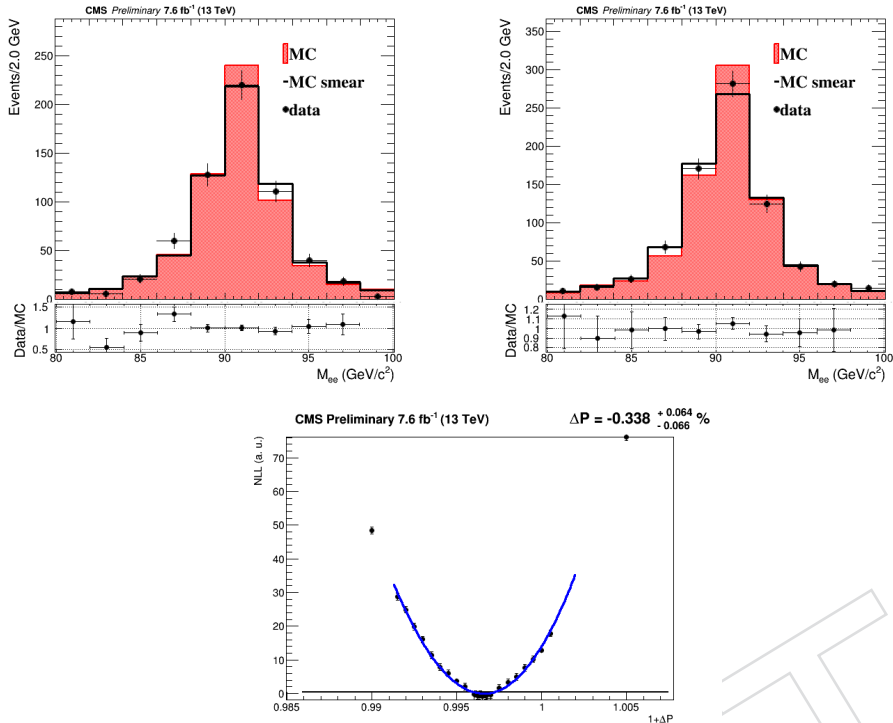


Figure 13: Data to MC agreement before and after the energy scale and smearing adjustments for the $Z \rightarrow e^+e^-$ selection for 2 example event categories with both electrons in EB: both electrons with $100 \text{ GeV} < E_T < 150 \text{ GeV}$ (top left), one electron with $100 \text{ GeV} < E_T < 150 \text{ GeV}$ and the other one with $E_T > 150 \text{ GeV}$ (top right). The likelihood profile for the category with $E_T > 150 \text{ GeV}$ is also shown (bottom).

343 The uncertainty on the measurement of the mass of a 750 GeV resonance is extracted by ap-
 344 plying the observed differential non-linearity to the MC samples. To this end, the diphoton
 345 invariant mass of each event is scaled by $\sqrt{f_{ID}(E_T^1)f_{ID}(E_T^2)}$, where E_T^1 and E_T^2 are the transverse
 346 energies of the photons. The functions $f_{ID}(E_T)$ are taken, for each photon identification cate-
 347 gory, from the linear fits through the points of Fig. 15. The procedure is repeated by floating
 348 the parameters of the $f_{ID}(E_T)$ functions within the uncertainties discussed above (and repre-
 349 sented by the light blue bands in Fig. 15). Results are reported in Fig. 16 where the diphoton
 350 invariant mass spectrum before and after applying the observed non linearity is shown. The
 351 uncertainty on the mass for each category estimated by adding in quadrature the shift of the
 352 central value (due to residual non linearities) and the RMS spread due to the uncertainty on
 353 the residual non-linearity. The total uncertainty on the diphoton invariant mass scale for a 750
 354 GeV narrow resonance is about 0.5% for events with both photons in EB and 0.5% for events
 355 with one photon in EB and one photon in EE.

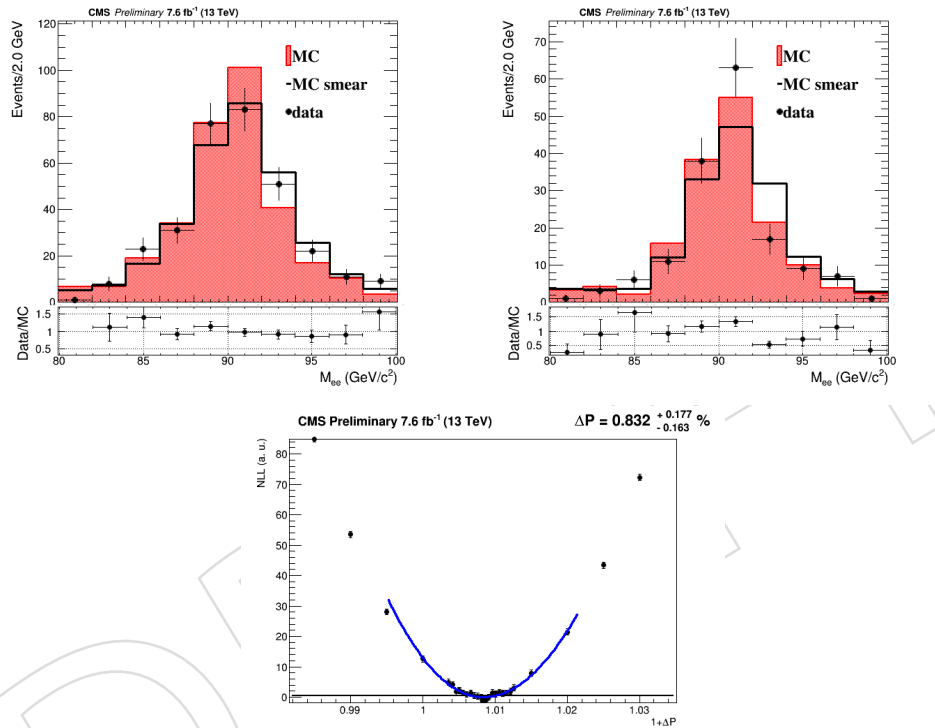


Figure 14: Data to MC agreement before and after the energy scale and smearing adjustments for the $Z \rightarrow e^+e^-$ selection for 2 example event categories with both electrons in EE: both electrons with $100 \text{ GeV} < E_T < 150 \text{ GeV}$ (top left), one electron with $100 \text{ GeV} < E_T < 150 \text{ GeV}$ and the other one with $E_T > 150 \text{ GeV}$ (top right). The likelihood profile for the category with $E_T > 150 \text{ GeV}$ is also shown (bottom).

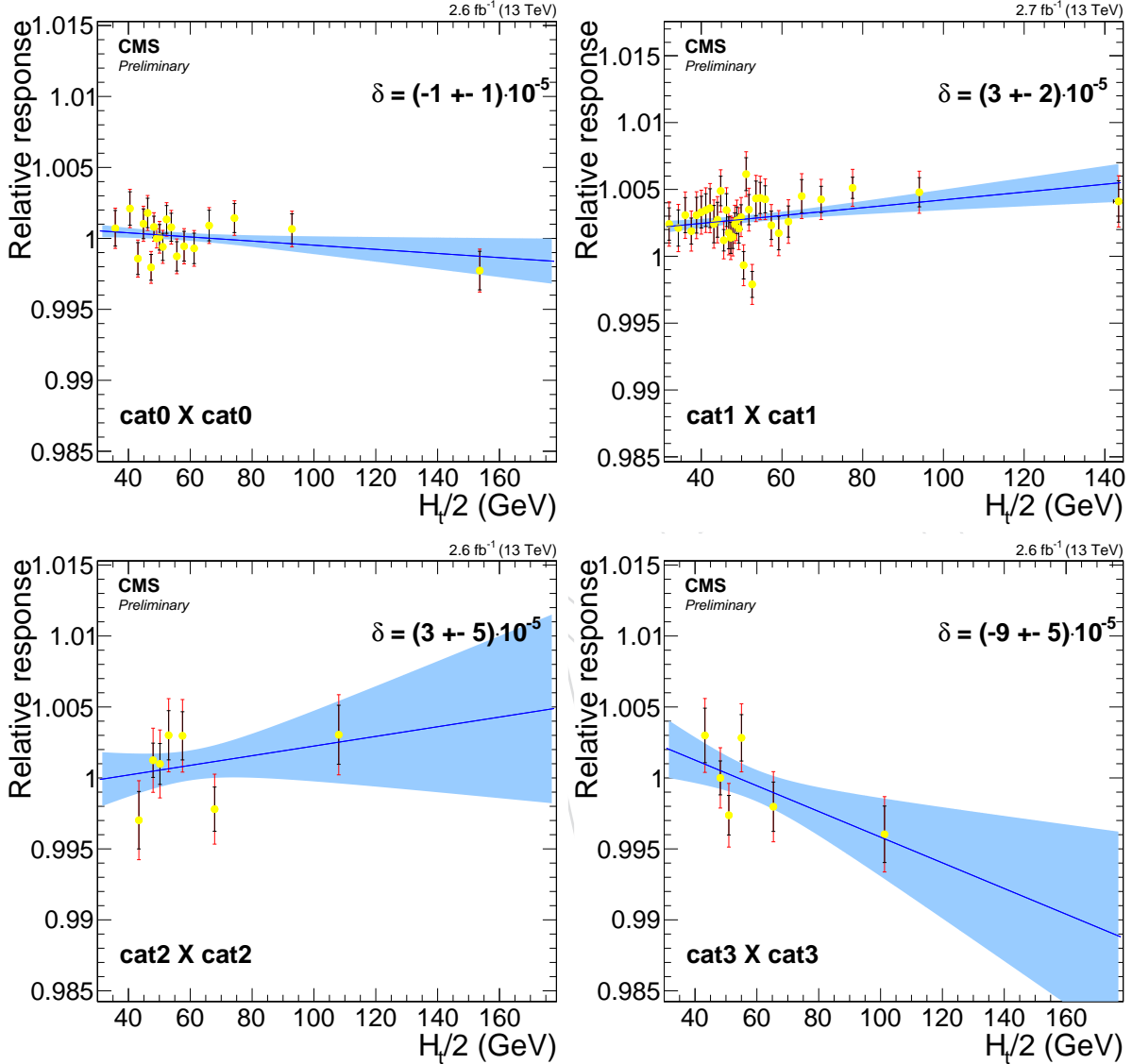


Figure 15: Differential non-linearity in the four photon identification categories (top-left: EB $R_9 > 0.94$, top right: EB $R_9 > 0.94$, bottom left: EE $R_9 > 0.94$, bottom right: EE $R_9 > 0.94$) as derived from the dielectron invariant mass. Each graph shows the ratio of the estimated position of the the m_{ee} invariant mass peaks in data to the corresponding position estimated in MC simulation. On the abscissa, the $H_T/2$ is shown. These results are obtained using 2.6 fb^{-1} of data collected in 2016.

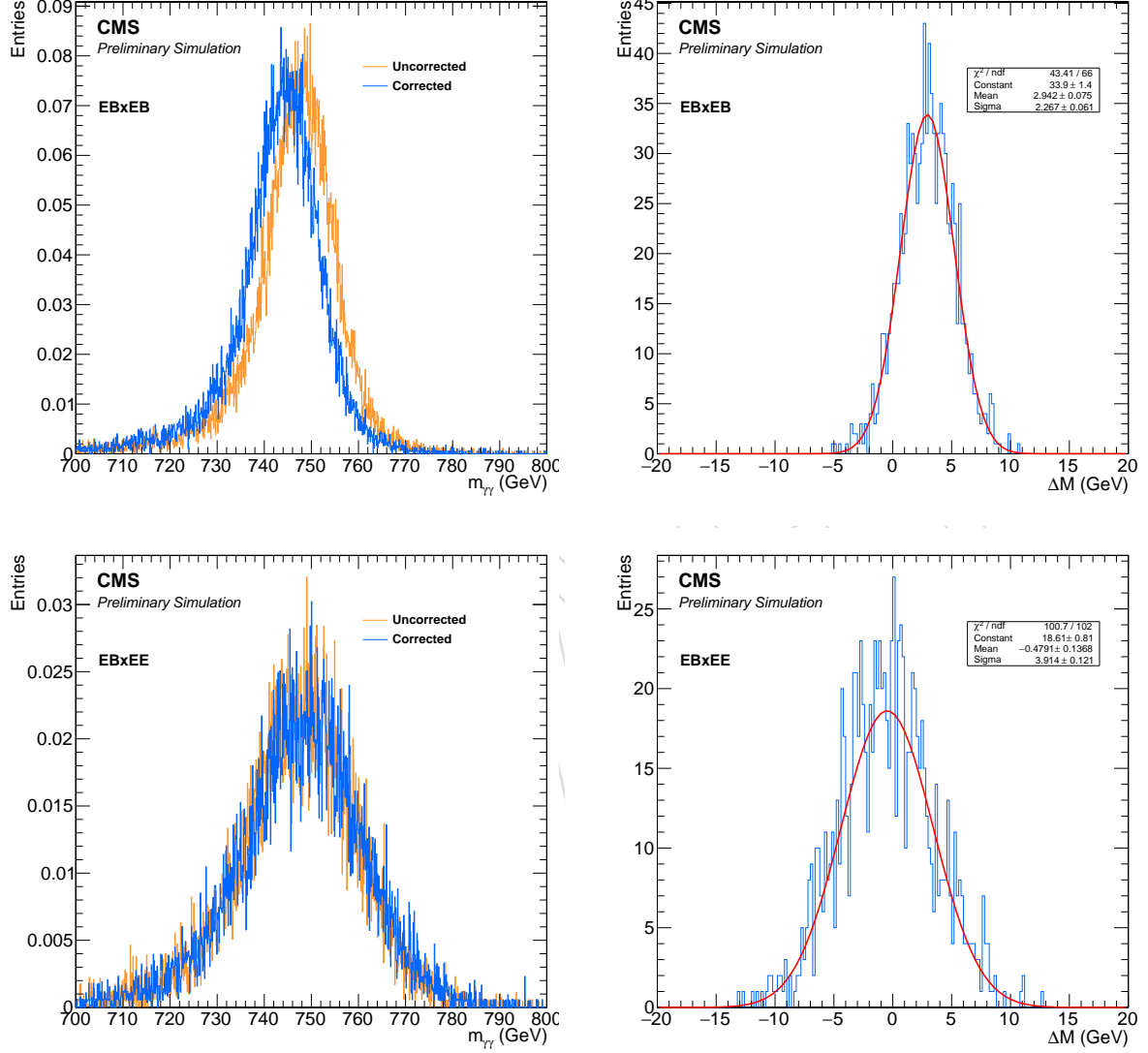


Figure 16: Left: diphoton invariant mass distribution for the two analysis categories before and after applying the measured residual non-linearity. Right: invariant mass shift for 1000 pseudo-experiments generated by floating the parameters of the $f_{ID}(E_T)$ functions within their uncertainties.

356 6 Selection efficiency control from data

357 The standard Tag and Probe technique using $Z \rightarrow e^+e^-$ events is used to determine the selection
 358 efficiency with the exception of the electron veto.

359 Data events are selected in the SingleElectron dataset which fire the *HLT_Ele27_eta2p1_WPLoose_Gsf*
 360 path. In Montecarlo no trigger information is required, since it is missing in the simulated sam-
 361 ples. A tag electron must be present in the event, with $p_T > 30\text{ GeV}$ and which passes the ‘tight’
 362 working point of the electron selection developed by the EGamma POG in 2015. Since it was
 363 recently discovered that the online ‘loose’ working point is actually tighter than the offline
 364 ‘medium’ and ‘tight’ ones, also the proposed preselection to mimic the online working point
 365 suggested by the POG is applied, both in data and in Montecarlo. To mimic the $|\eta| < 2.1$ cut
 366 applied in the trigger the tag is requested to be in the same pseudorapidity region offline, both
 367 in data and in simulation. A match with the HLT candidate is requested in data, and a match
 368 with the Montecarlo truth in the simulation. The probe photon must have $p_T > 20\text{ GeV}$ and
 369 pass the inverted electron veto. The invariant mass of the tag and probe system is required to
 370 be within 70 GeV and 110 GeV .

371 The p_T and η spectra of the probe photons entering the efficiency measurement are shown in
 372 Figure 17 for the probes in data and in Montecarlo. In Figures 18, 19 and 20 we compare the dis-
 373 tributions of the variables used in the photon selection in data and simulation. The Montecarlo
 374 yields are rescaled to match those in data. The agreement is fine in most of the variables. There
 375 may be some fakes contamination, which is visible in the H/E or photon-isolation distribu-
 376 tions, but this is not affecting the efficiency results since a fit to the mass spectrum is performed
 377 to disentangle signal and background. The variable which shows the largest disagreement be-
 378 tween data and MC is the photon component of the isolation after the corrections for p_T and
 379 pileup.

380 Since the selection efficiency may depend on the kinematics, the computations are done sepa-
 381 rately for photons in the barrel and in the endcaps and in several bins in p_T , which have been
 382 chosen to keep the statistical error within a few percents. To estimate the efficiency in Mon-
 383 tecarlo, a simple cut-and-count is done as recommended by the EGamma POG. In data, the
 384 selected events are fitted with a signal plus background model, and simultaneously for probes
 385 passing and failing the selection. A Montecarlo template convolved with a Gaussian is used as
 386 signal PDF for the nominal results, and an exponential function as background PDF. The sys-
 387 tematics related to the fit model are among the dominating ones. To evaluate them we change
 388 the signal or the background PDF separately and we consider the maximum difference from
 389 the nominal fit. The signal PDF is changed into an analytical fit with a Crystal Ball convoluted
 390 with the Z line-shape at NLO from Montecarlo. The background PDF instead is changed into
 391 a RooCMSShape.

392 In Figure 21 two example fits for the bin $50\text{ GeV} < p_T < 60\text{ GeV}$ and for bin $110\text{ GeV} < p_T <$
 393 150 GeV in the barrel can be seen.

394 Table 11 gives the efficiencies for data and Montecarlo together with the statistical and system-
 395 atic errors. **The systematic errors have not been updated with the latest statistics and are**
 396 **still those computed with 4.3 fb^{-1}** . The efficiencies and the ratio between data and Montecarlo
 397 are also shown in Fig 22. In both cases, for the endcaps results we restrict to the region up to
 398 $|\eta| < 2.1$. This choice is motivated by the fact that the signal is more central than Zs. Fig. 23
 399 shows the efficiency and the scale factors as a function of η of the probe photon.

400 Differently with respect to 2015, the scale factor is not compatible with 1 in all the p_T bins and
 401 as a result a data/MC scale factor has to be applied. We fit the scale factor curve (considering

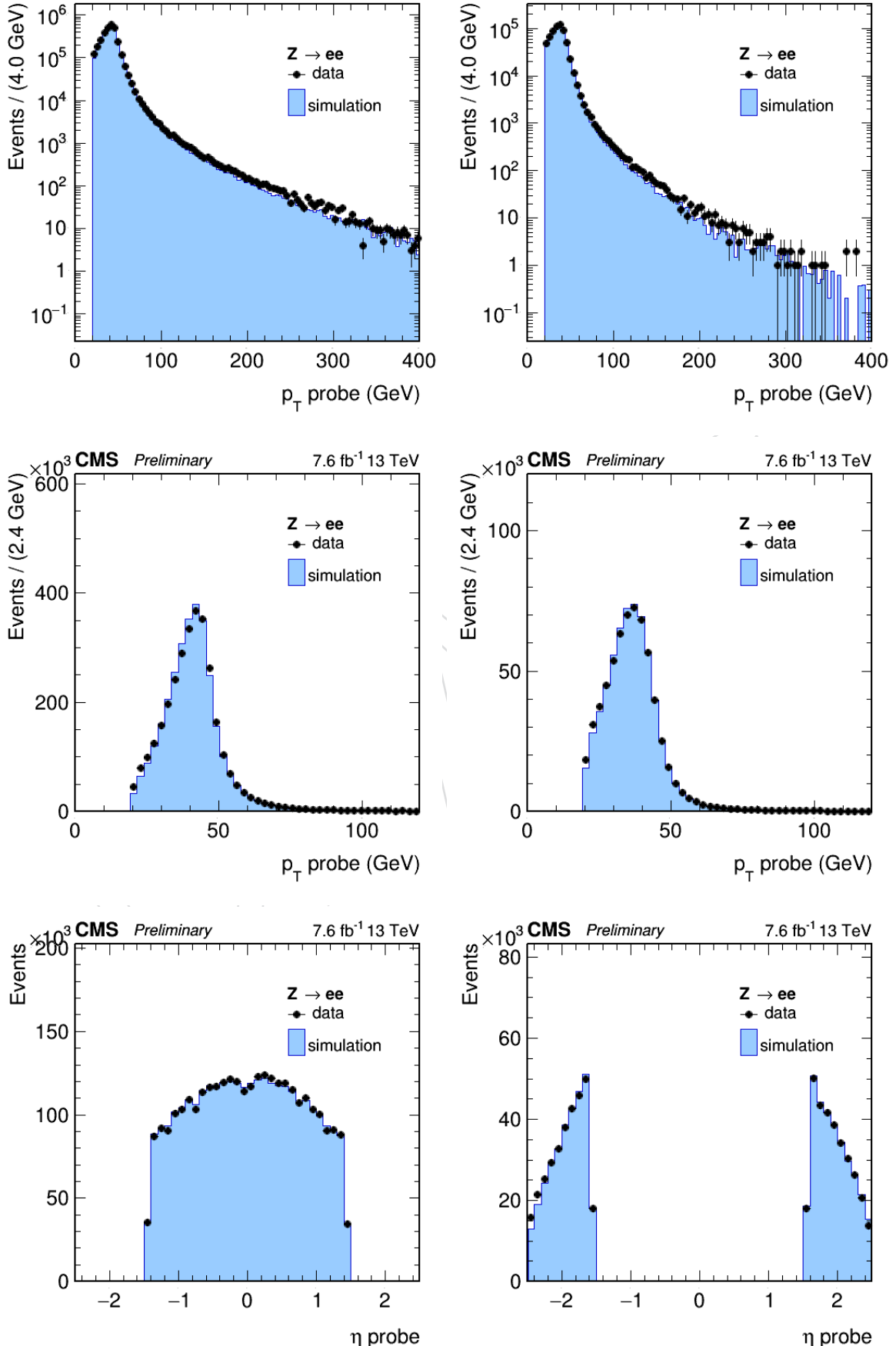


Figure 17: Transverse momentum (top and middle, in log and linear scale) and pseudorapidity (bottom) spectra of the probes. Probes in the barrel (endcaps) are shown on the left (right).

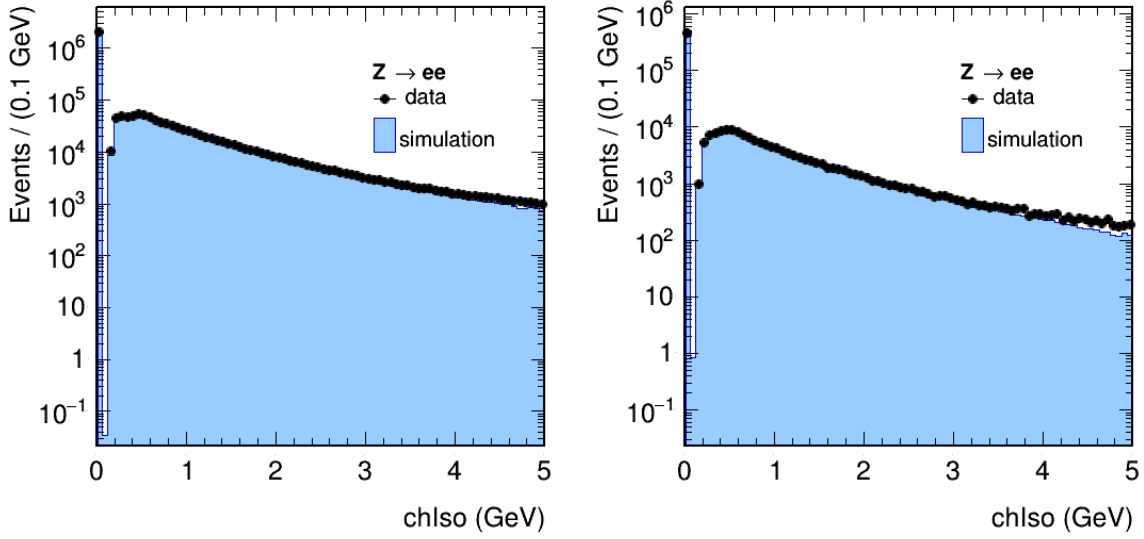


Figure 18: Charged component of the isolation for probe photons. Probes in the barrel (end-caps) are shown on the left (right).

Barrel		data			MC
p_T [GeV]	Efficiency	Stat.Err.	Syst.Err	Efficiency	
20-30	0.7887	0.0013	0.0293	0.8325	
30-40	0.8499	0.0004	0.0021	0.8813	
40-50	0.8804	0.0003	0.0013	0.9087	
50-60	0.8805	0.0007	0.0027	0.9110	
60-80	0.8763	0.0014	0.0104	0.9106	
80-110	0.8787	0.0030	0.0146	0.9104	
110-150	0.8887	0.0047	0.0045	0.9150	
150-200	0.8933	0.0076	0.0069	0.9161	
200-270	0.8963	0.0105	0.0117	0.9261	
270-350	0.8768	0.0185	0.0263	0.9257	
Endcap		data			MC
p_T [GeV]	Efficiency	Stat.Err.	Syst.Err	Efficiency	
20-30	0.6480	0.0021	0.0162	0.6831	
30-40	0.7294	0.0011	0.0070	0.7542	
40-50	0.7771	0.0010	0.0028	0.7974	
50-60	0.7940	0.0024	0.0009	0.8150	
60-80	0.8046	0.0041	0.0079	0.8291	
80-110	0.8305	0.0074	0.0094	0.8527	
110-150	0.8292	0.0120	0.0057	0.8656	
150-200	0.8372	0.0030	0.0177	0.8943	
200-350	0.9116	0.0142	0.0044	0.9162	

Table 11: Photon selection efficiency measured in barrel and endcaps up to $|\eta| < 2.1$ using the Tag and Probe method (all cuts except for electron rejection). **The systematic errors have not been updated with the latest statistics and are still those computed with 4.3 fb^{-1} .**

402 the statistical errors only) with a constant factor obtaining the numbers shown in table 12.

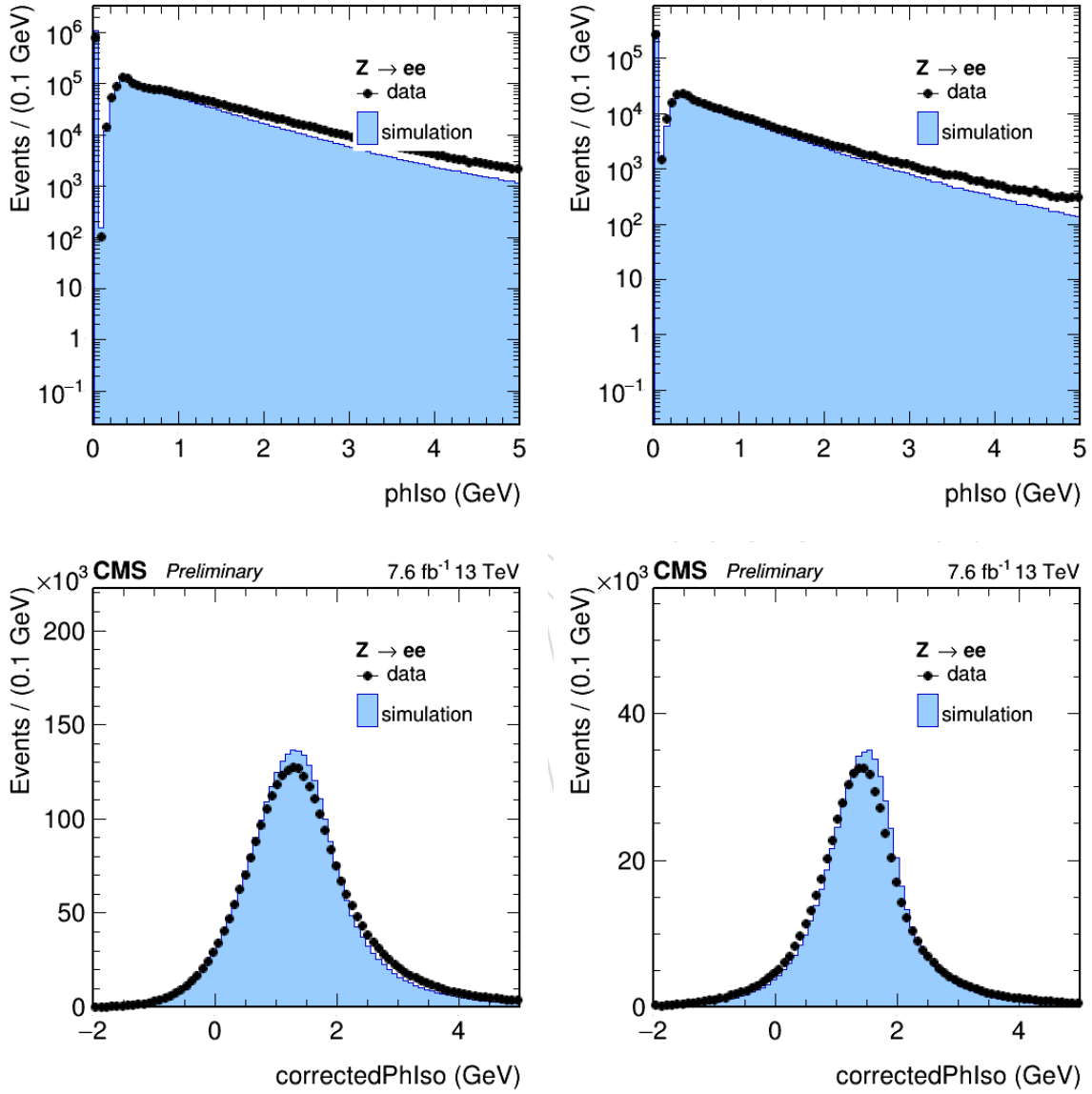


Figure 19: Photon component of the isolation for probe photons before (top) and after (bottom) the corrections for pileup and p_T discussed in the text. Probes in the barrel (endcaps) are shown on the left (right).

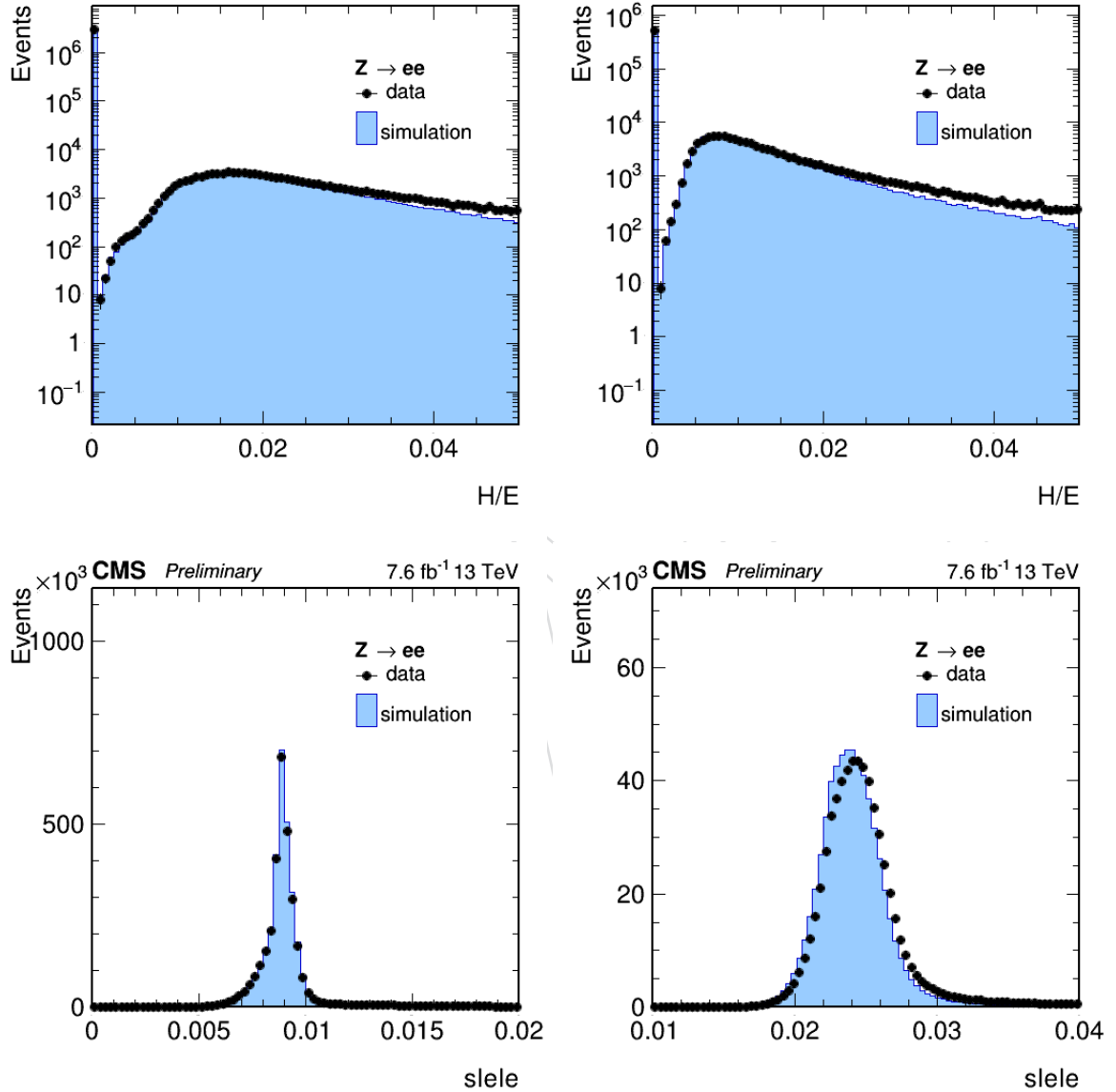


Figure 20: H/E (top) and $\sigma_{\eta\eta\eta}$ (bottom) distribution for probe photons. Probes in the barrel (endcaps) are shown on the left (right).

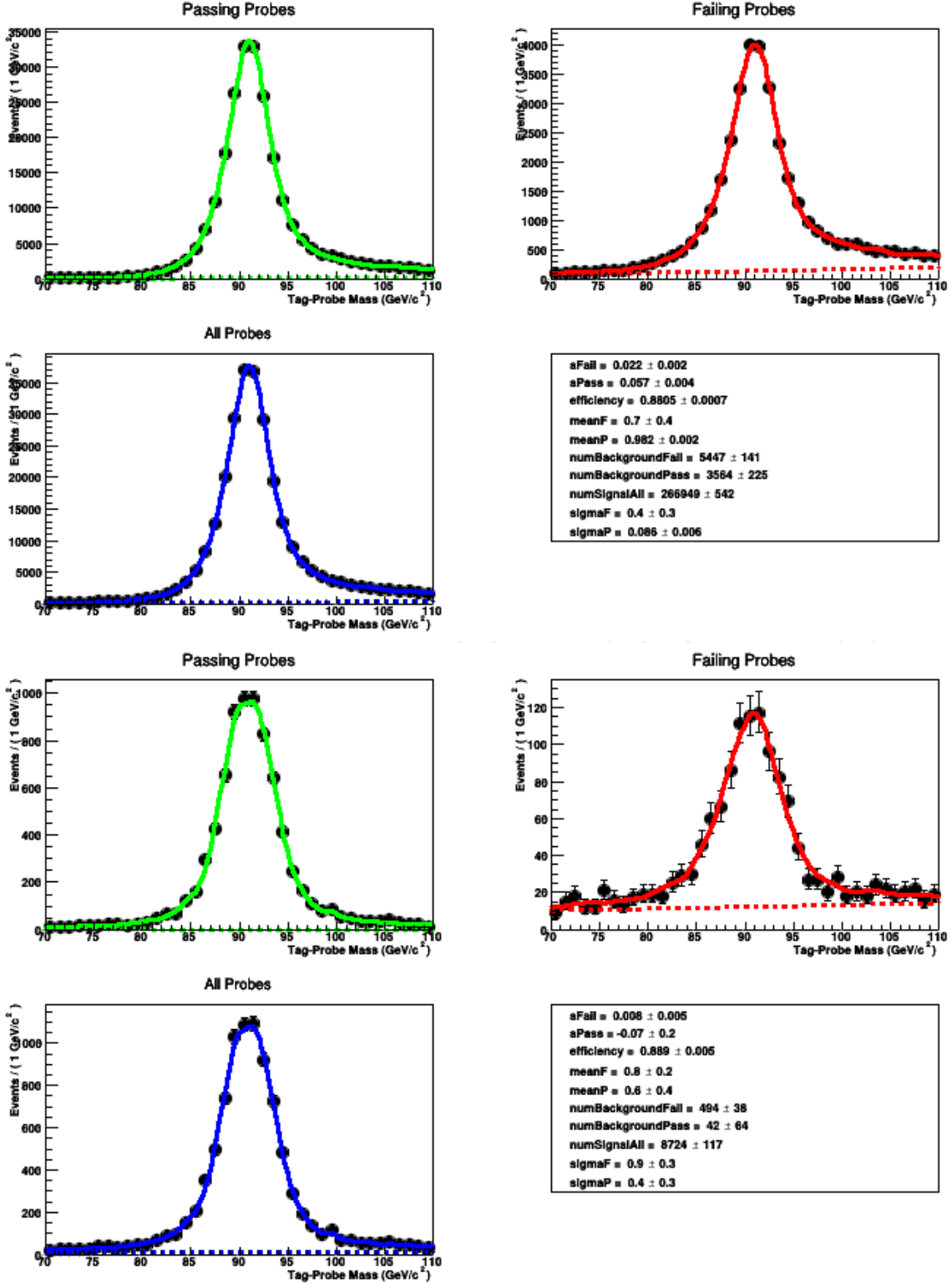


Figure 21: Two example fits for the bins $50 \text{ GeV} < p_T < 60 \text{ GeV}$ (top) and $110 \text{ GeV} < p_T < 150 \text{ GeV}$ (bottom). The signal and background shape are fitted as described in the text.

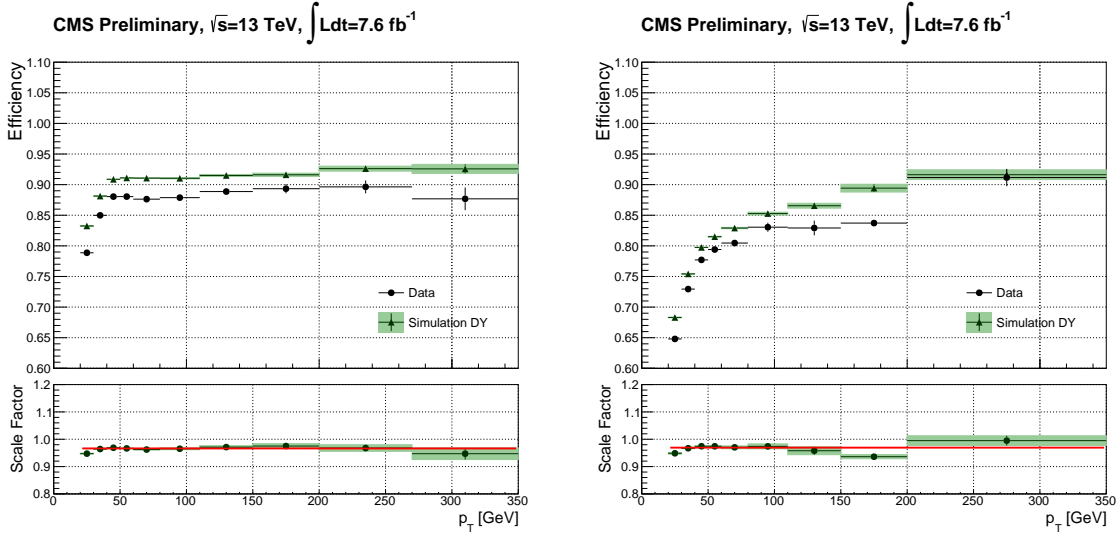


Figure 22: Top: Photon selection efficiency measured in barrel (left) and endcaps up to $|\eta| < 2.1$ (right) using the tag and probe method (all cuts except for electron rejection). Statistical errors only are shown. Bottom: data over Montecarlo scale factors.

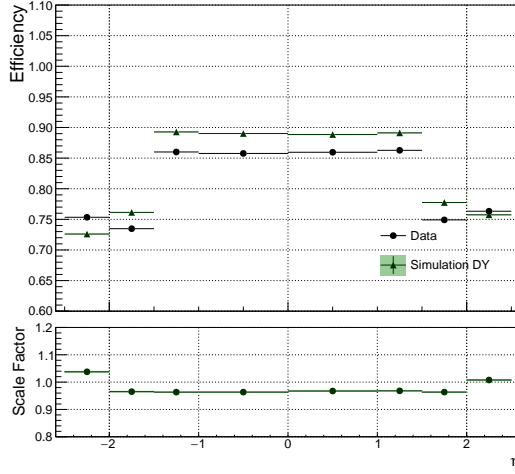


Figure 23: Photon selection efficiency measured using the tag and probe method as a function of the pseudorapidity (all cuts except for electron rejection). Statistical errors only are shown. Bottom: data over Montecarlo scale factors.

- 403 In order to understand the change in the scale factor with respect to 2015, we compared the
 404 distributions of the variables entering the selection in data and in Montecarlo for the two years.
 405 The variable which was found to have changed more is the photon component of the isolation,
 406 before and after the corrections for p_T and pileup discussed in this note. The distributions are
 407 compared in Fig. 24. We don't know the exact reason of this change. A possibility is the change
 408 in the ECAL selective readout, but we did not prove that. This comparison was performed on
 409 the first part of the dataset, with a luminosity corresponding to 4.3 fb^{-1} .
- 410 The data/MC scale factors and their uncertainties are propagated to the analysis. An uncer-
 411 tainty of 6% (3% per leg) is propagated to the signal model, which covers the scale factor which

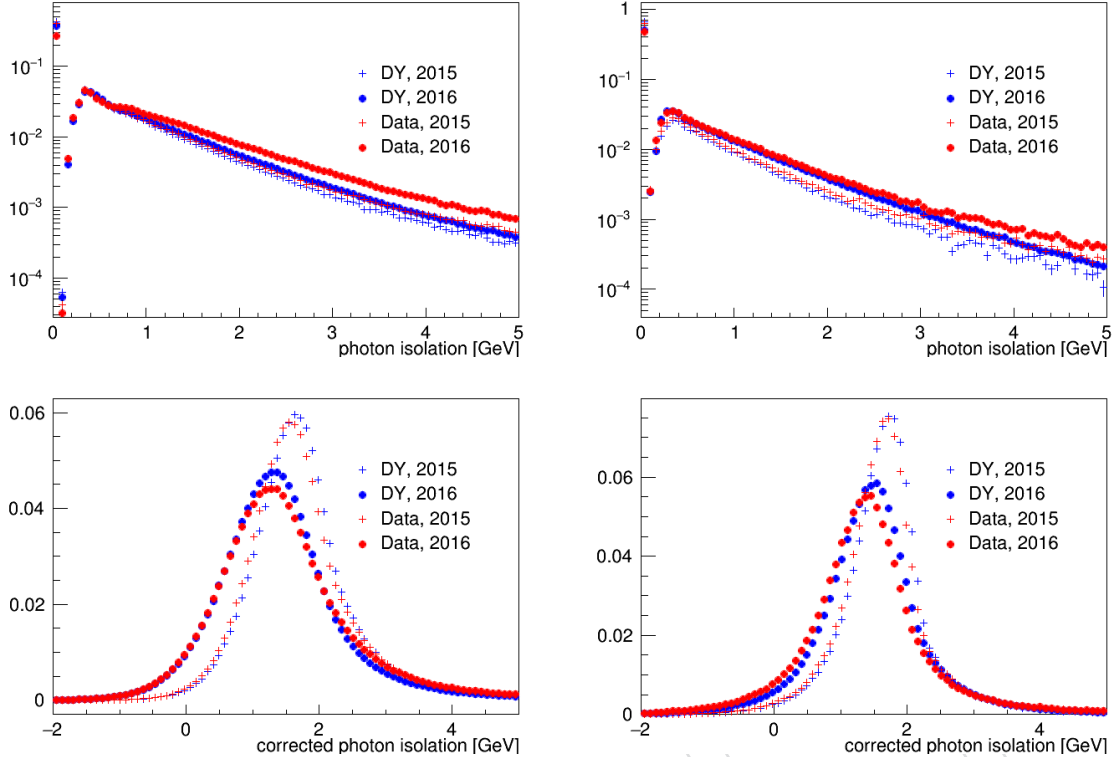


Figure 24: Comparison of the photon component of the isolation between the 2015 and 2016 datasets, in data and Montecarlo. Distributions before (top) and after (bottom) the corrections discussed in the text are shown for probe photons in the barrel (left) and in the endcaps (right).

Region	scale factor
$ \eta < 1.5$	0.9663 ± 0.0003
$1.5 < \eta < 2.1$	0.9695 ± 0.0009

Table 12: Result of constant fits as a function of p_T to the data to Montecarlo scale factors.

- 412 is measured and which may be assumed as a systematic itself.
 413 The electron veto scale factor is measured by the EGamma POG using $Z \rightarrow \mu^+ \mu^- \gamma$ events.
 414 Preliminary results are extracted from [19] and reported in Table 13.
 415 The final validation of both the energy corrections (scale and resolution) and the efficiency
 416 scale factors is performed with the $Z \rightarrow ee$ events compared to the simulated DY sample. The
 417 available simulated sample do not include trigger emulation, for this reason the loose electron
 418 ID provided by the EGamma group is applied as preselection to both data and MC, requiring
 419 that at least one of the two electrons pass the loose electron ID. Without the loose preselection
 420 an events deficit of $\sim 4\%$ was observed in data when comparing it to the simulation. The data
 421 to MC scale factors for the loose electron ID is compatible with 1 for both EB and EE electrons
 422 and has been derived by the EGamma group with the usual tag and probe method. Therefore
 423 only the scale factors related to the analysis selections are applied to the simulation (0.94 and
 424 0.96 for EBEB and EBEE category respectively). Figure 25 shows the final comparison for the
 425 two analysis category, the agreement between data and simulation is found to be very good
 426 after both the energy corrections and selection efficiency scale factors are applied.

	Data		Simulation		Ratio	
	Eff.	Stat.	Eff.	Stat.	Eff.	Unc.
Barrel; $R_9 > 0.85$	0.9935	0.0012	0.9974	0.0009	0.9961	0.0015
Barrel; $R_9 < 0.85$	0.9738	0.0040	0.9837	0.0041	0.9899	0.0058
Endcap; $R_9 > 0.90$	0.9850	0.0029	0.9852	0.0026	0.9998	0.0040
Endcap; $R_9 < 0.90$	0.9534	0.0181	0.9623	0.0131	0.9908	0.0232

Table 13: Efficiency of the conversion-safe electron veto measured in the context of the $H \rightarrow \gamma\gamma$ analysis [19]. The data to simulation ratio is also shown with its uncertainty.

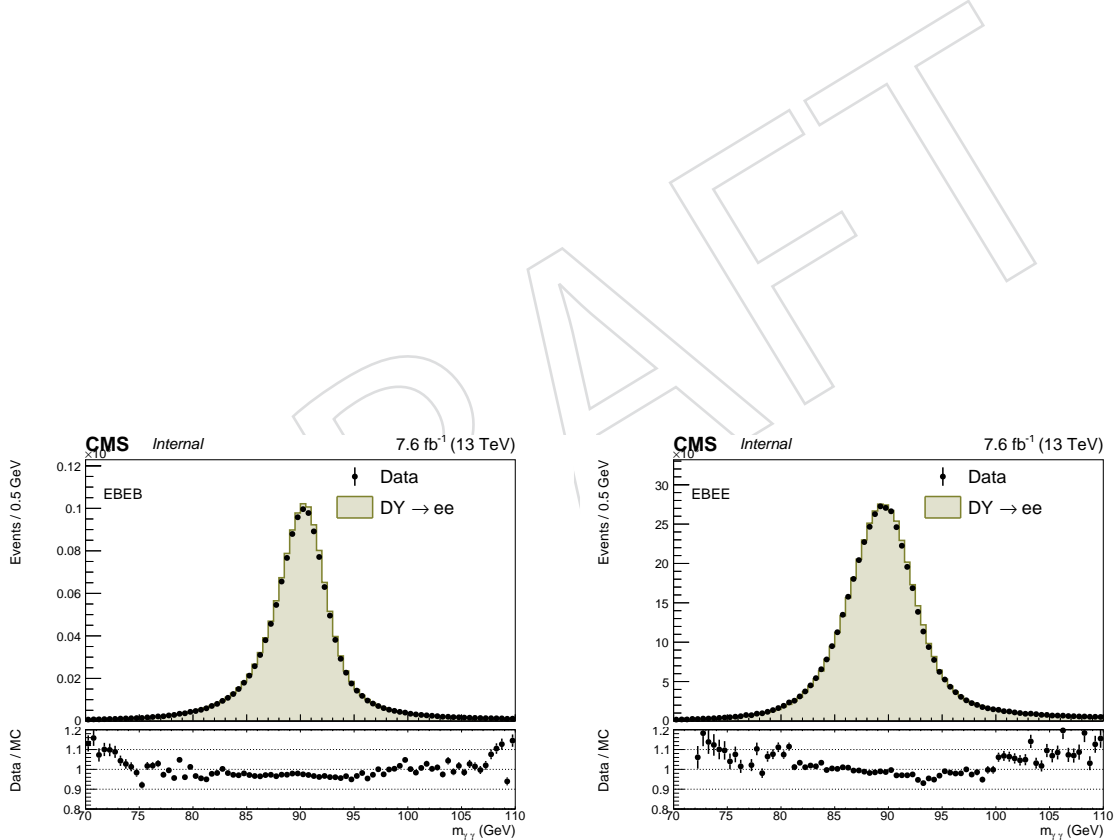


Figure 25: Invariant mass distribution of the events used to check the energy scale and resolution corrections and the selection efficiency scale factors. (left) events with both electrons in the barrel region, (right) events with one electron in the barrel region and one in the endcaps.

427 7 Background composition control from data

428 Still to be updated to 7.6 fb^{-1}

429 In order to validate the simulation of the analysis background processes, data driven techniques
 430 are used to estimate the fraction of reducible and irreducible backgrounds. The estimated
 431 irreducible background is then compared with the NNLO QCD predictions.

432 The irreducible background consists of two prompt photons ($\gamma\gamma$). For the reducible back-
 433 ground, at least one photon candidate is a jet j , misidentified as a photon. The corresponding
 434 background fractions are denoted as γj and jj . The fractions of those three background com-
 435 ponents are estimated using a template fit to data. Three 2-dimensional templates are built,
 436 each dimension describing the charged particle flow isolation of one of the two photons. The
 437 following section concentrates on the construction of those templates, which are directly built
 438 from data.

439 The diphoton events used in the template fit, passed the same kinematic selection and photon
 440 ID cuts as detailed in section 3.3, except for the charged particle flow (IsoCh) requirement that
 441 is relaxed to 15 GeV. The number of the diphoton events for 7.6 fb^{-1} are listed in Table 14.

Table 14: Number of diphoton events for 7.6 fb^{-1} .

	EBEB ($m_{\gamma\gamma} > 230 \text{ GeV}$)	EBEE ($m_{\gamma\gamma} > 320 \text{ GeV}$)
diphoton events	2588 ± 51	1340 ± 137

442 The chosen template variable is the charged particle flow isolation as it gives good discrimi-
 443 nation power between prompt (γ) and fake (j) photons and it has a small pile-up dependence.
 444 Prompt photons have mostly a charged particle flow isolation lower than 5 GeV. The enlarged
 445 range can thus be used to describe the fake photons.

446 For isolated prompt photons, we expect the isolation to be mostly around values near zero.
 447 The template binning is consequently chosen such that the first bin has the range $0.0 - 0.1 \text{ GeV}$
 448 to contain all well isolated photon candidates. The next range ($0.1 - 5 \text{ GeV}$) reflects the cut on
 449 the signal region at 5 GeV. The last bin ($5 - 15 \text{ GeV}$) contains mostly fakes. To evaluate the
 450 influence of the binning, the number of bins is reduced to two bins ($0 - 5 \text{ GeV}$ and $5 - 15 \text{ GeV}$)
 451 for a dedicated study and the result is taken as a systematic error.

452 7.0.1 Prompt-prompt template with the random cone method

453 The building of the prompt-prompt ($\gamma\gamma$) templates relies on the assumption that the prompt
 454 photon is isolated and the only activity in its isolation cone is due to underlying event, pile-
 455 up and ECAL electronic noise. Exactly the same method as in 2015 is used. The random cone
 456 technique takes the η -coordinate of the photon and throws a new isolation cone with a random
 457 angle in ϕ . The ϕ -angle is between 0.8 and $2\pi - 0.8$ radians to assure that the isolation cones
 458 with a size of $\Delta R < 0.4$ do not overlap with each other. The random cone is taken if no jet
 459 with $p_{t,jet} > 30 \text{ GeV}$ or photon with $p_{t,\gamma} < 10 \text{ GeV}$ is found inside the cone. This random cone
 460 technique is applied up to 9 times on the respective $\gamma\gamma$ -diphoton events in data to increase
 461 the statistics. Figure 26 shows the comparison of the $\gamma\gamma$ component in Monte Carlo truth, the
 462 charged particle flow isolation of the random cones from the MC dataset and from the dataset
 463 for 7.6 fb^{-1} . The random cone isolation of the lead and sub-lead photon is randomly switched
 464 on the axes for EBEB, where both photon candidates are centrally detected. The distribution
 465 of the left and right plot is as such the same by definition and only the first axis is shown in
 466 the left plot of Figure 26. For the barrel-end cap category, the random cone isolation of the
 467 barrel photon candidate is projected on the first axis (right plot in Figure 26), the random cone

isolation of the endcap photon candidate on the second axis. The charged particle flow isolation is normalized to the area and each bin and its error are then divided by the bin width to have a comparison of the different number of entries for the individual bins. The original dataset includes also fake photons. As random cones are thrown from each event, also from the ones with misidentified jets, the resulting error is part of the final non-closure in MC.

The method works, if MC truth and the charged particle flow isolation in MC show a good agreement. For barrel-barrel and barrel-endcap, the first two bins show an excellent agreement within 1σ for both legs as visible in the ratio plot. A slight offset in the first bin of about 5% is part of the final MC non-closure. The third bin has in all cases much less entries as this bin of the extended range is mostly populated by fake photon candidates.

As such it is expected, that the $\gamma\gamma$ -component in this bin is nearly zero and a disagreement of MC truth and the $\gamma\gamma$ -template from the MC dataset is not influencing the final 2-dimensional fit.

The templates, in particular the number of entries per bin, are statistically constrained. The jack-knife method is used to estimate the resulting uncertainty. It is described in the last part of this section.

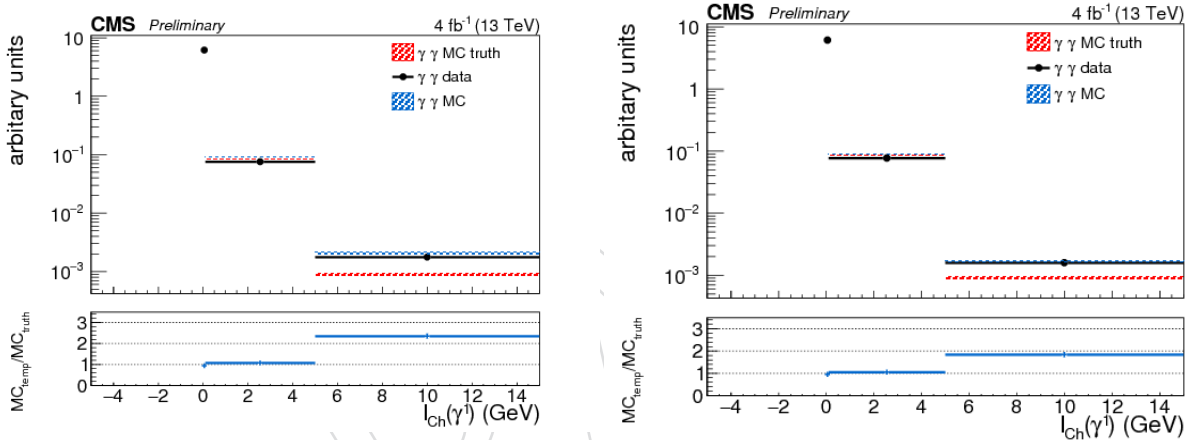


Figure 26: Projection of charged particle flow isolation of the first leg for $\gamma\gamma$ -templates in EBEB (left) and EBEE (right) for the full $m_{\gamma\gamma}$ range.

The estimate of the fractions of the different background components will be used for a final semi-parametric fit in a future analysis. In preparation to this, it is useful to "unroll" the 2-dimensional templates to a 1-dimensional histogram. A sketch of the method can be seen in Figure 27

The bin content of each bin of the 2-dimensional histogram is normalized to the area and projected on a 1-dimensional axis. The result for the $\gamma\gamma$ -template can be seen in Figure 28. A bin width of 1 is chosen to study the agreement between MC truth and MC templates and templates in data.

The first four bins correspond to the signal region of the analysis with a charged particle flow isolation of < 5 GeV. The same agreement within 1σ as for the first two bins of the 1-d projection can be observed. For the first bin, the offset of the first bins of the 1-d templates add to a final offset of about 15%. Bin 4-9 depict the enlarged charged particle flow isolation range ($I_{isoCh} < 15$ GeV). As the number of events in those bins is largely reduced, bin 7, the least populated bin, does not contain any events in data for the EBEB category. Also, for this region, the disagreement in MC becomes larger. For the 2-dimensional fit, this range is used to estimate the fake contribution. The disagreement has thus a negligible influence. The uncertainty on the MC templates and the MC truth is in some bins not of the same size. The reason for

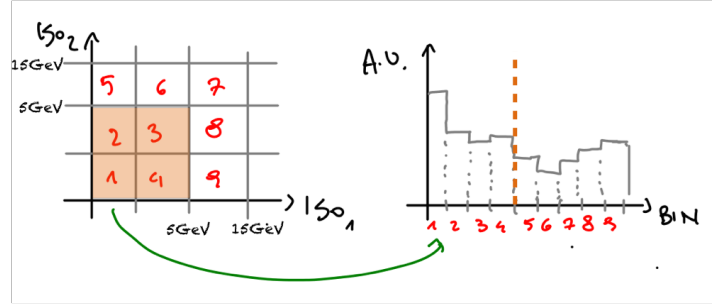


Figure 27: Sketch how the bin content of the 2-d charged particle flow isolation histogram is unrolled on a 1-d histogram.

the variations in the error bars is tracked down to a corresponding variation in the weight of the MC events used to produce the plot. When scaled to the integrated luminosity in data, the bulk of the events have fractional weights, while a small tail have weights of the order of a bit less than unity. If events with a high weight are disregarded, the size of the error bars agree in MC. This explains for example the disagreement in MC truth and the slight variation in the MC templates between the two legs in the third bin in EBEB which should be by construction the same.

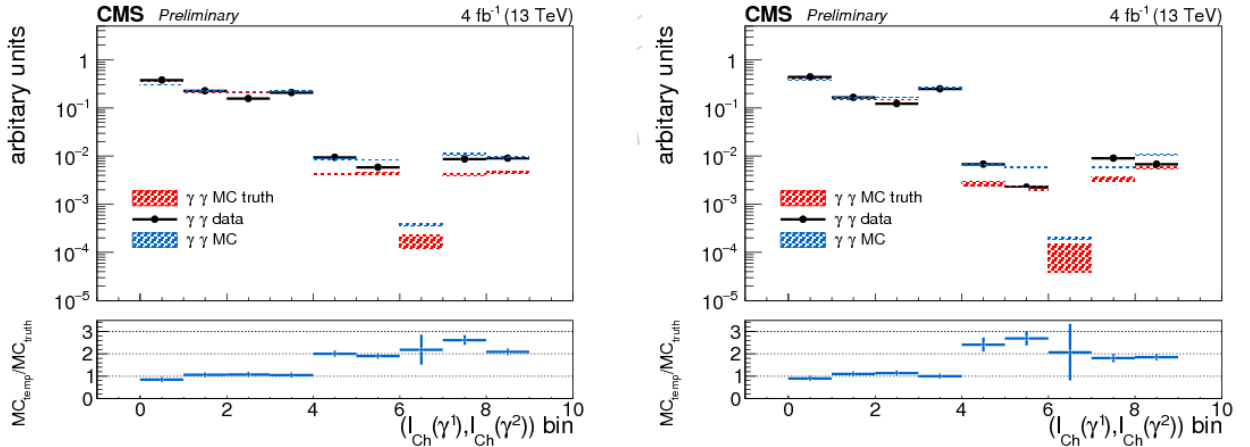


Figure 28: 1d-projection of 2-d charged particle flow isolation for $\gamma\gamma$ -templates in EBEB and EBEE for the full $m_{\gamma\gamma}$ range.

509 7.0.2 Fake template with the $\sigma_{i\eta i\eta}$ -sideband method

The template for the fake photon candidates, mainly jets passing the photon ID cuts, is built with the $\sigma_{i\eta i\eta}$ -sideband method. Fake-photon candidates need to have a $\sigma_{i\eta i\eta}$ -value below a certain $\sigma_{i\eta i\eta}$ -sideband cut. Additionally, the cut on the corrected photon isolation (Iso_{γ}) is slightly relaxed compared to the working point in the signal region (section 3.3). The sideband definition of the two categories is listed in table 15.

Table 15: Sideband definition for fake templates.

category	$\sigma_{i\eta i\eta}$	$\text{Iso}_{\gamma} \text{ GeV}$
EB	> 0.0112	< 4.5
EE	> 0.0300	< 13.5

515 The events need to have a $\sigma_{i\eta i\eta}$ -value smaller than 0.0112 for EB (0.030 for EE) to enter the
 516 sideband selection. If they have a value of $\sigma_{i\eta i\eta} > 0.0105$ for EB (0.028 for EE) they enter the
 517 signal selection and non-saturated photon events with a $\sigma_{i\eta i\eta}$ value in-between those two are
 518 not entering any selection to avoid prompt-photon contamination in the sideband.

519 The sideband definition is first evaluated on the single photon datasets. For MC, the full back-
 520 ground dataset as listed in table 3 is used. In data, the single photons are taken from the
 521 single-photon MiniAOD dataset, passing the same photon ID cuts as the photons of the dipho-
 522 ton event, but an additional transverse momentum cut of $p_t = 170 \text{ GeV}$ is applied, to avoid
 523 turn-on effects of the trigger. Prompt photons are photons which matched on generator level
 524 and have a $\text{genIso} < 10 \text{ GeV}$. To study the influence of a different $\sigma_{i\eta i\eta}$ -sideband definition,
 525 the working points were changed to $\sigma_{i\eta i\eta} > 0.012$ for EB and $\sigma_{i\eta i\eta} > 0.032$ in Ref. [17]. The
 526 resulting difference in the final fit is part of the final systematic error 27.

527 This sideband definition gives a reliable fake template for the charged particle flow isolation
 528 as both variables are only slightly correlated. The correlation is part of the final non closure in
 529 MC.

530

531 Templates from event mixing

532 With the chosen sideband definition, the 2-dimensional templates for the prompt-fake (γj) and
 533 fake-fake (jj) component would not contain enough events to describe the background compo-
 534 nents correctly, especially in the high p_t region.

535 By the time of the freezing for the approval, not all QCD-EM enriched MC samples were pro-
 536 duced yet. The jj -component is thus missing in the MC templates and MC truth.

537 To enrich the fake component and to build a high statistics 2-dimensional template, the k-
 538 Nearest-Neighbour algorithm is used. With this method, the photons of the diphoton event are
 539 matched to photons from a single photon selection with similar phase space values. Hereby,
 540 the correlations between the two legs are taken into account.

541 The matching is performed with variables of a "n-dimensional" phase space which include the
 542 most influential variables for the diphoton events:

- 543 • EBEB: the logarithm of the transverse momentum $\log(p_T)$, the pseudo-rapidity η
 544 and the number of vertices.
- 545 • EBEE: the logarithm of the transverse momentum $\log(p_T)$, the pseudo-rapidity η
 546 and the corrected photon isolation Iso_{γ} .

547 The photon isolation is looser in EBEE than in EBEB, thus its inclusion in the matching criteria.
 548 This inclusion was associated with the exclusion of the matching in number of vertexes to limit
 549 the number of variables. For the γj -template, the prompt photon candidate is taken from the
 550 prompt single photon selection and the random cone method is applied to estimate the charged
 551 particle flow isolation.

552 Photons in the sideband are matched to the sideband selection of the single photons. A sub-
 553 sample of $k = 10$ similar single photon events is built. Each variable of the n-dimensional
 554 matching tree is now integrated to a cumulative distribution function (cdf) to have a com-
 555 parable metric for the matching. Each photon of the diphoton event is then matched to the
 556 single photon event with the smallest cdf distance. This matching is performed with the Near-

557 est Neighbour algorithm. On top of that, the correlations of the photons in a γj -diphoton event
 558 are taken into account. These were studied with the Monte Carlo truth information:

559

- 560 • **prompt-fake template:** for EBEB, the prompt photon is with a probability of 80 %
 561 the leading photon.
- 562 • **prompt-fake template:** for EBEE, the prompt photon is with a probability of 56 % in
 563 the barrel.

564 Both values are varied by 10% for the final systematic error for the fractions of the background
 565 components. After the event mixing, the two template variables are projected on the two axes
 566 as described for the $\gamma\gamma$ -templates.

567 The event mixing leads to γj - and jj templates which have $k = 10x$ more events than data
 568 and the highly enriched samples are used subsequently for the fit to determine the reducible
 569 background.

570 The "mixed" charged particle flow isolation templates are compared to MC truth to proof that
 571 the method works. The projection on the first photon leg can be seen for EBEB (EBEE) in the
 572 left (right) plot in Figure 29. The charged particle flow isolation is normalized to 1 and each bin
 573 and its error are then divided by the bin width. For the prompt-fake and fake-fake templates
 574 the same projection is applied as for EBEB and EBEE for the prompt-prompt template. For
 575 the category, where the prompt photon and fake photon candidate are in the barrel, the ran-
 576 dom cone isolation of the lead and sub-lead photon is randomly switched on the axes. For the
 577 barrel-end cap case, the random cone isolation of the barrel photon candidate is projected on
 578 the first (right in Figure 29), the one of the endcap photon candidate on the second axis. Both
 579 categories show a good agreement between MC truth and the enriched γj -templates within 1σ
 580 for all bins. The uncertainty on the MC templates and the MC truth is in some bins not of the
 581 same size. The reason for the variations in the error bars is tracked down to a corresponding
 582 variation in the weight of the MC events used to produce the plot. When scaled to the data
 583 integrated luminosity, the bulk of the events have fractional weights, while a small tail have
 584 weights of the order of unity. If events with a high weight are disregarded, the size of the error
 585 bars agree in MC. This explains for example the disagreement in MC truth and the slight vari-
 586 ation in the MC templates between the two legs in the third bin in EBEB which should be by
 587 construction the same.

588 Given that the method works in MC, the approach can be applied on data. Also the the data
 589 MC comparison shows a good agreement for both categories.

590

591 Also the γj -templates are "unrolled" in 1-dimension (Figure 30). The such unrolled charged
 592 particle flow isolation for barrel-barrel shows for most bins a very good agreement within their
 593 uncertainties, as expected from the 1-d projection on the legs. The less populated bins show the
 594 larges disagreement. The data follows the MC prediction in all bins within their uncertainties.
 595 The agreement proofs that the event-mixing describes the physics of the γj -templates correctly.
 596 As for the $\gamma\gamma$ -templates, the shape of the γj -templates, the number of entries per bin, is sta-
 597 tistically constrained. To estimate this systematic error on the final background fractions, the
 598 jack-knife method is again applied and described in the following section.

599 Due to the missing QCD-EM prediction in MC, the jj -component could not yet be determined,
 600 but based on previous studies it is expected to be below 5 % for the full $m_{\gamma\gamma}$ range.

601 The binning is chosen such that the statistical error in data does not exceed 10% for most bins
 602 for low luminosities.

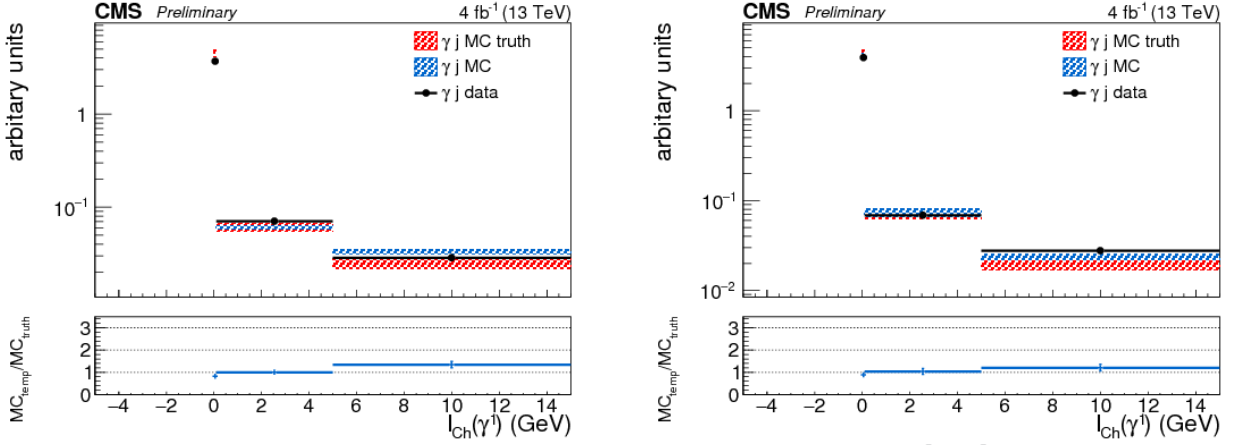


Figure 29: Projection of charged particle flow isolation of the first leg for γj -templates in EBEB (left) and in EBEE (right) for the full $m_{\gamma\gamma}$ range.

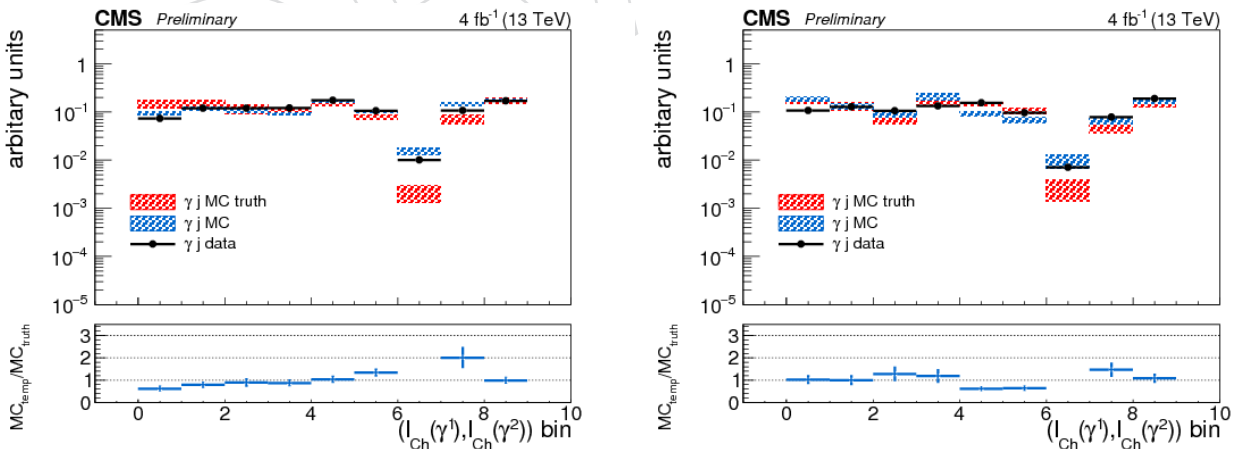


Figure 30: 1d-projection of 2-d charged particle flow isolation for γj -templates in EBEB and EBEE for the full $m_{\gamma\gamma}$ range.

- 603 • 9 bins in EBEB (GeV): [230,253,282,295,332,409,500,600,800,1600]
 604 • 6 bins in EBEE (GeV): [320,356,444,500,600,800,1600]

605 7.0.3 Estimate of purity fraction for the extended Iso_{Ch} range in data

With the above described charged particle flow isolation templates, a breakdown of the individual background components in different bins of mass is performed. The 1-dimensional "unrolled" shapes of the three $\gamma\gamma$, γj , jj templates are fitted to data and compared to the Monte Carlo truth information. These data-driven histograms give an estimate of the amount of irreducible and reducible background. The likelihood fit has the following form:

$$L(data|f_{\gamma\gamma}, f_{\gamma j}, f_{jj}) = \prod_{i=1}^{Nbins} (f_{\gamma\gamma} \cdot T^{\gamma\gamma}(\text{Iso}_{Ch,i,1}, \text{Iso}_{Ch,i,2}) + f_{\gamma j} \cdot T^{\gamma j}(\text{Iso}_{Ch,i,1}, \text{Iso}_{Ch,i,2}) + f_{jj} \cdot T^{jj}(\text{Iso}_{Ch,i,1}, \text{Iso}_{Ch,i,2}))^{n_i} \quad (1)$$

The sum of the final fractions $f_{\gamma\gamma}$, $f_{\gamma j}$, f_{jj} is by construction 1. The parametrization of the coefficients is defined recursively to improve the stability of the fit.

$$L(data|c_1, c_2, c_3) = c_1 \cdot PDF_{\gamma\gamma} + (1 - c_1) \cdot (c_2 \cdot PDF_{\gamma j} + (1 - c_2) \cdot c_3 \cdot PDF_{jj}) \quad (2)$$

- 606 This is necessary as the pdf of the jj -component evaluates in some mass bins zero. For illustration, two examples fits in data for the lowest $m_{\gamma\gamma}$ bin in EBEB and the highest $m_{\gamma\gamma}$ bin in
 607 EBEE can be seen in Figure 31. The first 4 bins give an estimate of the $\gamma\gamma$ -component, the
 608 last 5 bins describe the γj -component (see also the sketch in Figure 27). The jj -component is
 609 nearly zero in all bins. The fit uncertainty is quantified with asymmetric errors using MINOS.

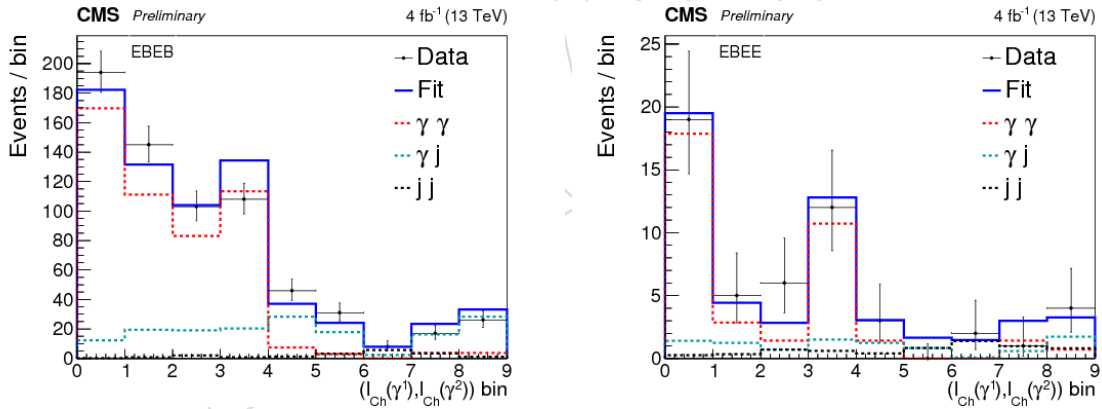


Figure 31: Example of a fit with the three components $\gamma\gamma$, γj , jj for the lowest (left) and highest (right) mass bin in EBEB (EBEE) in data.

- 610 Towards higher masses, the $\gamma\gamma$ -component is very high and has a coefficient of nearly one, in
 611 those cases the MINOS error calculation fails and the Clopper-Pearson interval is used for the
 612 error calculation. Details about the systematic error can be found in the appendix G. The sum
 613 in quadrature of all errors lead to a total systematic error of 9% for barrel-barrel and 11% for
 614 barrel-endcaps.
 615

616 7.0.4 Extrapolation of background fractions to signal region

- 617 The goal of this study is to breakdown the individual background components to better de-
 618 scribe the background in $m_{\gamma\gamma}$. For this estimate, the fractions of the three components in the

619 signal region ($\text{Iso}_{\text{Ch}} < 5 \text{ GeV}$) has to be known. The fractions f , fitted for the extended charged
 620 particle flow isolation range ($\text{Iso}_{\text{Ch}} < 15 \text{ GeV}$) are taken and calculated for the signal region by
 621 multiplying them with the ratio of the integral of the respective component divided by the full
 622 background pdf.

$$f_{\text{sigRegion}} = f_{\text{fullRegion}} \cdot \frac{\int_{\text{sigRegion}} \text{pdf}_f}{\int_{\text{sigRegion}} \text{pdf}_{\text{full}}} \quad (3)$$

623 The results are depicted in Figure 32 and Figure 33 for EBEB and EBEE respectively. The purity
 is shown with the systematical error (full area) and the total error (lines). The fraction of the

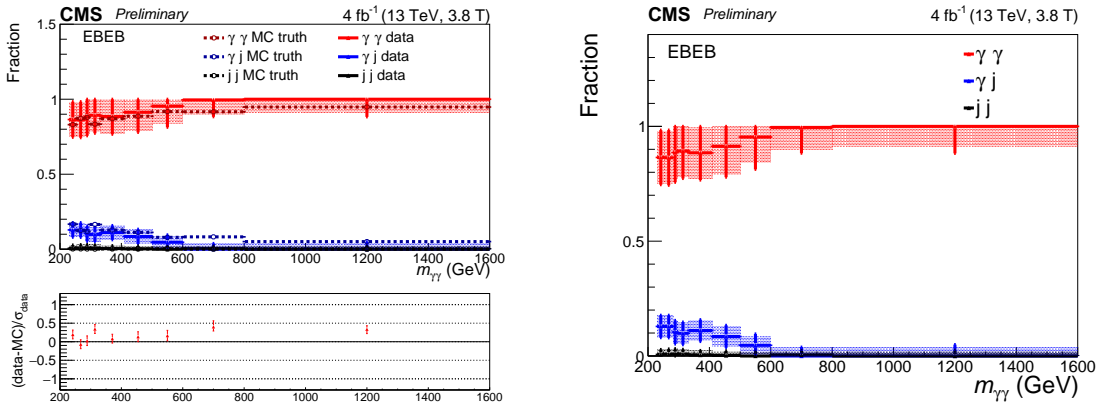


Figure 32: Fraction of the background components for $\text{Iso}_{\text{Ch}} < 5 \text{ GeV}$ to the overall background in MC (left) and in data (right) for EBEB.

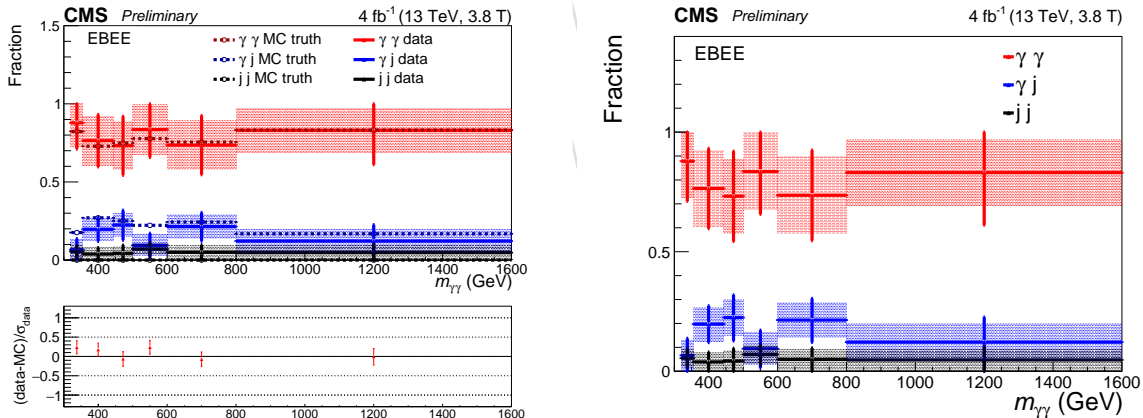


Figure 33: Fraction of the background components for $\text{Iso}_{\text{Ch}} < 5 \text{ GeV}$ to the overall background in MC (left) and in data (right) for EBEE.

624 irreducible background is higher than for the extended charged particle flow isolation range.
 625 It is roughly around 90 %, increasing to > 95% for higher $m_{\gamma\gamma}$ values in EBEB, and 80 %,
 626 increasing to > 85% for higher $m_{\gamma\gamma}$ values in EBEE. The statistical error of the fractions of the
 627 background components in the signal region $\sigma_{\text{stat,sig}}$ is the propagated error of the statistical
 628 error of the fractions of the full range and the jack-knife error.
 629 It is assumed that the systematic error is on average flat over all charged particle flow isolation
 630 bins. This is also done to avoid picking up fluctuations in MC. If the systematic error is flat,
 631 it can be calculated for the background fractions in the signal region by propagating the error
 632 from the full range.
 633

634 **7.0.5 Comparison between measured and predicted $\gamma\gamma$ component**

Using the results of the parametric fits described above, the mass spectrum of the irreducible $\gamma\gamma$ background component can be extracted from data, simply taking the product between $f_{\gamma\gamma}$ and the number of events observed in each of the $m_{\gamma\gamma}$ bins.

$$N_{data}^{\gamma\gamma}(bin) = f_{\gamma\gamma} \cdot N_{data}(bin)$$

635 The resulting spectrum was compared to the expectation from perturbative QCD. The latter
 636 was obtained rescaling the LO fully simulated Sherpa sample to the NNLO prediction obtained
 637 with the 2gNNLO program, as explained in Ref. [17].

638 The result of the comparison is reported in Fig. 34. The predictions from perturbative QCD
 639 match well the observation for the EBEB category, while a small under-prediction is observed
 for the EBEE.

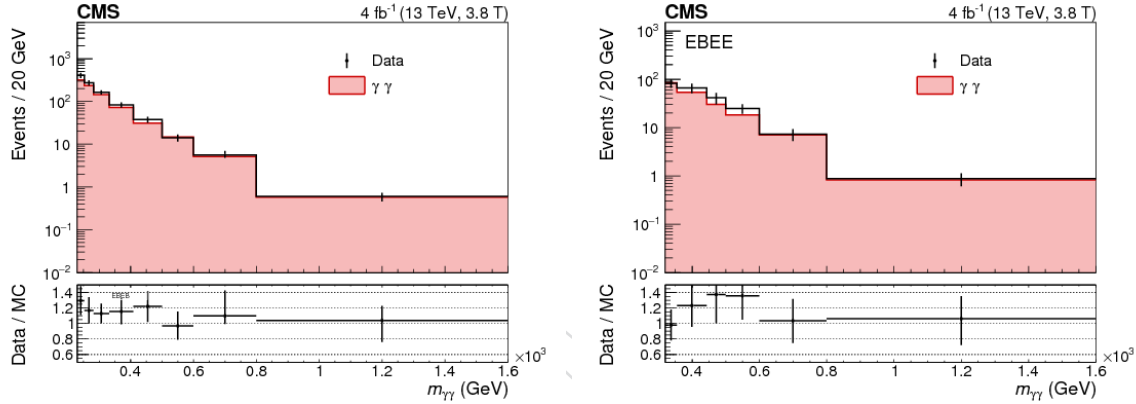


Figure 34: Comparison between the predicted and measured $\gamma\gamma$ background spectrum. Events in the EBEB (EBEE) category are shown on the left (right).

640

641 8 Parametric Signal Model

642 In order to statistically interpret the data, it is necessary to have a description of the signal
 643 which specifies the shape of the diphoton mass distribution in each category as well as the
 644 efficiency \times acceptance. So far the signal shape was described by a non-parametric model ex-
 645 ploiting smeared histograms, which is detailed in Sec. 9. This section describes a novel tech-
 646 nique used to describe the shape of the resonant diphoton signal exploiting a parametric model.
 647 The change from a histogram-based model to a parametric shape allows us to perform a finer
 648 scan of the investigated mass without the need of generating an infinite number of signal points
 649 and keeping the size of the input workspaces relatively small. It also makes easier to have a
 650 two-dimensional model describing both mass and width of the resonance.

651 The Monte Carlo is used, after the smearing of the resolution, and the application of all effi-
 652 ciency corrections and scale factors, to build a model for the signal. The strategy is to describe
 653 the simulated signal with an analytic function in which the hypothetical signal mass (m_X) rep-
 654 resents a parameter which can vary continuously for any value in the range of interest of the
 655 search. This can be extended in a simple fashion to allow for an additional free parameter, the
 656 natural width of the new resonance, Γ_X , performing the parametrization of the signal model
 657 also as a function of the width.

- As first step the response distribution of the reduced mass (Δm) is computed for each available reconstructed mass point ($m_x = 500, 750, 1000, 1250, 1500, 1750, 2000, 2250, 2500, 2750, 3000, 4000$ GeV) as the difference between the reconstructed diphoton mass in the event (m_{reco}) and the true mass (m_{true}) of the event:

$$\Delta m = m_{reco} - m_{true} \quad (4)$$

- In order to construct the parametric model the response distribution is fitted with an analytic function, namely a double-sided Crystal-Ball function with mean m_0 , sigma σ and two asymmetric tails defined by two different different n and α parameters. The Crystal-Ball function (CB) $f_{CB}(x)$ combines a Gaussian core and a power-law tail with an exponent n to account for photon energy loss due to pair production. The parameter α defines the transition between the Gaussian and the power-law functions. In Figure 35 the fit to the reduced mass is shown for the signal mass point $m_X = 750$ GeV.
- The theoretical signal line shape of the X resonance is described by the functional form of a relativistic Breit-Wigner centered at m_X and with the expected natural width for a resonance of Γ_X . The Breit-Wigner distribution is fitted in this analysis with a double-sided crystal-ball. The results of the fit are shown in Figure 36 for $m_X = 750$ GeV.
- The theoretical line-shape fit function is convoluted with the response fit function to account for the experimental resolution of the ECAL. The convoluted shape is compared with the reconstructed mass shape as a closure test of the fitting model. The closure test is shown in Figure 37 for $m_X = 750$ GeV.
- The convoluted model obtained in the previous step is used to throw an Asimov dataset which is fitted with a double-sided crystal-ball. This ultimate fitting model represents the final description of the mass resonance for a given mass and width. The closure test fit to the asimov dataset is shown in Figure 38 for $m_X = 750$ GeV narrow width.
- The signal model derived in the previous steps depends continuously upon m_X through the parameters which describes the model itself: mean, σ , $\alpha_{L/R}$, $n_{L/R}$.

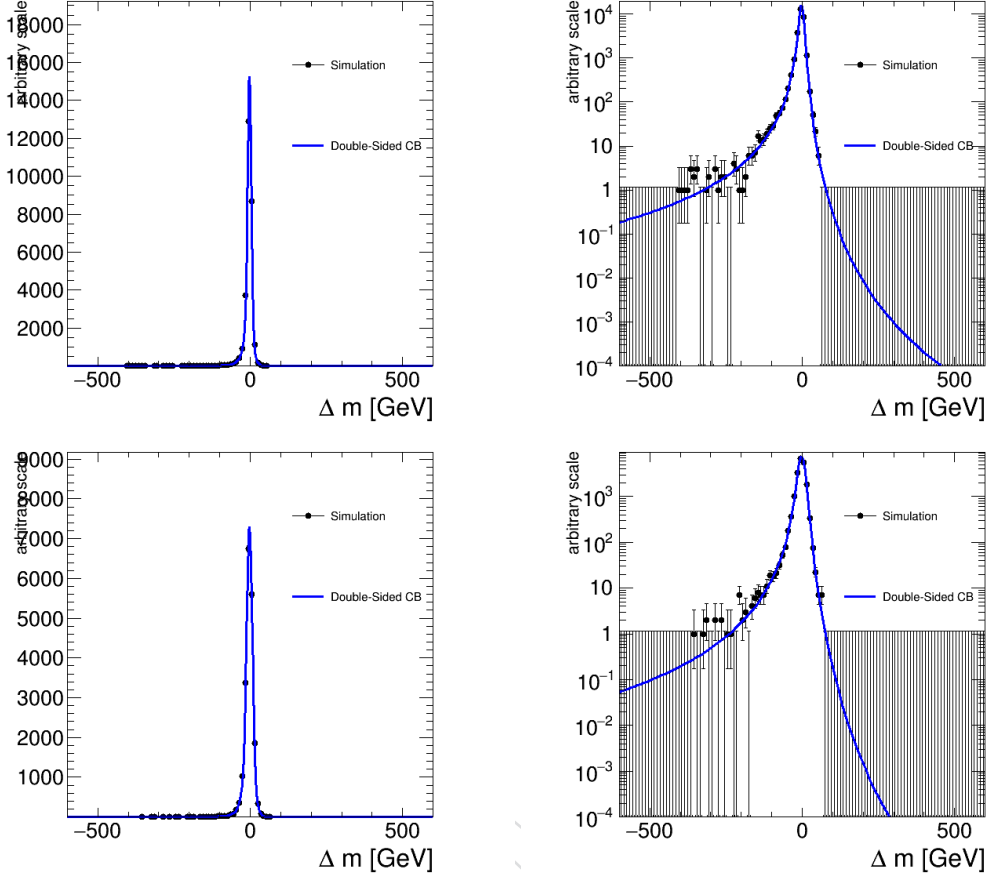


Figure 35: Double-sided Crystal-Ball fit (blue line) to the response distributions for $m_X = 750$ GeV. Linear scale (left) and logarithmic scale (right). Barrel-barrel category on the top and barrel-endcap category on the bottom

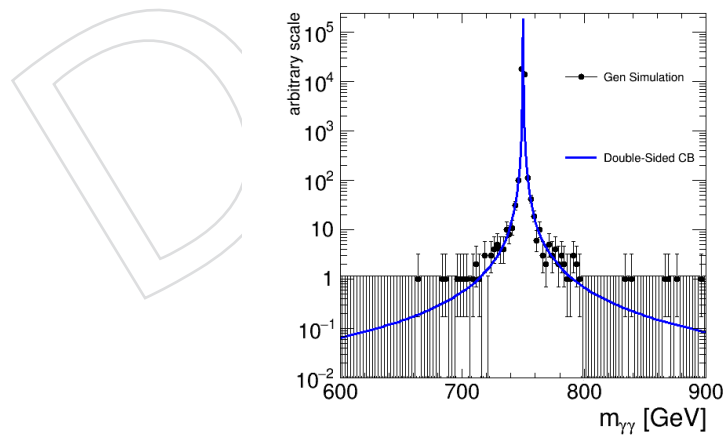


Figure 36: Double-sided Crystal-Ball fit (blue line) to the generator-level distributions for $m_X = 750$ GeV narrow width hypothesis.

For each category and for each width hypothesis the trend of these parameters is studied and modelled with a polynomial function with m_X as the only independent variable.

The parametric signal model obtained is shown in Figures below as a function of m_X

682
683
684

685

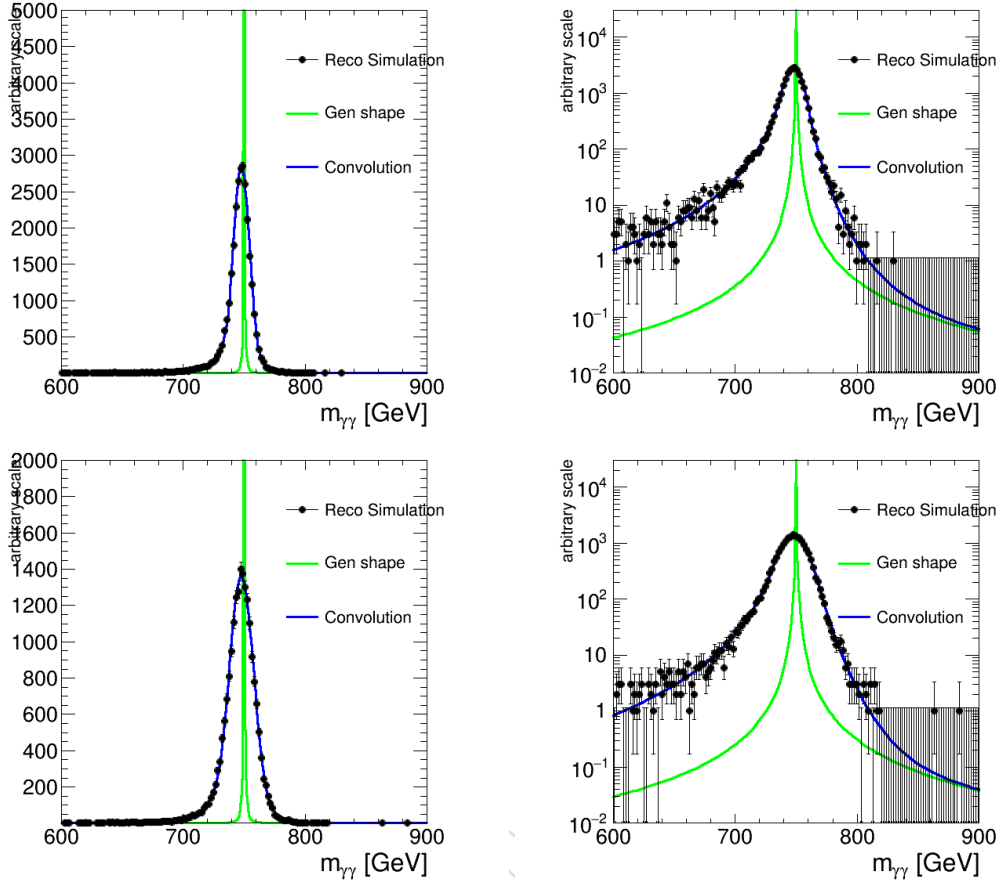


Figure 37: Convolved model (blue line) of the response function and the generator-level function (green line) compared to the reconstructed mass distribution for $m_X = 750$ GeV. Linear scale (left) and logarithmic scale (right). Barrel-barrel category on the top and barrel-endcap category on the bottom.

for the different width hypotheses.

8.1 Parametric Signal Shape comparison 76X/80X

The procedure described in Sec. 8 has been repeated using two different reconstruction conditions corresponding to two CMSSW release: 76X and 80X. We compare the resonance mass shape between the two release in Figure 40 for m_X equal to 750. The agreement is very good and the resolution is comparable with what has been observed in the non-parametric signal models described in Section 9.

8.2 Expected limits comparison with and without the parametric signal model

Expected limits with the available statistic of 7.6 fb^{-1} have been computed as described in Sec. 13 using the new parametric signal model and the non-parametric signal model used at Moriond described in Sec. 9. The comparisons for both spin 0 and spin 2 are shown in this section for three different width hypotheses. The results are compatible within 3.5%.

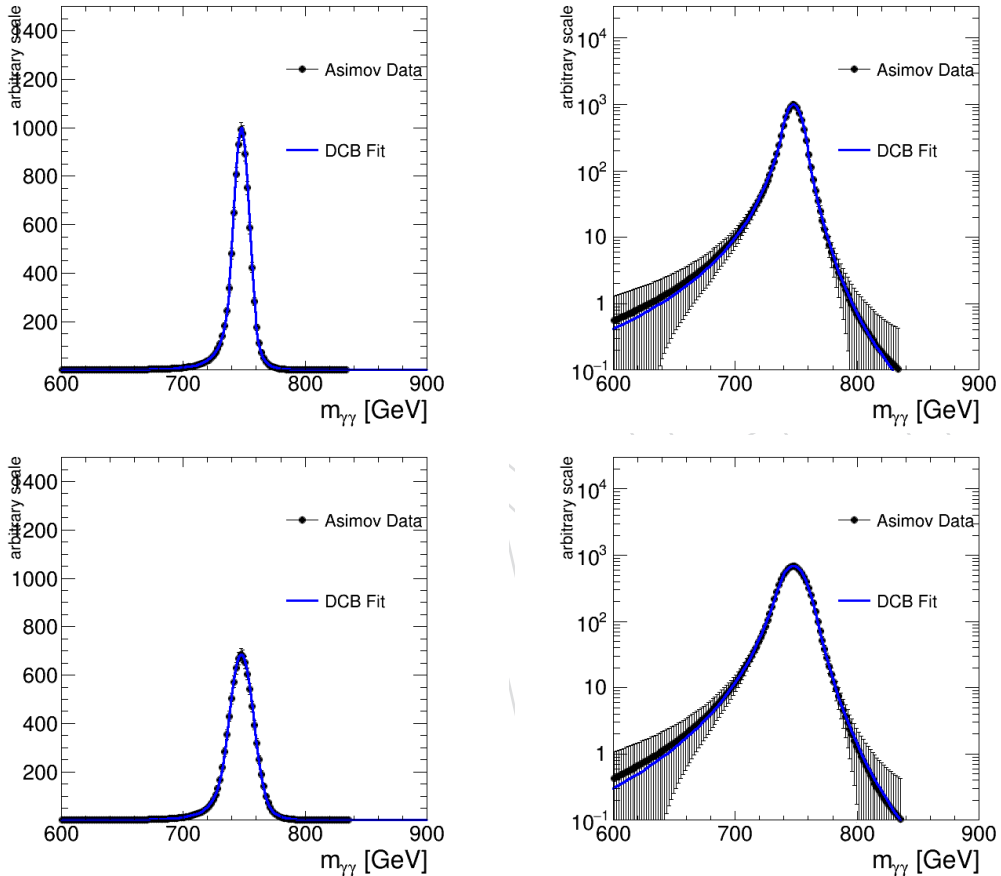


Figure 38: Convoluted model (blue line) of the response function and the generator-level function (green line) compared to the reconstructed mass distribution for $m_X = 750$ GeV. Linear scale (left) and logarithmic scale (right). Barrel-barrel category on the top and barrel-endcap category on the bottom.

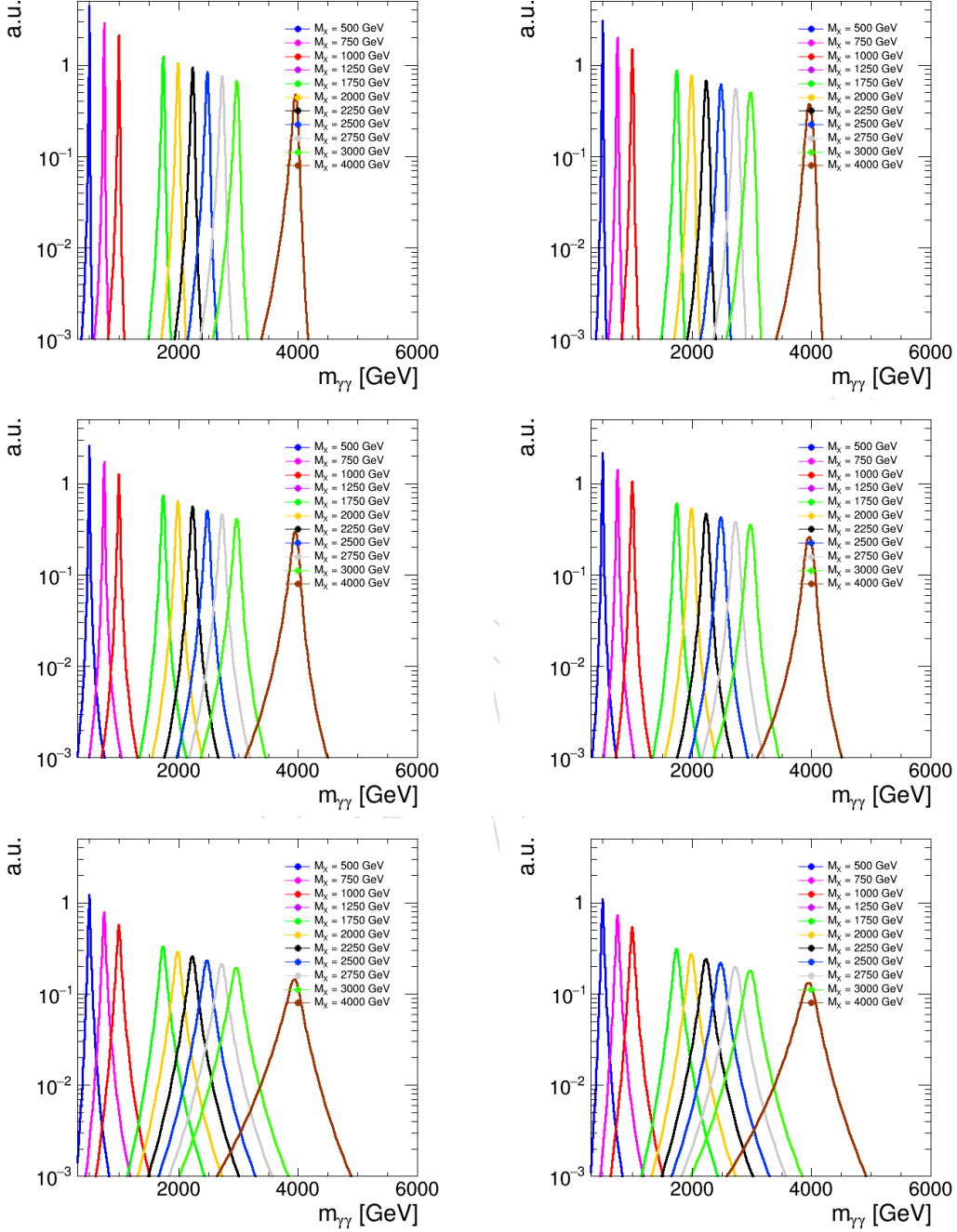


Figure 39: Parametrized signal model as a function of the resonance mass m_X for: $\Gamma/m = 0.14\%$. Left barrel-barrel category, right barrel-endcap category. From top to bottom the width increases as follows: $\Gamma/m = 0.14, 1.4\%, 5.6\%$

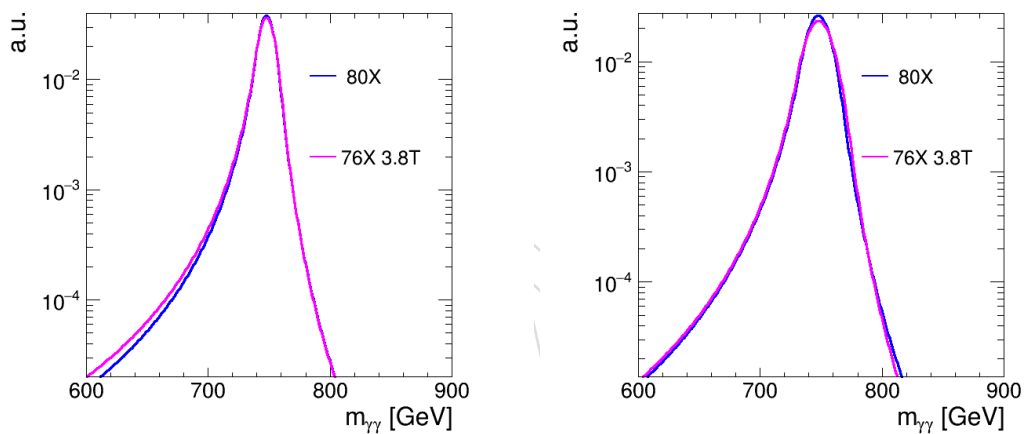


Figure 40: Parametrized signal model comparison between 80X and 76X for $m_X = 750$ GeV narrow width. Linear scale on the left and logarithmic scale on the right. Barrel-barrel category on the top and barrel-endcap category on the bottom.

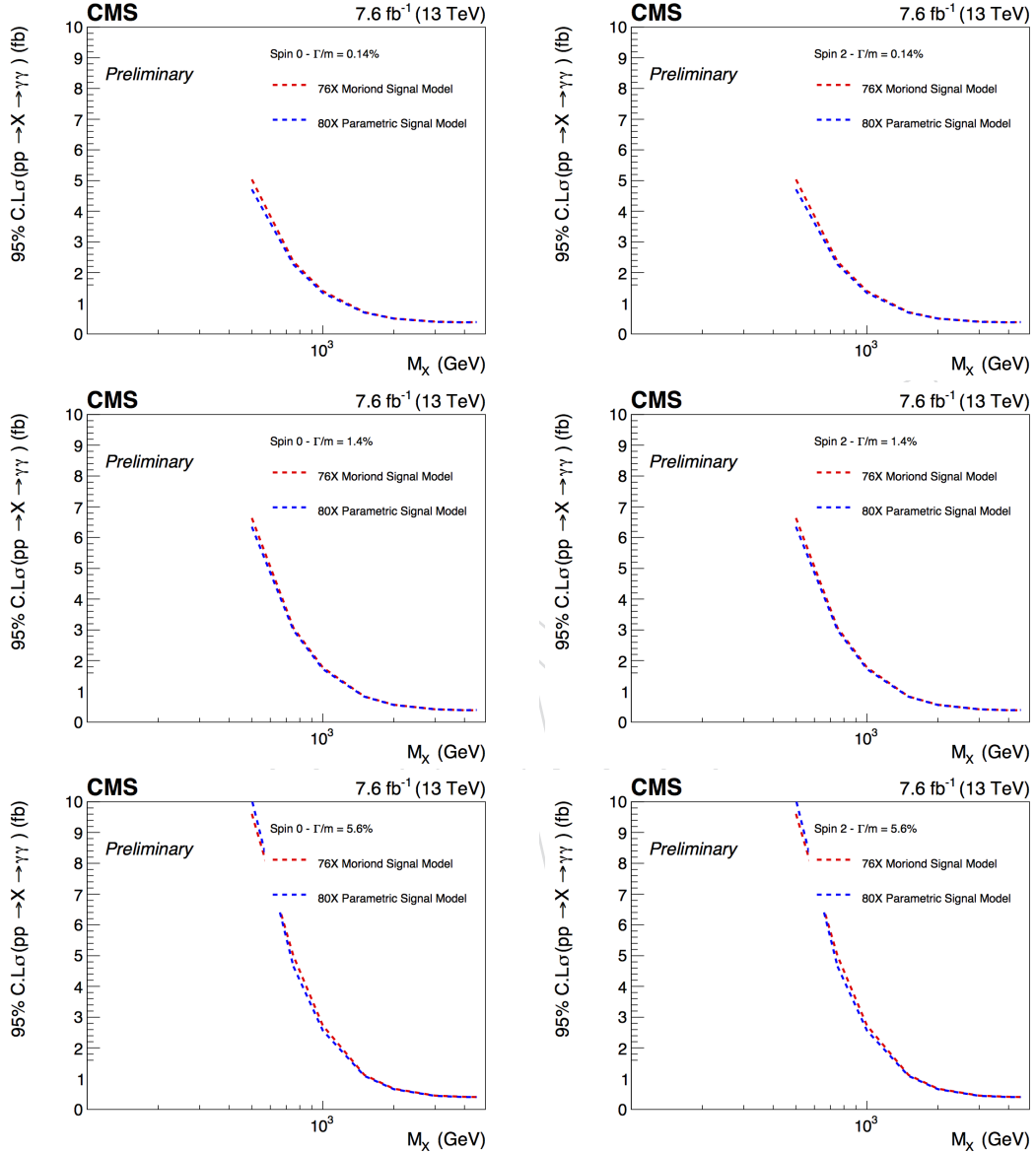


Figure 41: Expected sensitivity obtained with the statistical procedure described in Sec. 13 using the old signal model and the new parametric signal model for the spin 0 hypothesis on the left and spin2 hypothesis on the right. From top to bottom three different resonance widths are investigated.

698 9 Non-parametric Signal Model

699 In this section we describe the method which was originally used in the analysis. It has been
 700 replaced by the method described in Section 8. A description of the original method is given
 701 here for reference, and so that the performance of the new method can be compared with it.

702 As was done in 2015, a binned signal model for all available simulated signal samples. The
 703 full signal model is then defined by an interpolation of each histogram between the fitted mass
 704 values using the morphing technique documented in [20] and implemented in RooFit in the
 705 RooMomentMorph class. The Monte Carlo is used as input to the fits after the smearing of the
 706 resolution. The detector response is modeled using the signal Monte Carlo samples generated
 707 with small intrinsic width. The intrinsic signal line shape is well extracted either from samples
 708 centrally or privately produced at gen-level only. Finally, the generator-level mass histogram
 709 is convoluted with the detector response description to parametrize the reconstructed signal
 710 mass distribution.

711 For the version of the analysis produced so far we used the same signal models used for the
 712 Moriond conference analysis [15]. They are computed with the CMSSW 76X samples, and the
 713 resolution smearings used for Moriond are applied. We don't expect major changes by using
 714 the Spring16 simulated samples. As a first test, we compare in Fig. 42 the $m_{\gamma\gamma}$ distributions
 715 with 76x and 80x samples for the two class categories for two mass points. The agreement
 716 is very good and the resolution is comparable after the different set of smearings is applied.
 717 As a reminder, in Fig. 43 we show the simulation points for $m_X=750\text{ GeV}$ and $k=0.1$ (black
 718 dots) compared with the convolution of the resolution and intrinsic width functions (green
 719 line) obtained on that mass and width for the two event classes, EBEB and EBEE. The plot is
 720 extracted from AN documenting Moriond results, [18].

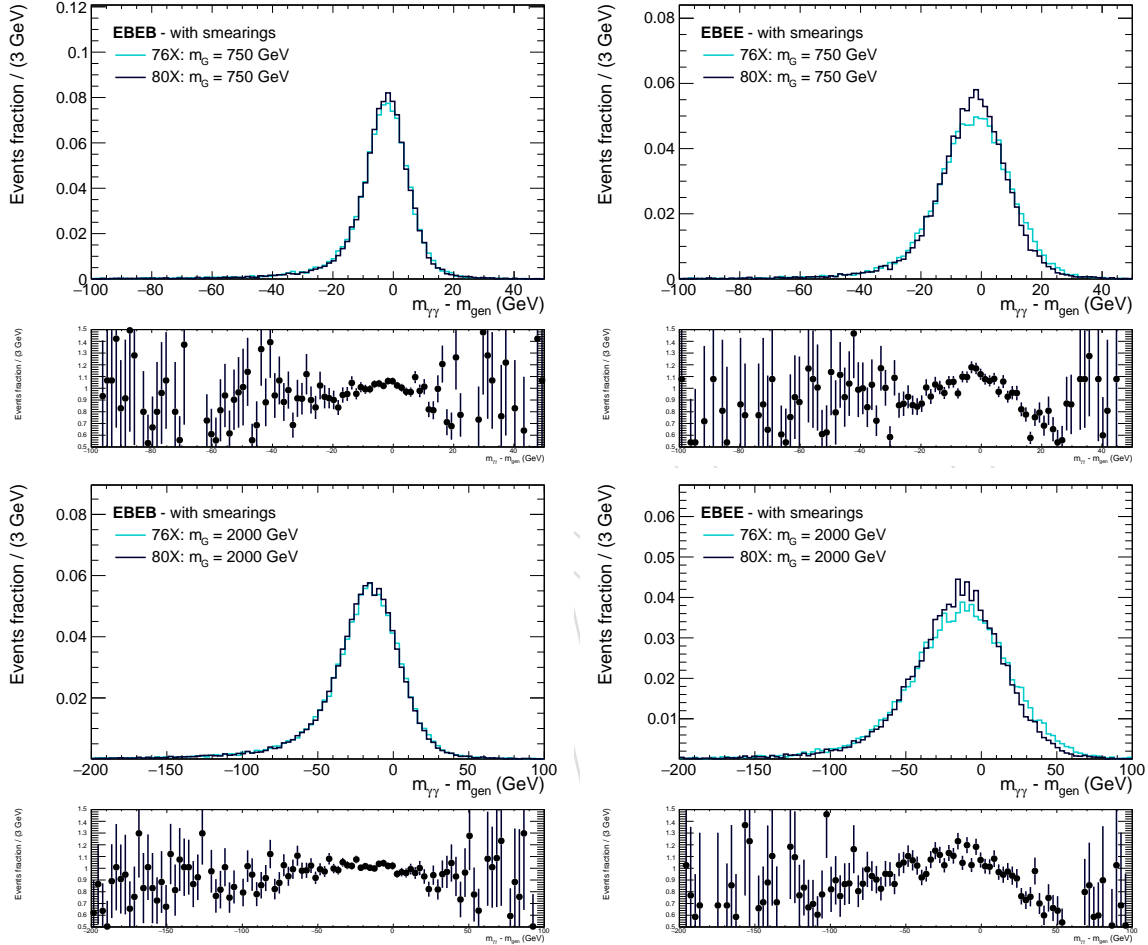


Figure 42: $m_{\gamma\gamma}$ distribution for cmssw-76x (cyan) and 80x (blue) MC signal samples. Signal shape for the signal sample with coupling $k=0.01$ and mass=750 GeV (top) and $m_X=2000$ GeV (bottom) . The two event classes are shown separately, EBEB on the left and EBEE on the right. For the cmssw-76x sample the energy smearings are computed with 2015 data, while for cmssw-80x samples with 2016 data.

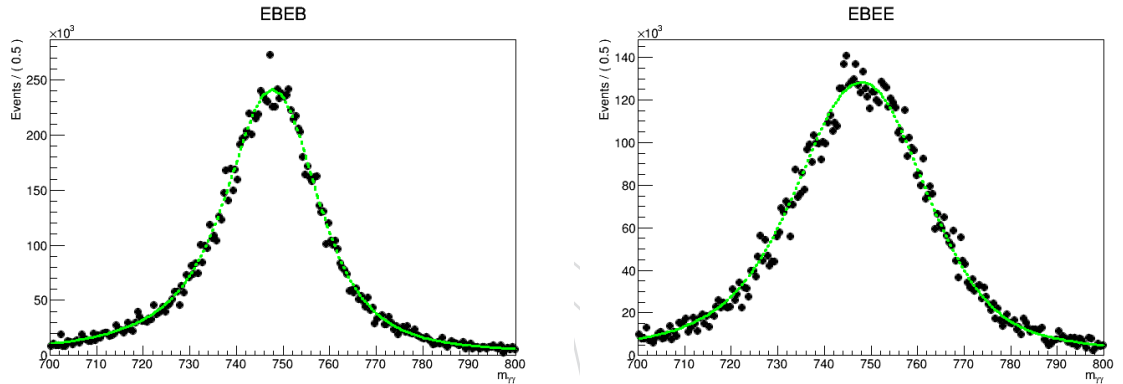


Figure 43: Signal shape for the signal sample with coupling $k=0.1$ and $m_X=750\text{ GeV}$. The black dots are the Monte Carlo events. The green line is the model, given by the convolution of the gen-level mass with the detector resolution. CMSSW-76x samples are used (Moriond signal model, for the moment. Plots extracted from [18]). The two event classes are shown separately, EBEB on the right and EBEE on the left.

721 10 Background model

722 The shape of background in $m_{\gamma\gamma}$ is described as a parametric function of $m_{\gamma\gamma}$. The parametric
 723 coefficients are fit to the data events, allowing to build a data-driven description of the shape.

724 10.1 Background parametrization and bias estimation

725 Choosing an appropriate parametrization of the mass spectrum is important to ensure accuracy
 726 of the prediction, while guaranteeing a good analysis sensitivity.

The background shape is parametrized, for each of the analysis categories, as

$$g(m_{\gamma\gamma}) = m_{\gamma\gamma}^{a+b \log(m_{\gamma\gamma})}$$

727 .

728 The accuracy of the background prediction is evaluated through the following procedure:

- 729 • An ansatz functional form, $g(m_{\gamma\gamma})$, is chosen for the background parametrization.
- 730 • The corresponding true underlying distribution, $h(m_{\gamma\gamma})$ is constructed histogramming the MC events.
- 731 • Unbinned toy experiments t_i , corresponding to number of events which are expected
 732 on data for 10 fb^{-1} are extracted from $h(m_{\gamma\gamma})$.
- 733 • An unbinned maximum likelihood fit is performed to each of the toy experiments,
 734 to obtain $\hat{g}_i(m_{\gamma\gamma})$.
- 735 • The number of events predicted by $\hat{g}_i(m_{\gamma\gamma})$ is compared with $h(m_{\gamma\gamma})$ in several mass
 windows w_j and the pull test statistics is constructed as:

$$p_i^j = \frac{N_{\hat{g}_i}^{w_j} - N_h^{w_j}}{\sigma(N_{\hat{g}_i}^{w_j})}$$

736 where $\sigma(N_{\hat{g}_i}^{w_j})$ accounts for both normalization and shape uncertainties on \hat{g}_i .

A set of intervals in $m_{\gamma\gamma}, w_j$, is chosen as test regions and the parametrization $g(m_{\gamma\gamma})$ is considered accurate if, for all the windows j , the following relation holds:

$$b^j = |\text{median}(p_i^j)| < 0.5 \quad (5)$$

737 Choosing a threshold of 0.5 for b^j is equivalent to allowing the uncertainty on the mean number
 738 of estimated background events to be underestimated by at most 10%.

If the criterion from Eq. 5 is not met for, the pull test statistics is modified as follows:

$$\tilde{p}_j^i = \frac{N_{\hat{g}_i}^{w_j} - N_h^{w_j}}{\sqrt{\sigma^2(N_{\hat{g}_i}^{w_j}) + \beta_I^2(w_j)}} \quad (6)$$

739 Where $\beta_I(w_j) = \int_{w_j} \beta(m_{\gamma\gamma})$ represent an additional uncertainty ("bias term") that is assigned
 740 additionally to the model. The bias criterion can then be modified exchanging p with \tilde{p} .

$$\tilde{b}^j = |\text{median}(\tilde{p}_i^j)| < 0.5 \quad (7)$$

For this study the $\gamma\gamma$ Sherpa sample (see Tab. 3) is used to derive $h(m_{\gamma\gamma})$. The sample is generated in several bins covering the $m_{\gamma\gamma}$ interval $60 < m_{\gamma\gamma} < 13000 \text{ GeV}$. The leading-order cross-section is scaled by 1.4 to take into account higher order corrections. The resulting background model predicted by simulation is shown by the black points in Figure 44. In order to avoid introducing local distortions in the $m_{\gamma\gamma}$ spectrum, the events are not weighted to match the data pile-up distribution.

Several variations of the spectrum are taken into account to construct $h(m_{\gamma\gamma})$, and the study is repeated for each variation:

- the $m_{\gamma\gamma}$ spectrum predicted by the Sherpa MC is used (“default”);
- an $m_{\gamma\gamma}$ -dependent k-factor [17] is applied to take into account higher order corrections up to NNLO (“pNNLO”);
- the contribution from reducible background is taken into account, parametrizing the background composition measured in the 2015 data [18] (“pFakes”);
- an artificial spectrum is generated, inverting the k-factor (“mNNLO”).

All mass spectra are scaled to the number of events expected in data for an integrated luminosity of 10 fb^{-1} .

A fit of the chosen background parametrization, $g(m_{\gamma\gamma}) = m_{\gamma\gamma}^{a+b \log(m_{\gamma\gamma})}$, to the “default” MC spectrum is shown in Fig. 44.

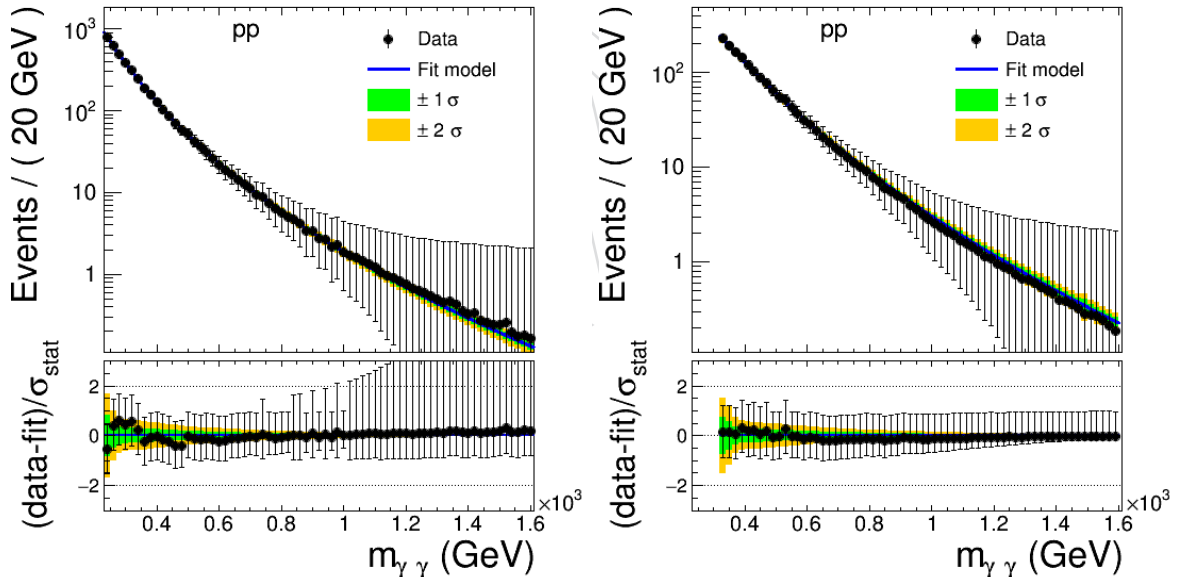


Figure 44: Fit to $\gamma\gamma$ MC spectrum, for the EBEB (left) and for the EBEE category (right) with the background parametrization $g(m_{\gamma\gamma}) = m_{\gamma\gamma}^{a+b \log(m_{\gamma\gamma})}$. The mass window up to 1.6 TeV is shown. The statistical uncertainty is reflecting the expected uncertainty in data for 10 fb^{-1} . The fit uncertainties shown account for shape and normalization uncertainties only and are not used in the bias study.

Three sets of test regions are considered in the study:

- a first set, listed in Tab. 16, is built to have a width of roughly 5% of the $m_{\gamma\gamma}$ value;
- a second set, listed in Tab. 17, is built with a 10% width;

- ⁷⁶² • a third set is built to match the regions used in Ref. [17].

$m_{\gamma\gamma}$ min (GeV)	$m_{\gamma\gamma}$ max (GeV)	$m_{\gamma\gamma}$ min (GeV)	$m_{\gamma\gamma}$ max (GeV)	$m_{\gamma\gamma}$ min (GeV)	$m_{\gamma\gamma}$ max (GeV)
500	525	1040	1090	2160	2270
525	550	1090	1145	2270	2380
550	580	1145	1205	2380	2500
580	610	1205	1265	2500	2625
610	640	1265	1325	2625	2760
640	670	1325	1395	2760	2895
670	705	1395	1465	2895	3040
705	740	1465	1535	3040	3195
740	775	1535	1615	3195	3350
775	815	1615	1695	3350	3520
815	855	1695	1780	3520	3695
855	900	1780	1865	3695	3880
900	945	1865	1960	3880	4000
945	990	1960	2060		
990	1040	2060	2160		

Table 16: List of test regions considered for the bias determination with a bin width of 5%.

$m_{\gamma\gamma}$ min (GeV)	$m_{\gamma\gamma}$ max (GeV)	$m_{\gamma\gamma}$ min (GeV)	$m_{\gamma\gamma}$ max (GeV)
500	550	1425	1570
550	605	1570	1725
605	665	1725	1900
665	730	1900	2090
730	805	2090	2295
805	885	2295	2525
885	975	2525	2780
975	1070	2780	3060
1070	1180	3060	3365
1180	1295	3365	3700
1295	1425	3700	4000

Table 17: List of test regions considered for the bias determination with a bin width of 10%.

$m_{\gamma\gamma}$ min (GeV)	$m_{\gamma\gamma}$ max (GeV)	$m_{\gamma\gamma}$ min (GeV)	$m_{\gamma\gamma}$ max (GeV)
500	550	900	1000
550	600	1000	1200
600	650	1200	1800
650	700	1800	2500
700	750	2500	3500
750	800	3500	4500
800	900	4500	5500

Table 18: List of test regions considered for the bias determination used in Ref. [17].

category	$m_{\gamma\gamma}$ range	$\beta(m_{\gamma\gamma})/L(\text{fb}/\text{GeV})$
EBEB	$> 230 \text{ GeV}$	$0.1 \times m_{\gamma\gamma}^{(2.2-0.4 \times \log(m_{\gamma\gamma}))}$
EBEE	$> 320 \text{ GeV}$	$0.01 \times \left(\frac{m_{\gamma\gamma}}{600 \text{ GeV}}\right)^{-5} + 2 \times 10^{-6}$

Table 19: Bias parametrization, β , divided by the integrated luminosity for the two analysis categories.

The modified bias criterion is met for all $m_{\gamma\gamma}$ spectrum variations and all sets of test region using β as reported in Table 19. The β function in Table 19 is smaller compared to the corresponding one in Ref. [17]. The reason is that in the present study a better estimation of the relative normalization of the different MC $m_{\gamma\gamma}$ bins was used. A mismatch of 5–10% in the relative $m_{\gamma\gamma}$ bins led in fact to an overestimation of b^j in Ref. [17]. The two β functions, normalized to 1 fb^{-1} , are shown in Figure 45.

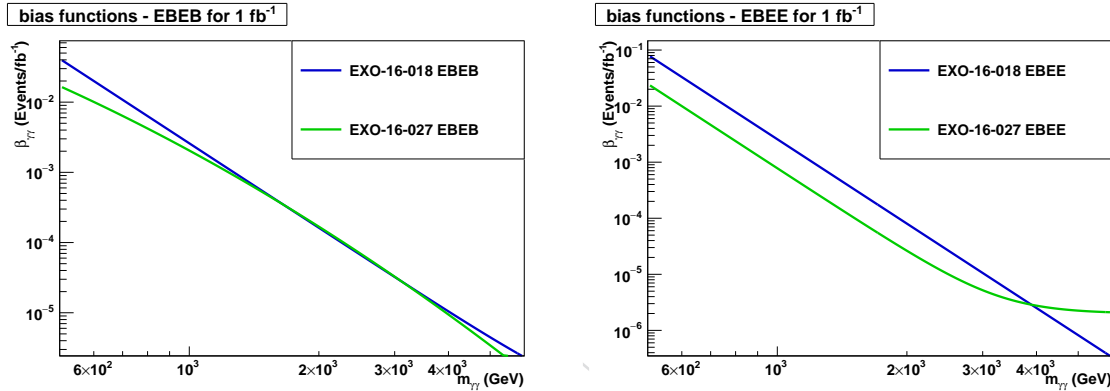


Figure 45: Comparison of the bias parametrization, β , divided by the integrated luminosity, obtained in this study and in Ref. [17]. Left and right plots show the EBEB and EBEE categories respectively.

The b and \tilde{b} values of the default test region of Table 18 can be found in Fig. 50 for the EBEB category and Fig. 51 for the EBEE category, respectively. The results for the set of test regions with a 5% and 10% width are shown in Fig. 46–Fig. 49. The chosen bias term parametrization covers all MC shape variations and different sets of test regions.

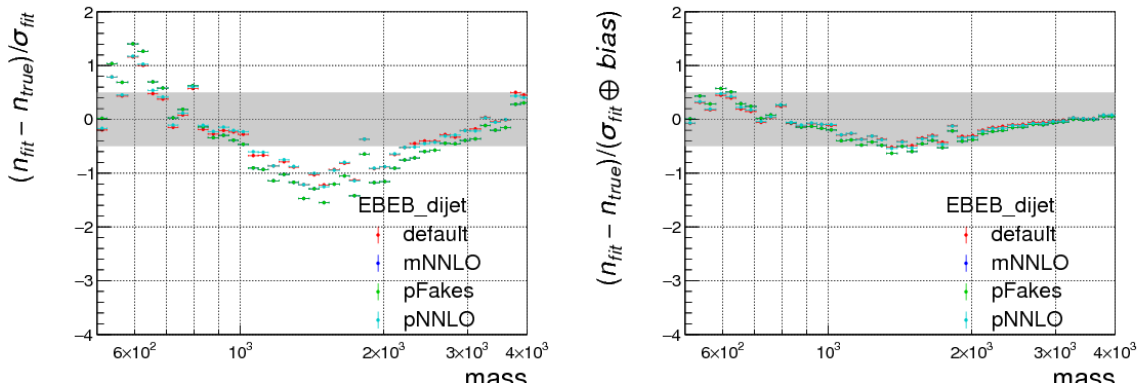


Figure 46: Median of the pull p and modified pull \tilde{p} for all considered test regions according to Tab. 16 for EBEB. Different datasets correspond to different MC shape variations as specified in the text.

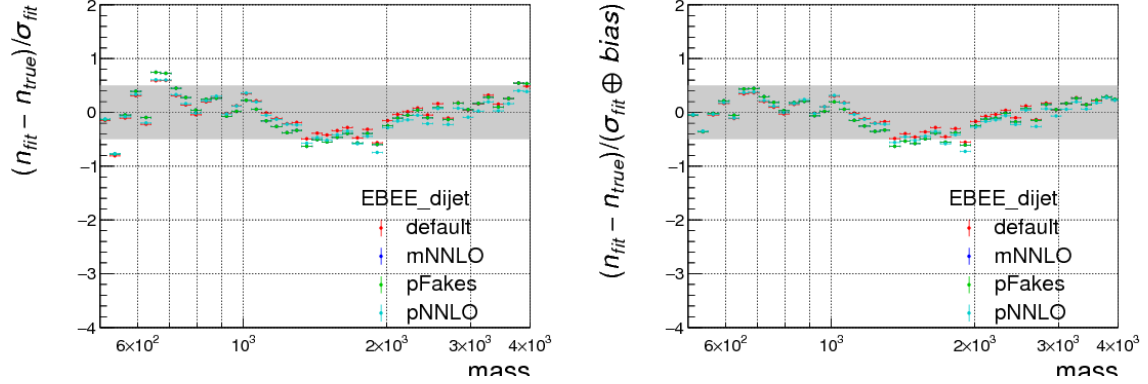


Figure 47: Median of the pull p and modified pull \tilde{p} for all considered test regions according to Tab. 16 for EBEE. Different datasets correspond to different MC shape variations as specified in the text.

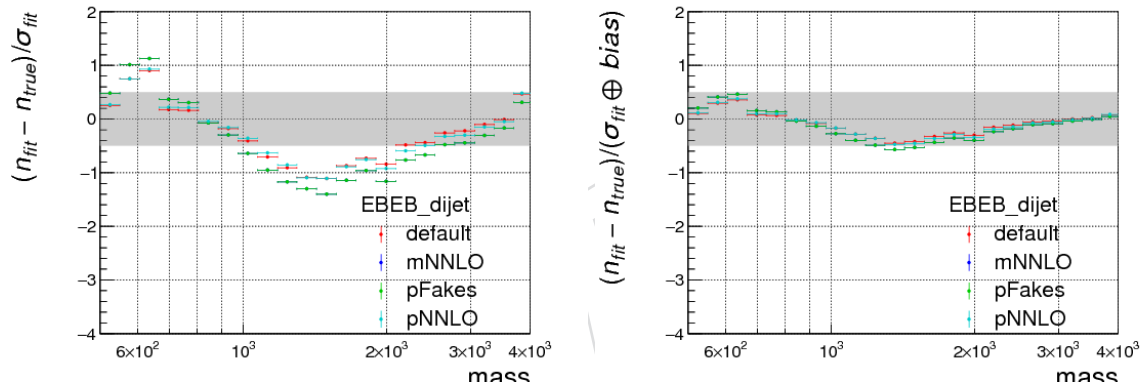


Figure 48: Median of the pull p and modified pull \tilde{p} for all considered test regions according to Tab. 17 for EBEB. Different datasets correspond to different MC shape variations as specified in the text.

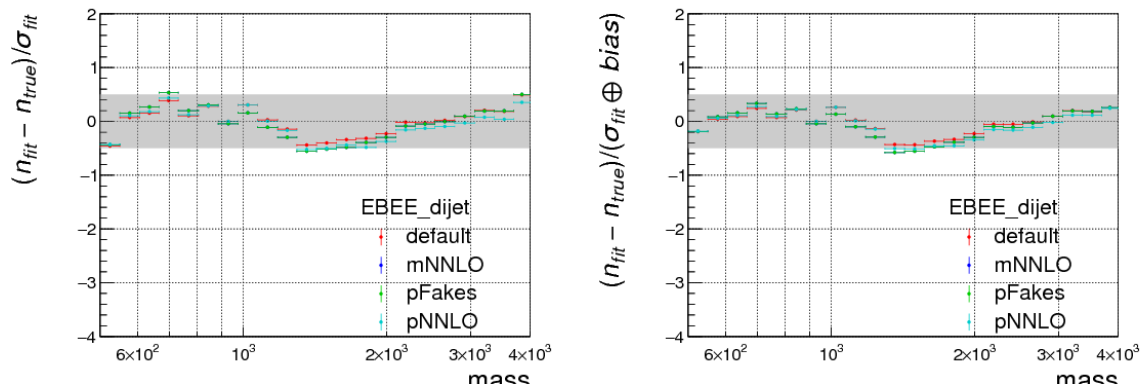


Figure 49: Median of the pull p and modified pull \tilde{p} for all considered test regions according to Tab. 17 for EBEE. Different datasets correspond to different MC shape variations as specified in the text.

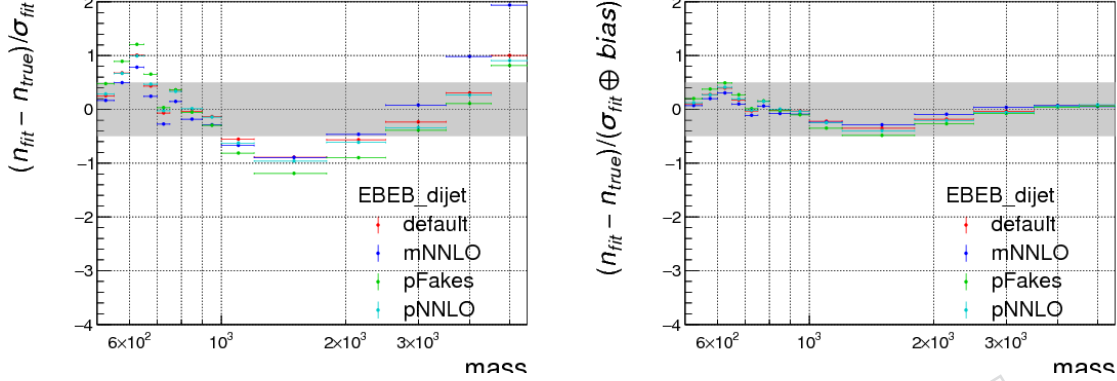


Figure 50: Median of the pull p and modified pull \tilde{p} for all considered test regions according to Tab. 18 for EBEB. Different datasets correspond to different MC shape variations as specified in the text.

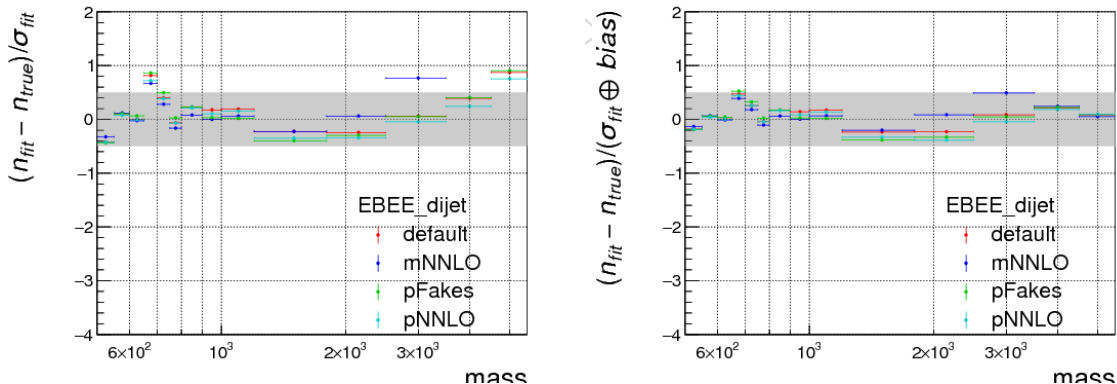


Figure 51: Median of the pull p and modified pull \tilde{p} for all considered test regions according to Tab. 18 for EBEE. Different datasets correspond to different MC shape variations as specified in the text.

773 10.2 Inclusion of bias term in hypothesis testing

774 In order to account for the bias uncertainty in the test statistics used in the hypothesis testing,
 775 the background model is modified to include an additional term which has the same distribution
 776 as the signal that hypothesis being tested.

$$\tilde{g}_{\text{sig}}(m_{\gamma\gamma}|\theta_\beta) \cdot Pdf(\theta_\beta) = \left(\frac{N_{bkg} - \theta_\beta N_\beta(\text{sig})}{N_{bkg}} g(m_{\gamma\gamma}) + \frac{\theta_\beta N_\beta(\text{sig})}{N_{bkg}} s(m_{\gamma\gamma}) \right) \cdot Norm(\theta) \quad (8)$$

777 Where $N_\beta(\text{sig}) = \int \beta(m_{\gamma\gamma}) \cdot s(m_{\gamma\gamma}) \sim \beta(m_G) \cdot FWHM(\text{sig})$, $s(m_{\gamma\gamma})$ is the signal pdf and
 778 $Norm(x)$ is the normal distribution.

The size of the bias term for the widest mass hypotheses tested in the analysis is: Further stud-

signal hypothesis		$N_\beta / (\varepsilon \cdot A \cdot L)$ (pb)		signal hypothesis		$N_\beta / (\varepsilon \cdot A \cdot L)$ (pb)	
m_G (GeV)	Γ/M (%)	EBEB	EBEE	m_G (GeV)	Γ/M (%)	EBEB	EBEE
500	5.6	2.54	6.75	2000	5.6	0.04	0.04
750	5.6	0.94	1.71	3000	5.6	0.01	0.04
1000	5.6	0.43	0.59	4000	5.6	0.004	0.07
1500	5.6	0.12	0.15				

Table 20: Equivalent cross section of the bias uncertainty for the widest signal hypotheses tested in the analysis for $J = 2$.

779
 780 ies, aiming to quantify the accuracy of the background model can be found in the Appendix F.
 781 An alternative parametrization of the background model and an alternative bias parametriza-
 782 tion are studied.

783 10.2.1 Effect of the bias term on the analysis sensitivity

784 In order to evaluate the impact of the background bias term introduced in the previous para-
 785 graphs on the sensitivity of the analysis, we studied the effect of switching on and off the bias
 786 term in Eq. 8.

787 Two metrics were considered: the median expected upper limit on the signal strength for dif-
 788 ferent mass hypotheses, as well as the expected signal strength for a mass of $m_{\gamma\gamma} = 750$ GeV
 789 with a cross section of $\sigma = 7$ fb. Both quantities were computed, using frequentist statistics in
 790 the asymptotic approximation, as detailed in Sec. 13, and assuming an integrated luminosity
 791 of 10 fb^{-1} .

792 The results of the median expected limit are reported in Table 21 and in Table 22 for spin-
 793 0 and spin-2, respectively. A comparison of the median expected limit for the largest width
 794 RS-graviton hypothesis is shown in Figure 52. The expected significance for a mass of $m_{\gamma\gamma} =$
 795 750 GeV is listed in Table. 23. As expected, the mass hypotheses for which the effect is largest are
 796 the widest ones ($\Gamma/M = 5.6\%$) at the low end of the search region ($m_G \sim 500 - 800$ GeV). In this
 797 range, a 5 – 15% worsening of the analysis sensitivity is estimated. The expected significance
 798 for a mass of $m_{\gamma\gamma} = 750$ GeV is reduced by up to 3% for the narrowest and largest signal width
 799 hypothesis. For narrower and heavier mass hypotheses, the size of the effect is smaller. For the
 800 narrow width (largest width) hypothesis the effect is at most 1% for masses above 1 TeV (1.6
 801 TeV).

$m_{\gamma\gamma}$ (GeV)	Γ/M (%)	exp.limit (fb) with bias	exp.limit (fb) without bias	difference (%)
500	0.014	2.61	2.43	7
	5.6	5.37	4.80	12
750	0.014	1.28	1.25	2
	5.6	2.72	2.57	6
1000	0.014	0.82	0.81	1
	5.6	1.58	1.49	6
3000	0.014	0.31	0.31	< 1
	5.6	0.34	0.34	< 1

Table 21: Comparison of the median expected upper limit on the signal strength for the narrow and large width hypotheses for the Spin $J = 0$ hypothesis using the bias parametrization from Tab. 19. An integrated luminosity of 10 fb^{-1} is assumed.

$m_{\gamma\gamma}$ (GeV)	Γ/M (%)	exp.limit (fb) with bias	exp.limit (fb) without bias	difference (%)
500	0.014	3.34	3.06	9
	5.6	6.63	5.88	13
750	0.014	1.58	1.54	3
	5.6	3.25	3.07	6
1000	0.014	0.97	0.96	1
	5.6	1.83	1.75	5
3000	0.014	0.31	0.31	< 1
	5.6	0.35	0.35	< 1

Table 22: Comparison of the median expected upper limit on the signal strength for the narrow and large width hypotheses for the Spin $J = 2$ hypothesis using the bias parametrization from Tab. 19. An integrated luminosity of 10 fb^{-1} is assumed.

Γ/M (%)	J	$Z_0^{\text{exp},\text{bias}}$	$Z_0^{\text{exp},\text{nobias}}$	difference (%)
0.014	0	6.10	6.28	3
0.014	2	5.06	5.19	3
5.6	0	2.91	3.01	3
5.6	2	2.45	2.53	3

Table 23: Comparison of expected significance for a mass of 750 GeV with a cross section of $\sigma = 7 \text{ fb}$ with and without bias parametrization listed in Tab. 19 for both spin hypotheses. An integrated luminosity of 10 fb^{-1} is assumed.

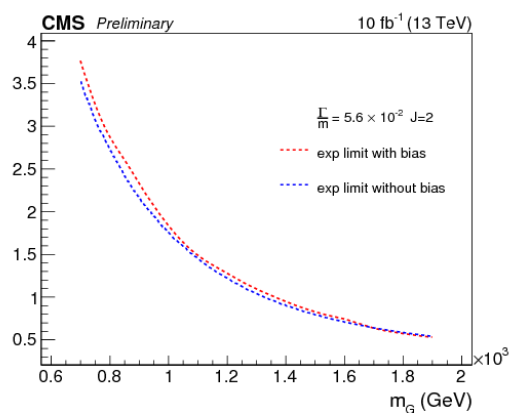


Figure 52: Comparison of the median expected limit for the largest width and spin-2 hypothesis in the mass range of $700 \text{ GeV} < m_{\gamma\gamma} < 2 \text{ TeV}$.

802 11 Systematic uncertainties

803 The impact of the systematic uncertainties is sub-dominant in this analysis.

804 The uncertainties associated to the signal modelling are summarized below. At the moment
805 they all are extracted from the 2015 analysis [18] and will be re-evaluated when needed. All
806 normalization uncertainties are assigned to the overall signal yield (i.e. they refer to pair of
807 photons where applicable).

- 808 • **Luminosity uncertainty:** 2.7% on the signal normalization was assigned to reflect
809 the uncertainty on the knowledge of the total integrated luminosity.
- 810 • **Selection efficiency uncertainties:** a 6% uncertainty on the signal normalization was
811 included to reflect the uncertainty on the knowledge of the data/MC scale factors
- 812 • **Parton distribution functions:** a 6% uncertainty on the signal normalization was
813 assigned in order to account for the variation in the kinematic acceptance of the
814 analysis coming from the use of alternative PDF sets.
- 815 • **Photon energy scale uncertainty:** a 1% energy scale uncertainty was assumed. This
816 number was derived to take into account the knowledge of the energy scale uncer-
817 tainty at the Z peak as well as the knowledge on the extrapolation to high mass,
818 following the studies presented in section 5.
- 819 • **Photon resolution uncertainty** The uncertainty on the extra smearing on the photon
820 uncertainty was evaluated summing and subtracting be 0.5% in quadrature from
821 the estimated constant term measured at the Z peak. The 0.5% value was chosen
822 to match the statistical uncertainty on the extra smearing term measured with the
823 non-resonant Drell-Yan production.

824 The parametric background model has no associated systematic uncertainties, except for the
825 bias term uncertainty described above. The shape coefficients were treated as unconstrained
826 nuisance parameters and contribute to the statistical uncertainties.

827 12 Alternative Analysis

828 An alternative analysis has been performed that uses a completely independent data analy-
 829 sis framework. The common starting point of both the alternative and the standard analysis
 830 is the MiniAOD data tier. The event selection, object reconstruction, and photon energy cor-
 831 rections used is identical to the standard analysis, and has been carefully synchronized and
 832 cross-checked starting with the 2015 version of the analyses, with a more detailed description
 833 for the 2015 analysis and results available in [21], including a near-perfect agreement in selected
 834 events and diphoton mass values, and excellent agreement, with 4% in the relevant parameters
 835 for signal and background models, and expected and observed limits and significances.

836 For the 2016 dataset comprising 4.0 fb^{-1} , there are 3154 events selected by the alternative anal-
 837 ysis, compared to 3152 for the standard analysis, of which 3151 events are in common. The
 838 remaining handful of events not in common are attributed to differences related to numerical
 839 precision near the boundaries of various cut values. For the 3151 events in common, the dipho-
 840 ton mass values are compared, and are in agreement at the level of 10^{-6} , with differences in
 841 the core of the distribution consistent with numerical precision. There are a small number of
 842 outliers, with 20 events with a relative difference of more than 1%. These events are mainly
 843 cases where a different primary vertex is selected, and these remaining differences affecting a
 844 very small fraction of events are attributed to a combination of numerical precision or small re-
 845 maining differences in the MVA primary vertex selection. The distribution for the relative mass
 846 difference for the common events between the alternative and standard analyses is shown in
 847 Figure 53.

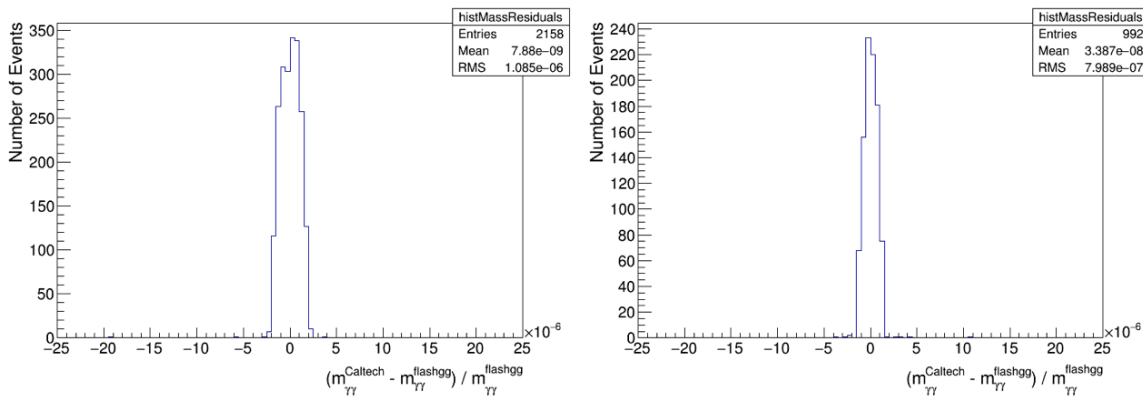


Figure 53: The distribution of the residuals between the diphoton mass obtained from the alternative analysis compared to the standard analysis in the EBEB category (left) and the EBEE category (right). (These plots were produced before the inclusion of the HLT_ECALHT800 trigger and therefore include one fewer event than what has been included in the final analysis.)

848 The di-photon mass distributions are compared between the cross-check and standard analyses
 849 in Figure 54, with differences consistent with the level of synchronization in the selected events
 850 and mass values.

851 Still to be updated

852 Expected limits on the 2.6 fb^{-1} 2016 dataset have been compared and found to agree within
 853 3% between the alternative and standard analyses, under common approximations involving
 854 the use of the 2015 signal model and acceptance/efficiency, and neglecting reconstruction scale

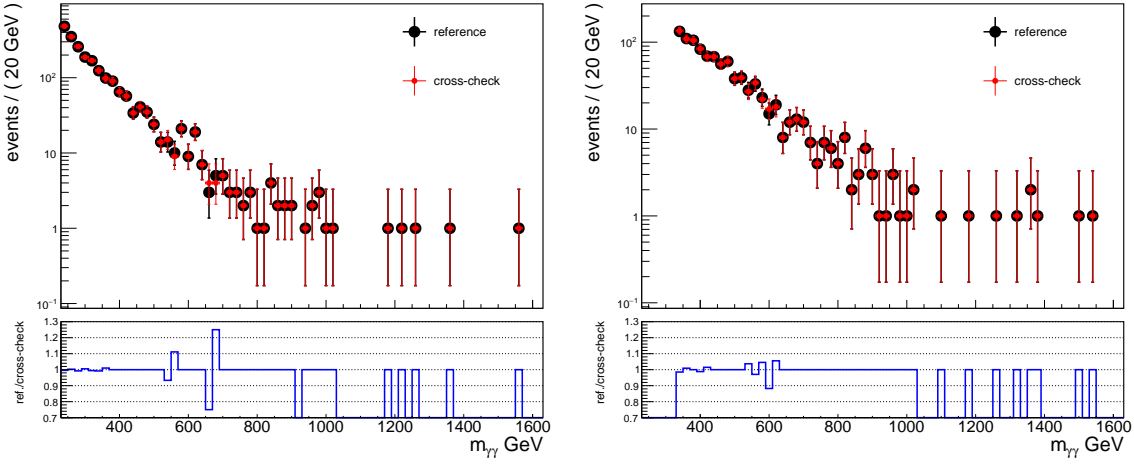


Figure 54: The overlaid diphoton mass distributions obtained from the alternative analysis compared to the standard analysis in the EBEB category (left) and the EBEE category (right).

855 factors for the 2016 dataset, implying an approximation at the level of several percent. The
 856 expected and observed exclusions limits for a narrow spin-0 signal is shown in Figure 55, and
 857 the observed significance in Figure 56.

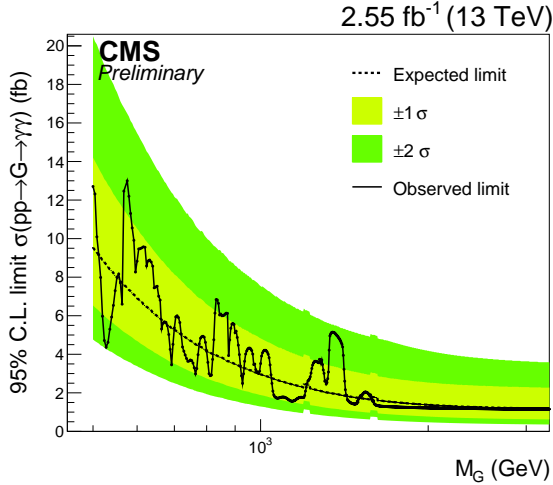


Figure 55: The expected and observed 95% exclusion limits for a narrow spin-0 signal hypothesis in the alternative analysis.

858 The exclusion limits and significance for the 2.6 fb^{-1} dataset are directly compared to those for
 859 the standard analysis in Figure 57.

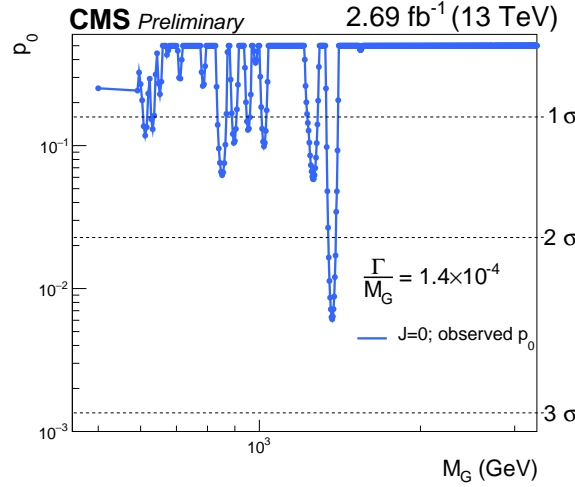


Figure 56: The expected and observed 95% exclusion limits for a narrow spin-0 signal hypothesis in the alternative analysis.

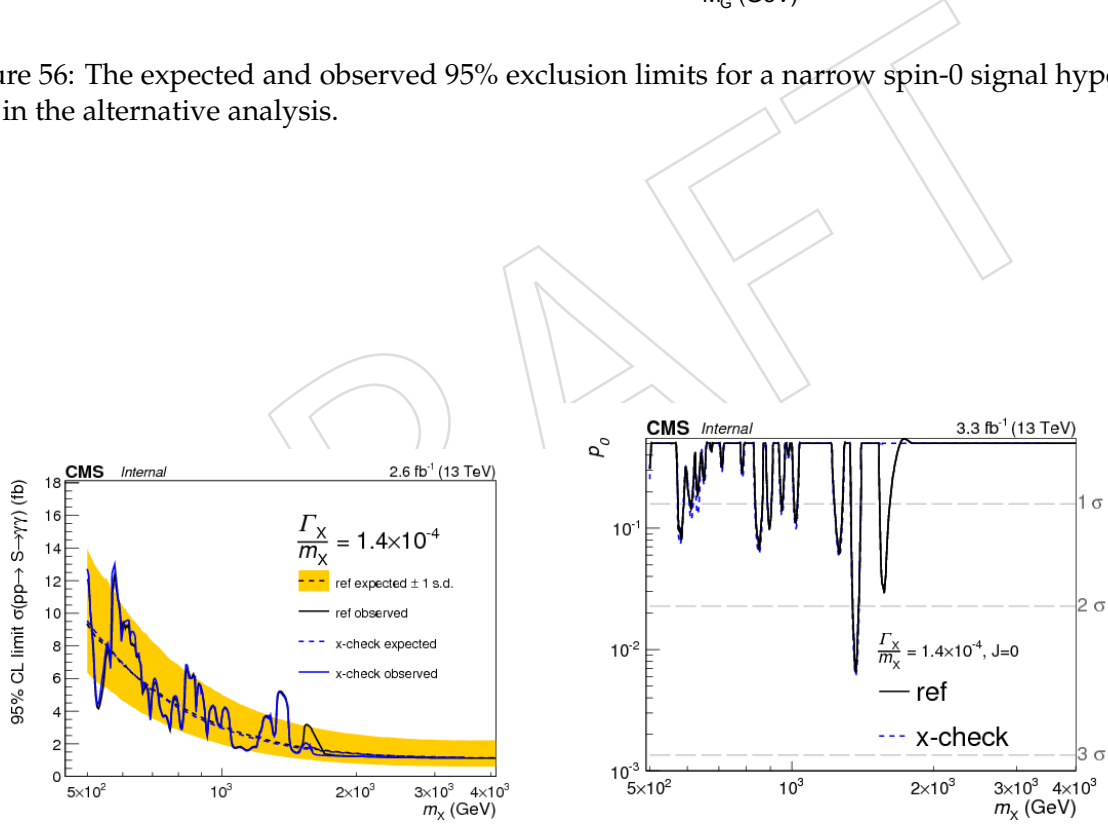


Figure 57: The expected and observed 95% exclusion limits for a narrow spin-0 signal hypothesis in the alternative analysis overlaid with those from the standard analysis (left) and for the observed significance (right). In this iteration of the analysis, the alternative analysis was not yet including the HLT_ECALHT800 trigger, leading to one fewer event selected with a mass around 1.4 TeV, and therefore a corresponding difference in the limits and significance in this region.

860 13 Results

861 This section presents results on the analysis sensitivity. Frequentist statistics is used, according
 862 to the prescriptions in [22], in conjunction with the use of asymptotic formulas [23].

863 Results are presented for the resonant search, assuming two kind of signals:

- 864 • RS gravitons.
- 865 • spin-0 resonances produced in gluon-fusion.

866 For each of the hypotheses, three kind of width scenarios are considered Γ/M : 0.014%, 1.4%
 867 and 5.6%. In the case of the RS graviton resonances, the width is parametrized as $\Gamma/M = 1.4k^2$
 868 and thus $k=0.01, 0.1, 0.2$.

869 For what is shown below, a simultaneous fit to the range $230(320) \text{ GeV} < m_{\gamma\gamma} < 6 \text{ TeV}$ in the
 870 EBEB (EBEE) event categories is used.

871 To set upper limits on the signal strength, the modified frequentist method, commonly known
 872 as CL_s is used, while the presence of a possible signal is quantified in terms of a *background-only*
 873 *p-value*.

874 The test statistics used to derived exclusion limits on the alternative hypothesis or the null one
 875 are based on the profile likelihood ratio:

$$q(\mu) = -\log \lambda(\mu) := -\log \frac{L(\mu \cdot S + B | \hat{\theta}_\mu)}{L(\hat{\mu} \cdot S + B | \hat{\theta})}$$

876 Where S and B are the pdf's for the graviton and SM processes respectively, μ is the so-called
 877 "signal strength" parameter and $\hat{\theta}$ are the nuisance parameters of the model. The $\hat{\cdot}$ notation
 878 indicate best-fit value of the parameters.

879 In many cases, asymptotic formulas [23] are used to compute the analysis sensitivity. The validity
 880 of these formulas in the statistical regime of this analysis have been verified, as documented
 881 in [24].

882 The total selection efficiency of analysis categories for different signal hypotheses are reported
 883 in Fig. 58.

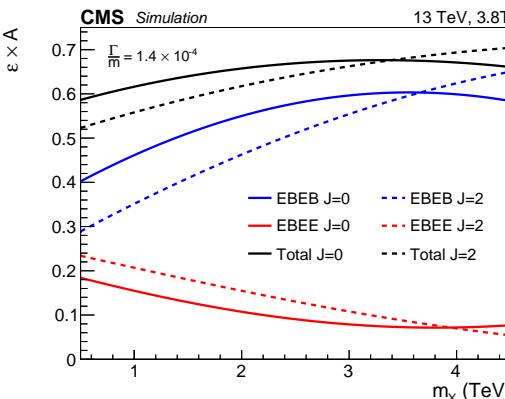


Figure 58: Total analysis selection efficiency.

884 The median expected and the observed exclusion limits for different signal hypotheses are
 885 shown in Fig. 59 for RS graviton and gluon-fusion-produced spin-0 resonances of different

886 widths.

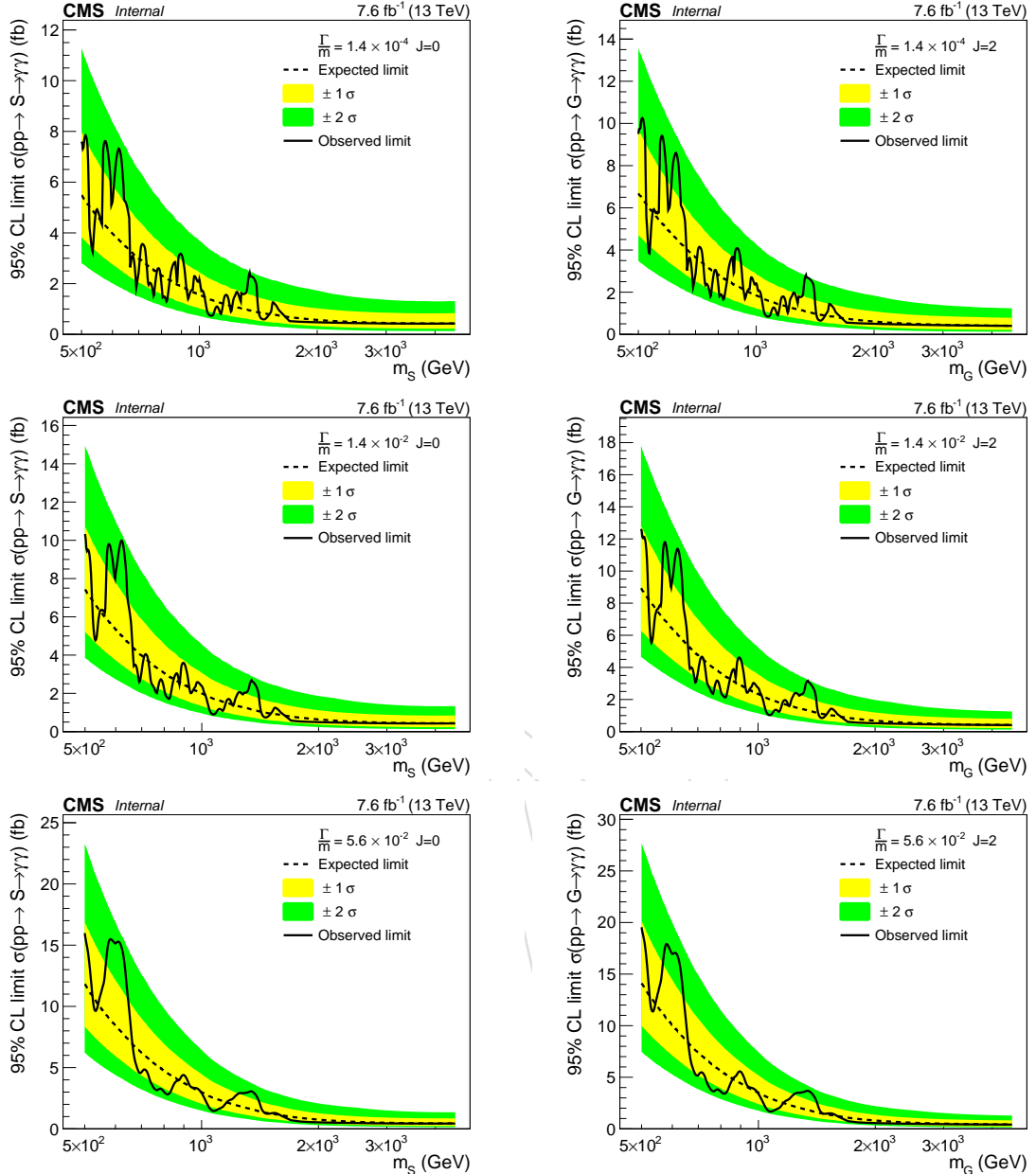


Figure 59: Expected and observed upper limit for RS graviton (left) and gluon-fusion-produced spin-0 (right) resonances of different widths.

887 The compatibility of the data with the background-only hypothesis was evaluated computing
 888 the background-only p-value p_0 , i.e. the probability to obtain a $q(0)$ above the observed one in
 889 the background-only hypothesis. Asymptotic formulas were used here. The results are shown
 890 in Fig. 60. As it can be seen, no excess is observed in the region around 750 GeV in this dataset.

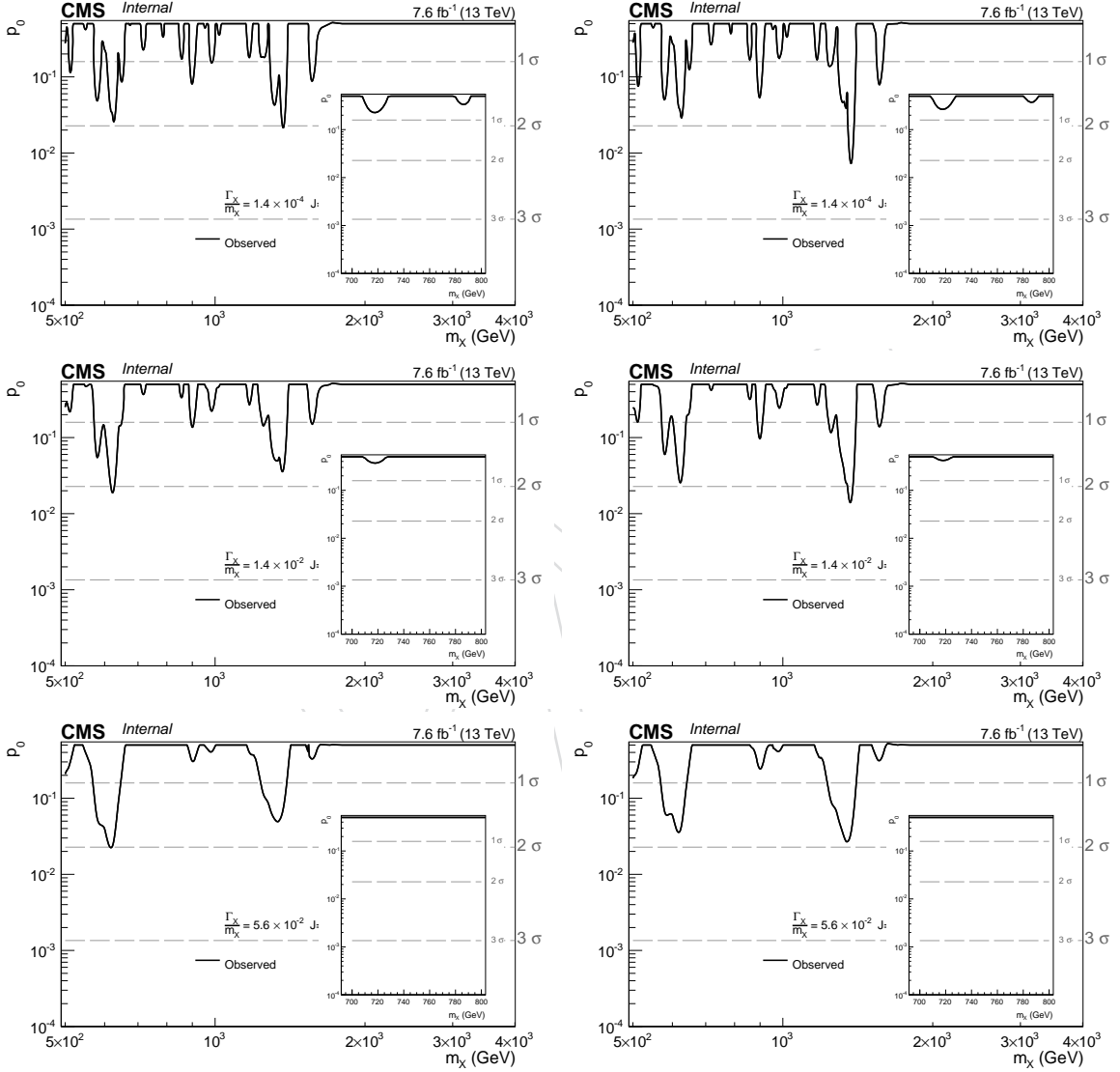


Figure 60: Observed p_0 as a function of the resonance mass for RS graviton (left) and gluon-fusion-produced spin-0 (right) resonances of different widths.

891 14 Conclusions

- 892 We reported on the update on the search for high mass diphoton resonances at $\sqrt{s} = 13$ TeV
893 using 2016 data. The analysis employs 7.6 fb^{-1} of pp collision collected by CMS.
- 894 The analysis strategy is unchanged compared to the analysis of 2015 data. The selection and
895 photon identification criteria were reviewed to check if the 2016 data taking conditions would
896 require a tuning of the event selection. No update was found to be necessary.
- 897 New energy scale and resolution corrections were derived on the 2016 dataset. The resolution
898 corrections were found to be similar with those measured in the 2015 data.
- 899 Overall, the observed data are consistent with the expectations from the SM.

A large, faint watermark-style text "DRAFT" is positioned in the lower-left quadrant of the page. The text is oriented diagonally, sloping upwards from the bottom-left towards the top-right. It is rendered in a light gray color that is semi-transparent, allowing the underlying text content to be visible.

900 A Combination with previous results

901 In this appendix we describe the statistical combination of the results obtained on this dataset
 902 with those of Refs [18, 25]. Three search results are combined.

- 903 • those obtained on 4 fb^{-1} at $\sqrt{s} = 13 \text{ TeV}$ in 2016;
- 904 • those obtained on 3.3 fb^{-1} at $\sqrt{s} = 13 \text{ TeV}$ in 2015;
- 905 • those obtained on 19.7 fb^{-1} at $\sqrt{s} = 8 \text{ TeV}$.

906 In order to combine the 2015 and 2016 results, the same background coefficients are used for
 907 the 2015 3.8T data and the 2016 data. The normalisation coefficients are assumed to be inde-
 908 pendent, while the bias uncertainty is taken to be fully correlated. The background shapes
 909 obtained with independent fits to the two datasets is shown in Fig. 61. Fully correlated signal
 910 uncertainties were taken.

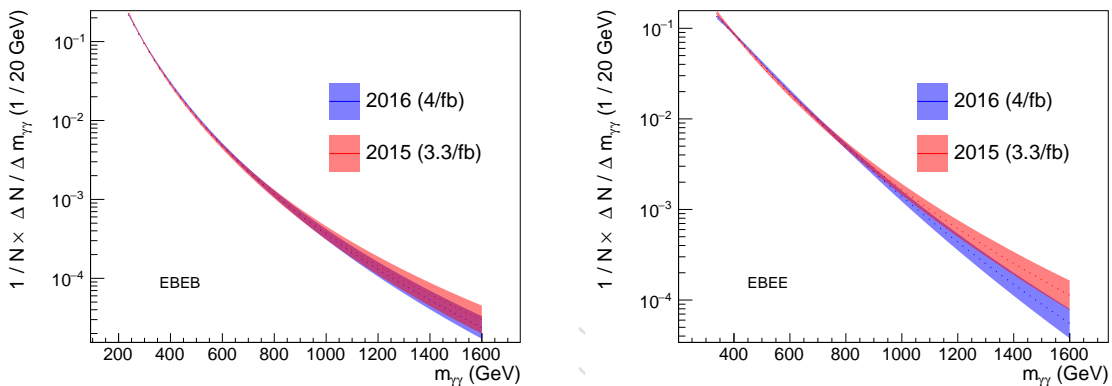


Figure 61: Background shapes obtained using independent fits to the 2015 3.8T data and the 2016 data. The EBEB and EBEE categories are shown on the left and the right respectively.

911 Figure 62 shows the combined p_0 obtained using the 2015 and 2016 datasets. As it can be seen
 912 from the plot, the 2.9 standard deviation excess observed in the 2015 dataset around 750 GeV
 913 under the narrow signal hypotheses is reduced to less than 1.5 standard deviation when the
 914 two datasets are combined.

915 The compatibility of the two results is estimated to be at the 2.2 standard-deviations level by
 916 studying the compatibility of the difference in signal strengths with 0. The corresponding like-
 917 lihood scan is shown in Fig. 63 for the narrow spin-0 hypothesis.

918 The 13 TeV results are further combined with those obtained at 8 TeV following the procedure
 919 described in [25]. The combined p_0 is shown in Fig. 64.

920 The compatibility of the three results is estimated to be at 1.8 standard-deviations level by
 921 studying the compatibility of the three datasets with a common signal strength. The corre-
 922 sponding likelihood scan as function of the equivalent 13 TeV cross-section is show in Fig 65,
 923 for each of the three datasets and for the combination.

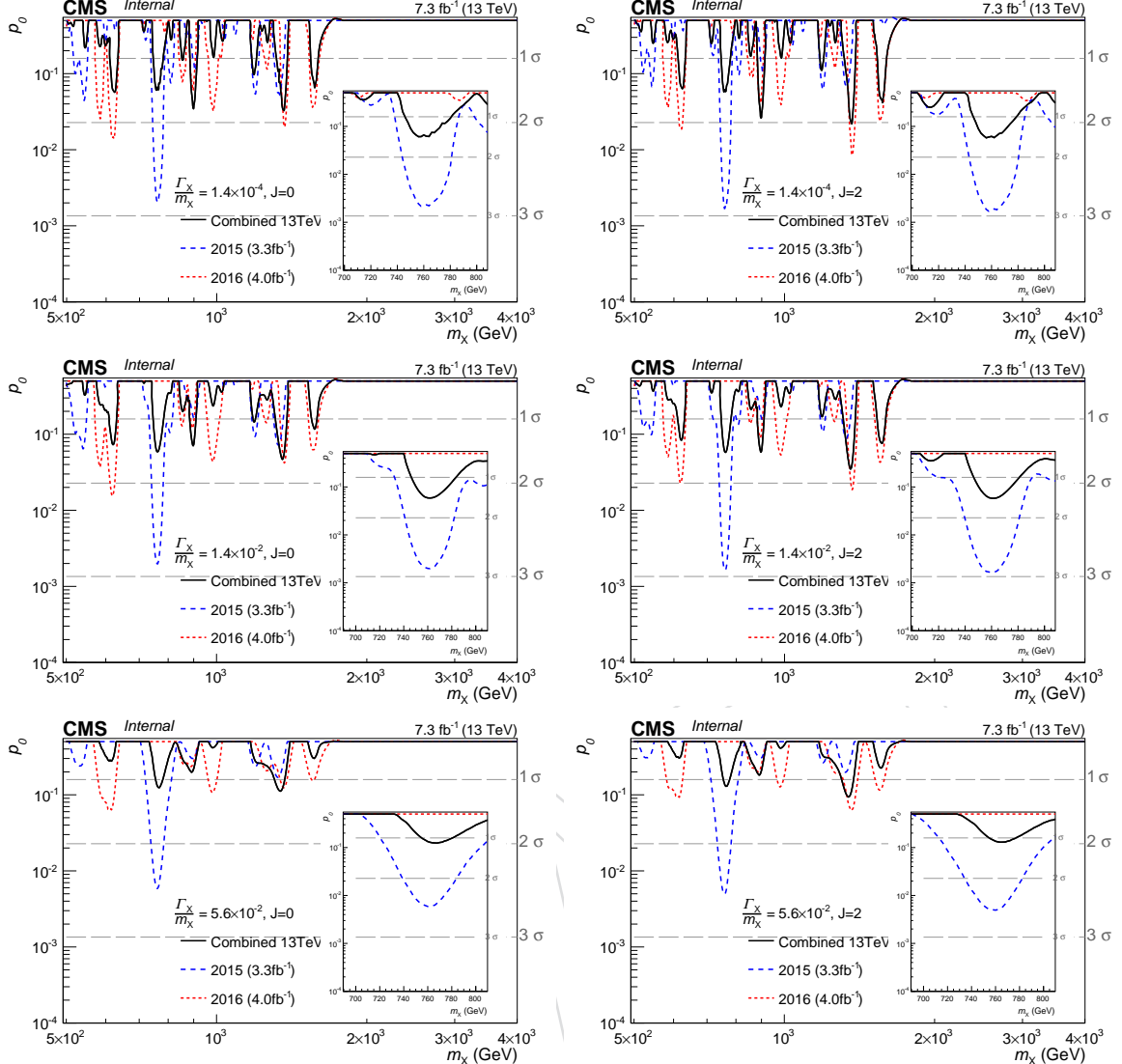


Figure 62: Observed p_0 as a function of the resonance mass obtained from the combination of the 2015 and 2016 results. RS graviton and gluon-fusion-produced spin-0 resonances of different widths are shown on the left and right columns respectively.

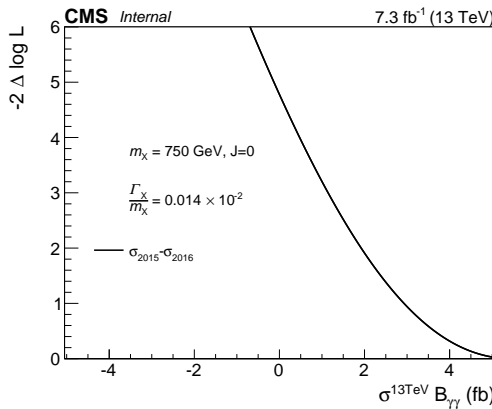


Figure 63: Likelihood scan of the difference between the 2015 and 2016 signal strength for a narrow spin-0 resonance with a mass of 750 GeV.

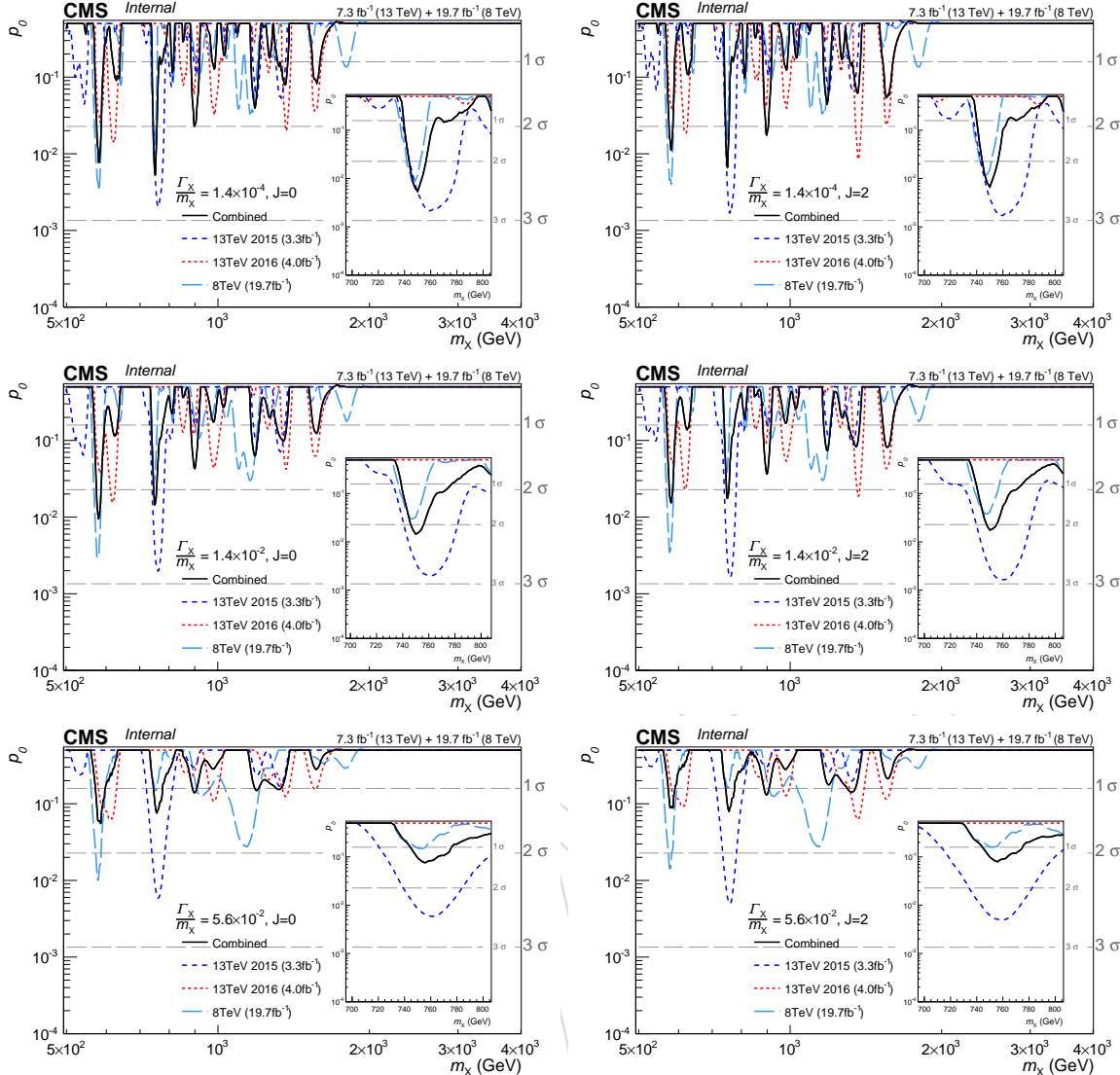


Figure 64: Observed p_0 as a function of the resonance mass obtained from the combination of the 8 and 13 TeV results. RS graviton and gluon-fusion-produced spin-0 resonances of different widths are shown on the left and right columns respectively.

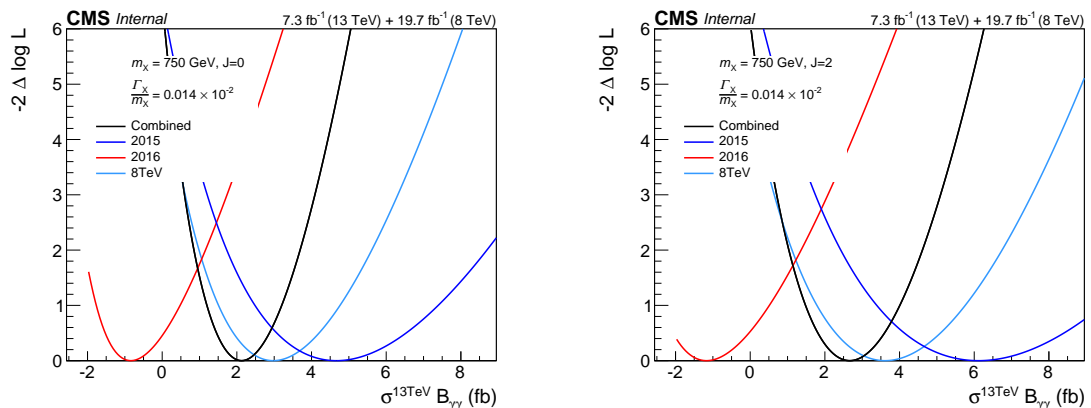


Figure 65: Likelihood scan of the difference between the 2015 and 2016 signal strength for a narrow spin-0 resonance with a mass of 750 GeV.

924 **B Control plots for luminosity top-up to 7.6 fb^{-1}**

925 In this appendix we show control plots for top-up of the analysis dataset to 7.6 fb^{-1} . Compared
 926 to the main body of the analysis note, the luminosity calibration was updated to follow the
 927 latest calibration. The integrated luminosity estimated for the dataset analyzed in the main
 928 body of the note changed to 4.3 fb^{-1} . Therefore, 3.3 fb^{-1} were added to the analysis.

929 Energy scale corrections where derived for new dataset using the same procedure described in
 930 Sec.5. The stability of the scale correction is shown in Fig. 66. The resolution corrections where
 931 found to be unchanged compared to Tab. 10.

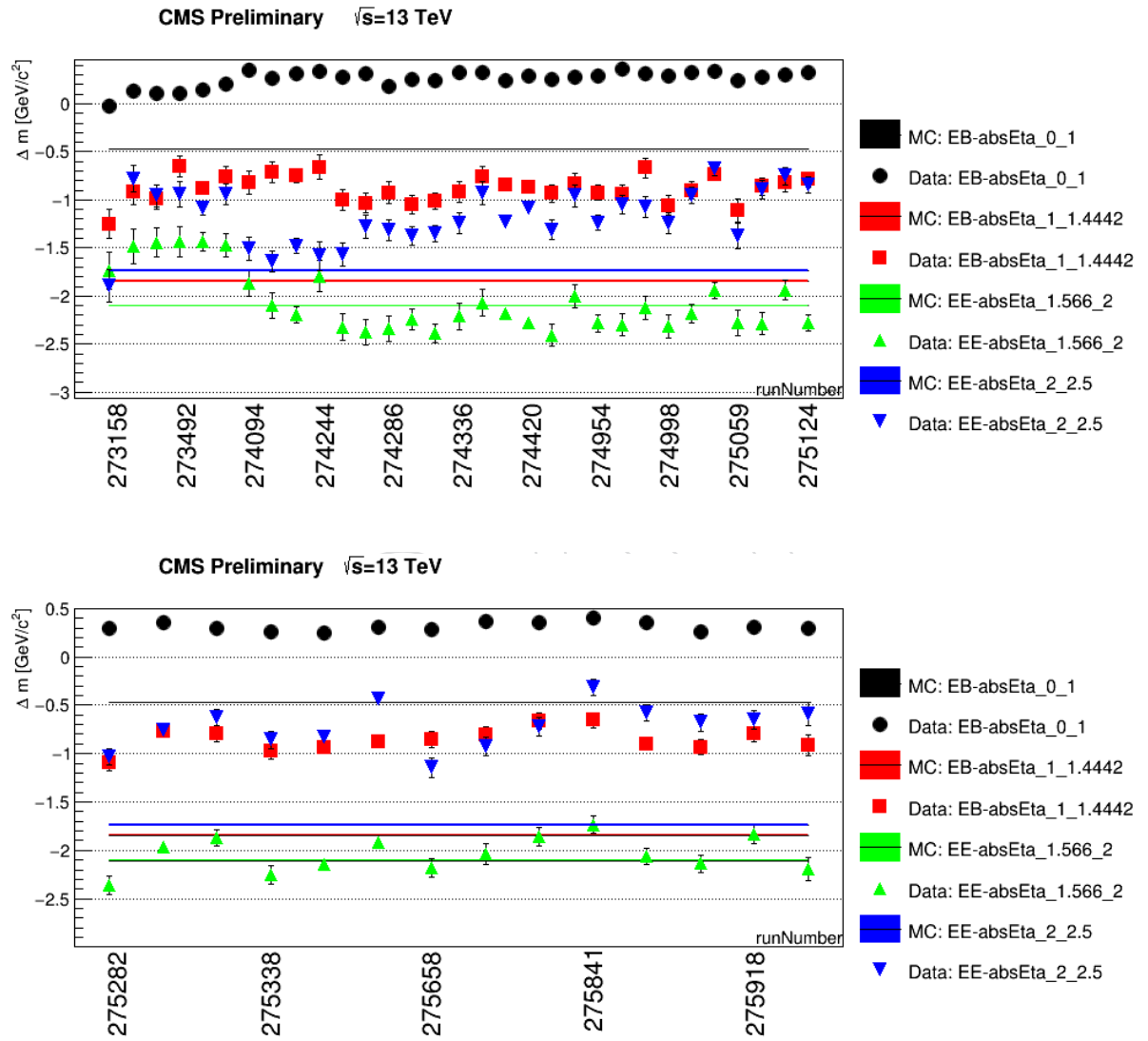


Figure 66: $Z \rightarrow e^+e^-$ lineshape peak values in several run ranges for 4 η categories: 2 categories in EB, 2 categories in EE. MC value is displayed as a continuous line. The top and bottom plots refer to the first 4.3 fb^{-1} and the second 3.3 fb^{-1} data respectively.

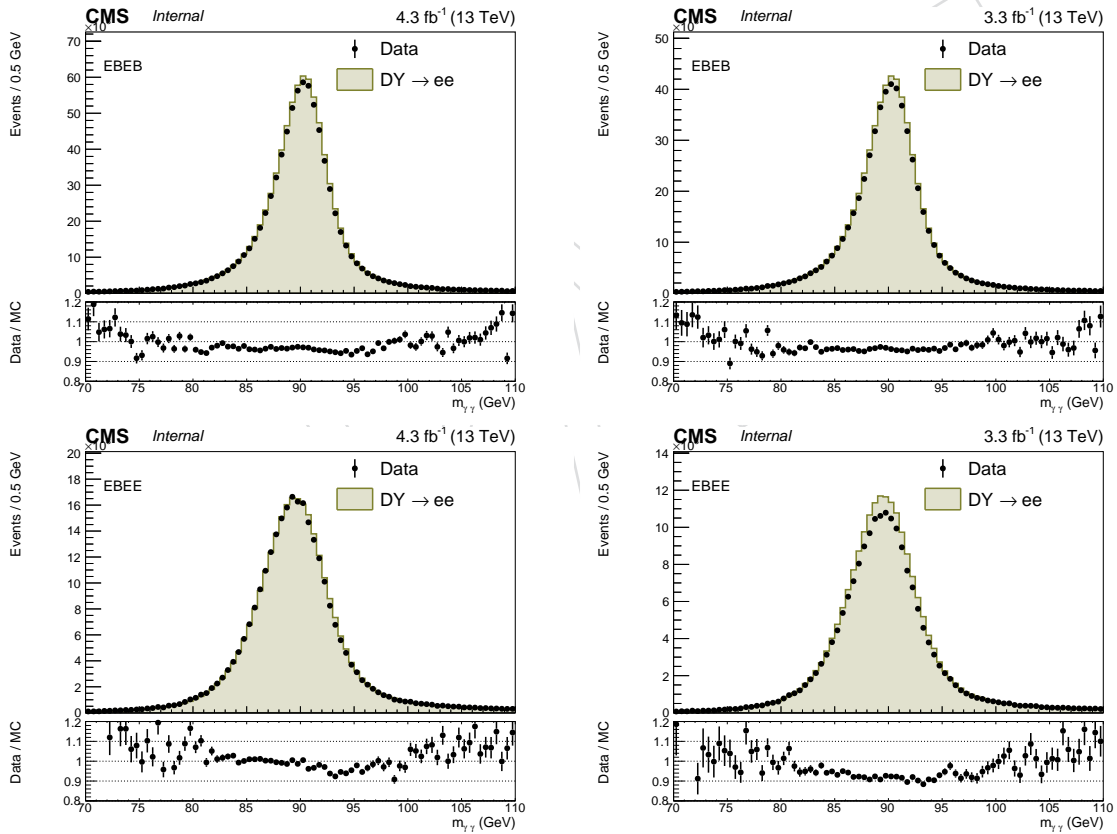
932 The efficiency scale factors have not yet been finalized. From preliminary results, the efficiency
 933 scale factors are roughly 1% lower (for each leg) in the 3.3 fb^{-1} dataset, compared to the 4.3 fb^{-1}
 934 one. This is however not yet taken into account in the following plots (here the scale factors

process	$m_{\gamma\gamma} > 230 \text{ GeV}$	$m_{\gamma\gamma} > 320 \text{ GeV}$	$m_{\gamma\gamma} > 500 \text{ GeV}$	$m_{\gamma\gamma} > 500 \text{ GeV}$
	EBEB N_{ev}	EBEE N_{ev}	EBEB N_{ev}	EBEE N_{ev}
data	1623 ± 40	748 ± 27	121 ± 11	211 ± 15

Table 24: Observed number of events in the two analysis categories.

935 obtained on 4.3 fb^{-1} are applied everywhere).

936 The invariant mass distributions observed for $Z \rightarrow e^+e^-$ events in data and simulation are
937 shown in Fig. 68. To obtain this plot the HLT_Ele27_WPloose trigger was used in data and
938 the simulation normalization was corrected for the efficiency of the trigger measured using the
939 tag and probe technique. A roughly 5% normalization correction was applied to the simulation
940 prediction in the 3.3 fb^{-1} dataset to account for the fact that the path was prescaled in the last
941 part of the data-taking period. The overall normalization agrees between data and MC within
942 roughly 3%, in all cases except for the EBEE category in the new data, and a good modelling
943 of the dielectron mass distributions can be observed, which allows to validate the energy scale
944 and resolution corrections.

Figure 67: Invariant mass distribution of dielectron events: 4.3 fb^{-1} (top) and 3.3 fb^{-1} (bottom). Events are split accordingly to the analysis categories: EBEB (left) and EBEE (right).

- 945 The number of events observed in the diphoton in the 3.3 fb^{-1} sample can be found in Tab. 24
946 and it is found to be compatible with what observed in the first 4.3 fb^{-1} within uncertainties.
947 The fit to the diphoton mass spectra observed in the 7.6 fb^{-1} dataset is shown in Fig. 69.
948 The expected upper limits obtained on the 7.6 fb^{-1} dataset are shown in Fig. 59.

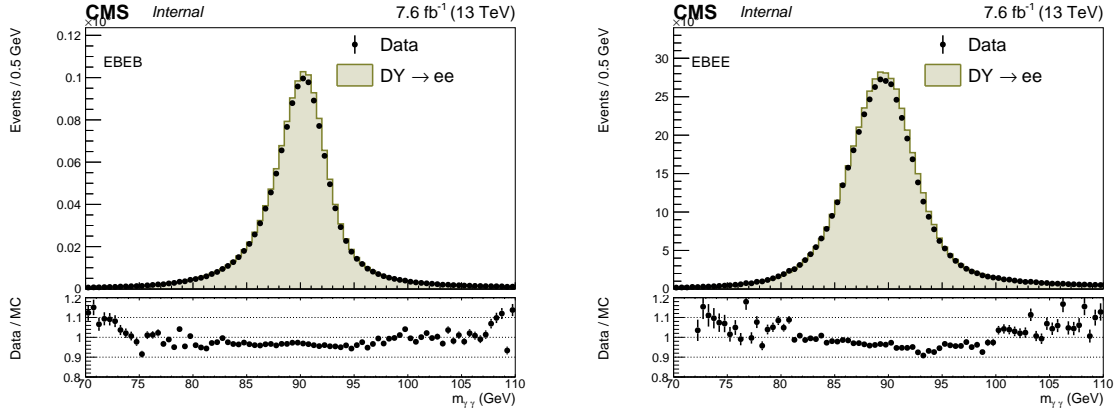


Figure 68: Invariant mass distribution of dielectron events in 7.6 fb^{-1} . Events are split accordingly to the analysis categories: EBEB (left) and EBEE (right).

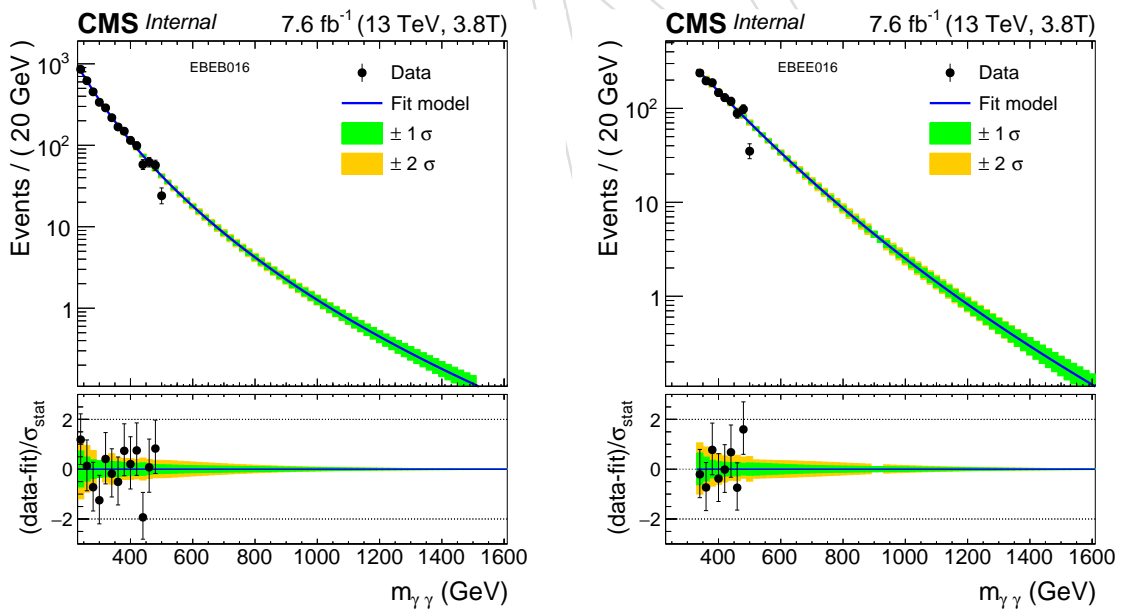


Figure 69: The fit to the diphoton mass spectra observed in the 7.6 fb^{-1} dataset. The region $m_{\gamma\gamma} > 500 \text{ GeV}$ is still blind. Left and right plots correspond to the EBEB and the EBEE categories respectively.

949 C Comparison of control plots with 2015 results

950 In this appendix we compare some of the main inputs to the analysis between the 2015 and
 951 2016 datasets, to facilitate the understanding of analogies and differences. The 2015 plots are
 952 extracted either from the AN documenting Moriond results [18] or from the one prepared for
 953 the December jamboree [17]. In the following all the figures show the 2015 distribution (left)
 954 and the equivalent 2016 one (right). These comparisons are based on 4.3 fb^{-1} of 2016 data.

Fig. 70 and 71: Data-MC comparison of the diphoton invariant mass distribution

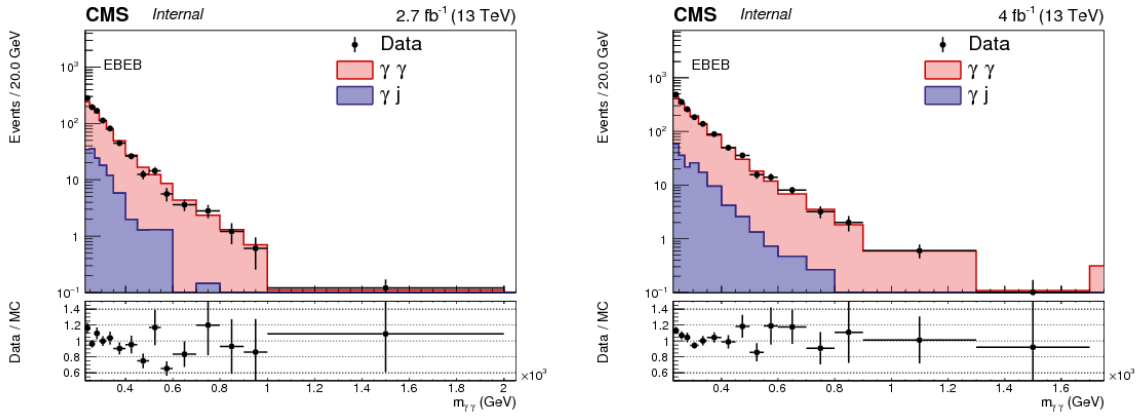


Figure 70: Data-MC comparison of the diphoton invariant mass distribution for the EBEB category. The Montecarlo predictions are rescaled by a factor 1.4 to account for higher order effects. 2015 data: [18]

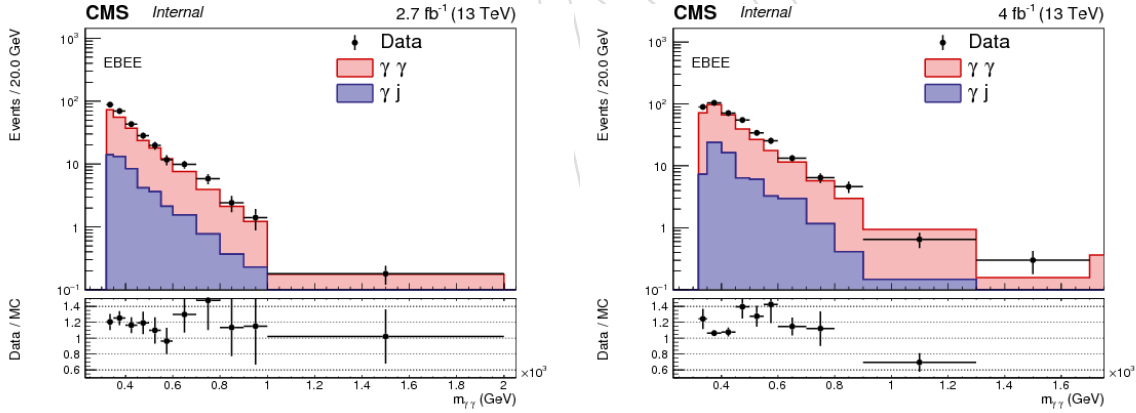


Figure 71: Data-MC comparison of the diphoton invariant mass distribution for the EBEE category. The Montecarlo predictions are rescaled by a factor 1.4 to account for higher order effects. 2015 data: [18]

Fig. 72 and 73: HLT efficiency computed with the tag-and-probe technique

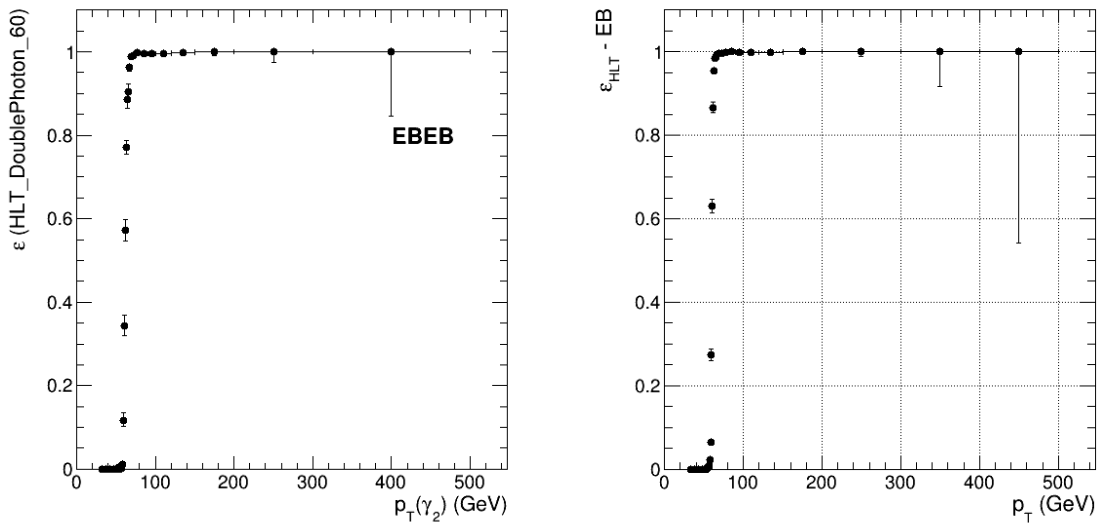


Figure 72: Efficiency for the HLT_DoublePhoton_60 bit to fire in di-electron events where the reference trigger has fired. The reference trigger is SingleEle_35_WP Loose_Gsf for the 2016 dataset, and HLT_Ele27_eta2p1_WP75_Gsf for 2015. Events with both electrons in the barrel. 2015 data: [17]

956

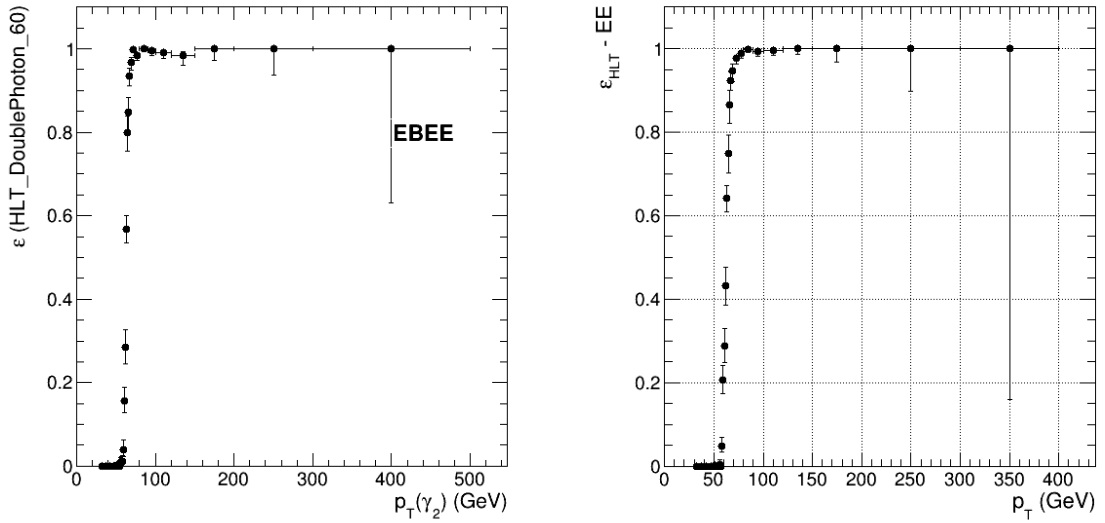


Figure 73: Efficiency for the HLT_DoublePhoton_60 bit to fire in di-electron events where the reference trigger has fired. The reference trigger is SingleEle_35_WP Loose_Gsf for the 2016 dataset, and HLT_Ele27_eta2p1_WP75_Gsf for 2015. Events with one electron in the barrel and one in the endcaps. 2015 data: [17]

957 Fig. 74 and 75: Selection efficiency computed with the tag-and-probe technique

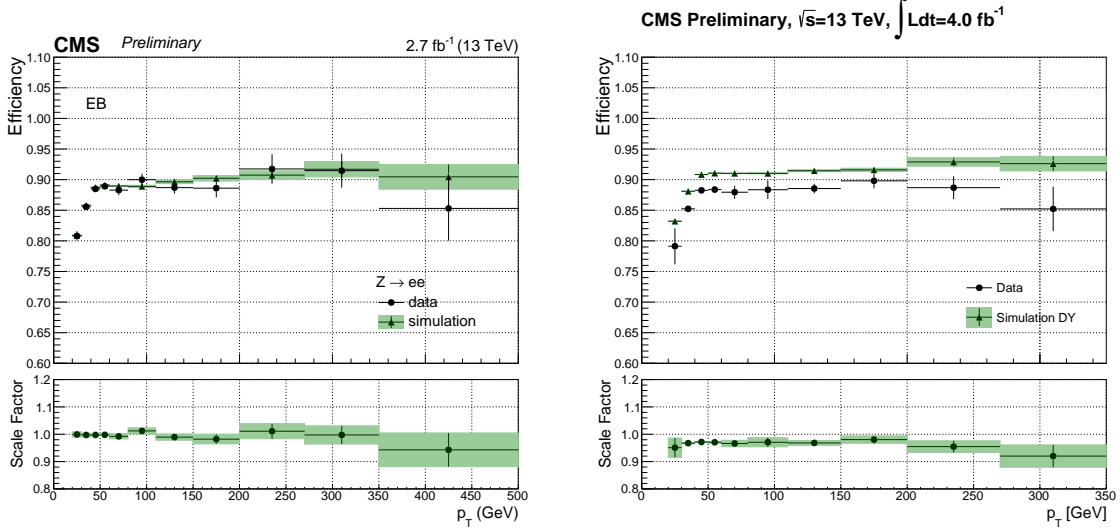


Figure 74: Top: Photon selection efficiency measured in barrel using the tag and probe method (all cuts except for electron rejection). Statistical and systematic errors are shown. Bottom: data over Montecarlo scale factors. 2015 data: [18]

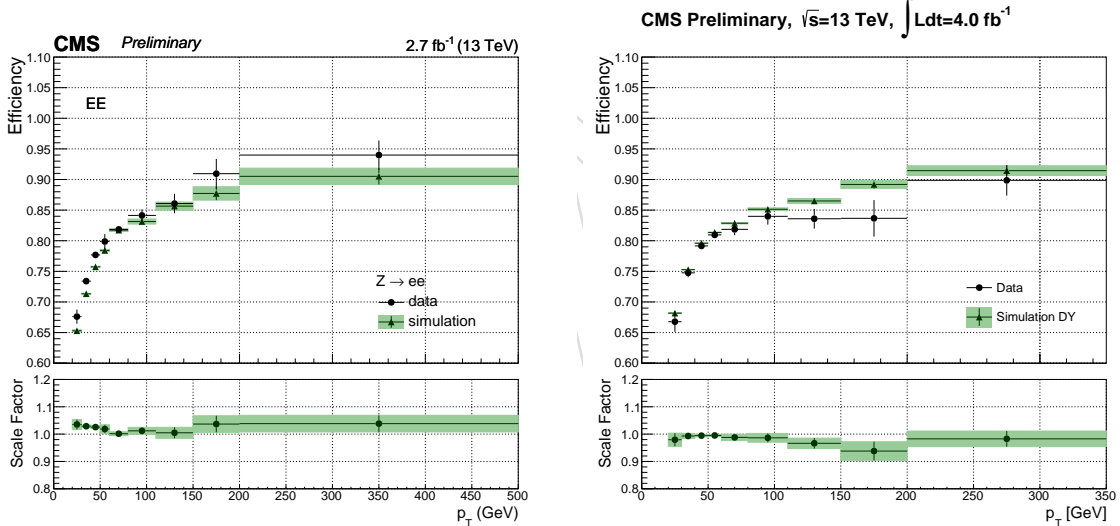


Figure 75: Top: Photon selection efficiency measured in endcaps (for 2016 up to $|\eta| < 2.1$) using the tag and probe method (all cuts except for electron rejection). Statistical and systematic errors are shown. Bottom: data over Montecarlo scale factors. 2015 data: [18]

958 Fig. 76 and 77 Background composition in the signal region ($\text{Iso}_{\text{Ch}} < 5 \text{ GeV}$) in data

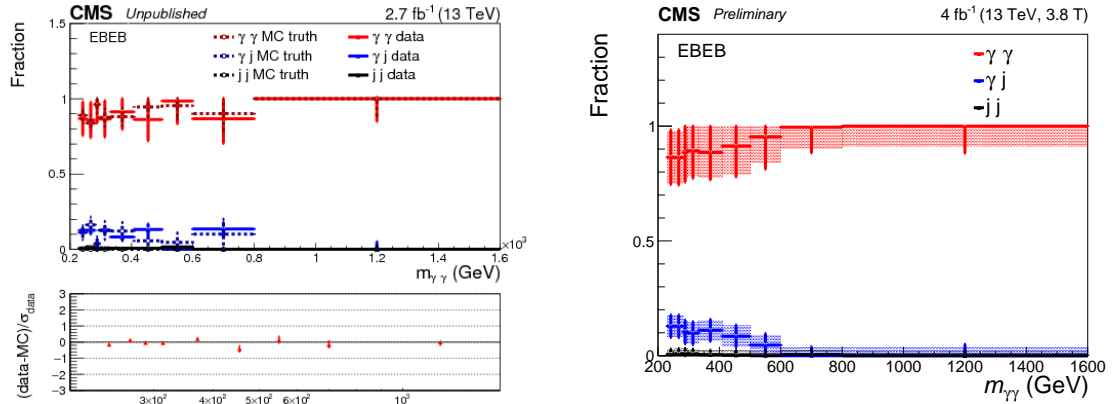


Figure 76: Fraction of the background components for $\text{IsoCh} < 5 \text{ GeV}$ to the overall background in data for EBEB. 2015 data: [18]

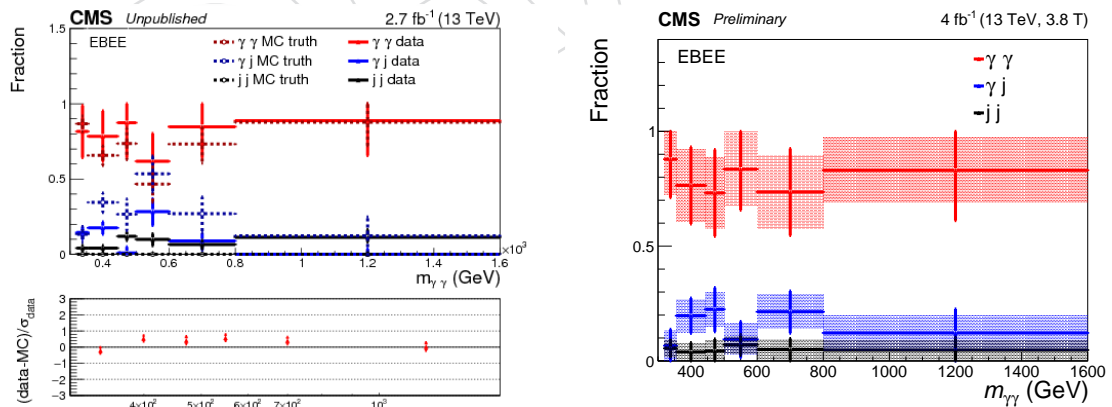


Figure 77: Fraction of the background components for $\text{IsoCh} < 5 \text{ GeV}$ to the overall background in data for EBEE. 2015 data: [18]

959 **D Comparison between the first 2.6 fb^{-1} the subsequent 1.4 fb^{-1}**

- 960 The analysis results were unblinded in two steps: first a dataset corresponding to 2.6 fb^{-1} was
961 analysed and then a 1.4 fb^{-1} dataset was added.
962 The $Z \rightarrow ee$ control sample was used to check the consistency of the energy corrections and
963 efficiency selection scale factors between the first 2.6 fb^{-1} and the following 1.4 fb^{-1} . The agree-
964 ment in both datasets is good between data and simulation (Figure 78).

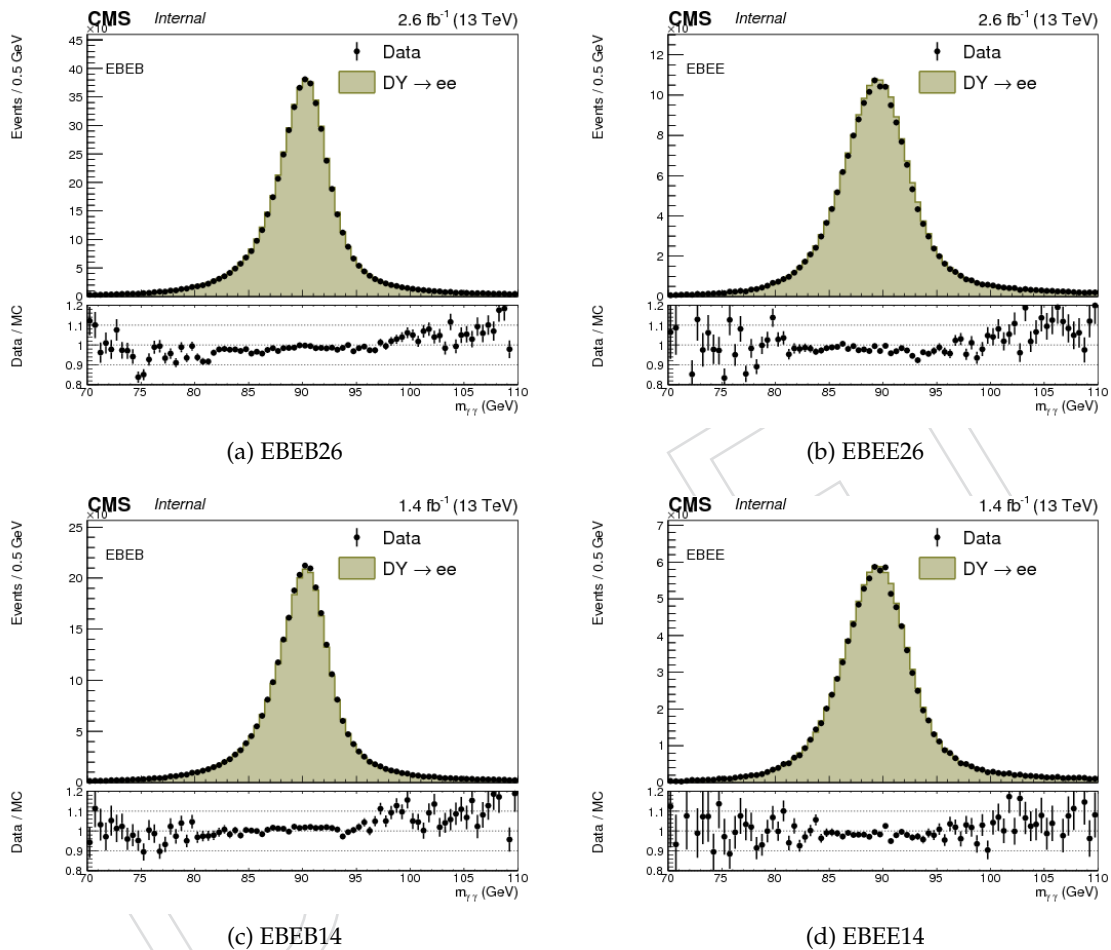


Figure 78: Invariant mass distribution of dielectron events: 2.6 fb^{-1} (top) and 1.4 fb^{-1} (bottom). Events are split accordingly to the analysis categories: EBEB (left) and EBEE (right).

- 965 The diphoton mass spectra observed in the two datasets are shown in Figures 79 and 80.

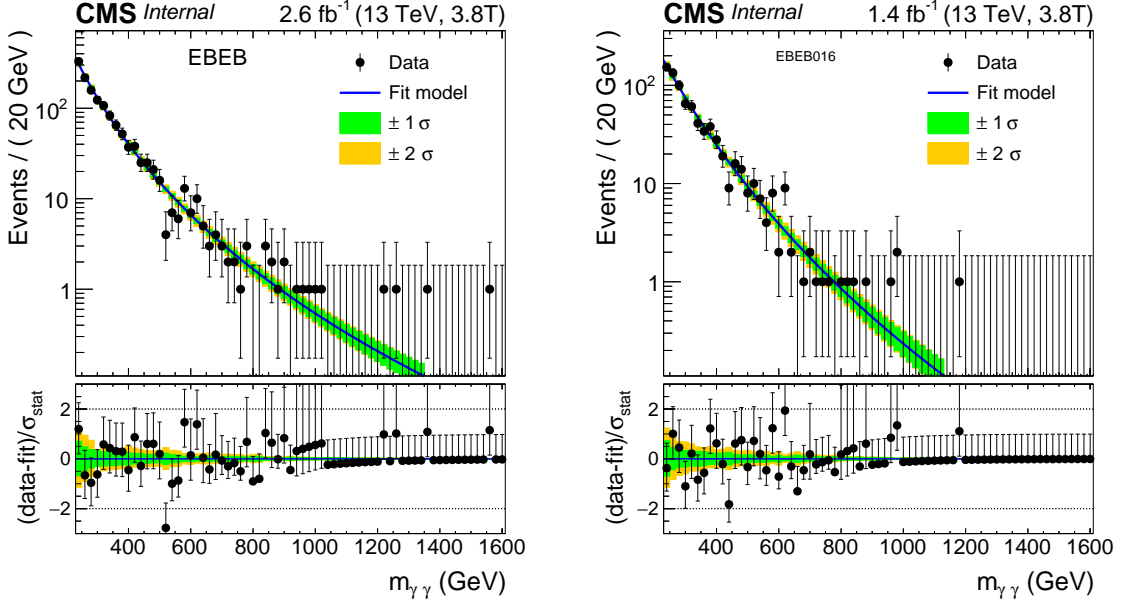


Figure 79: Observed mass spectrum in the EBEB category in the 2.6 fb^{-1} and 1.4 fb^{-1} datasets. The result of the parametric fit is superimposed to the points, together with bands representing the statistical uncertainties on the knowledge of the background shape.

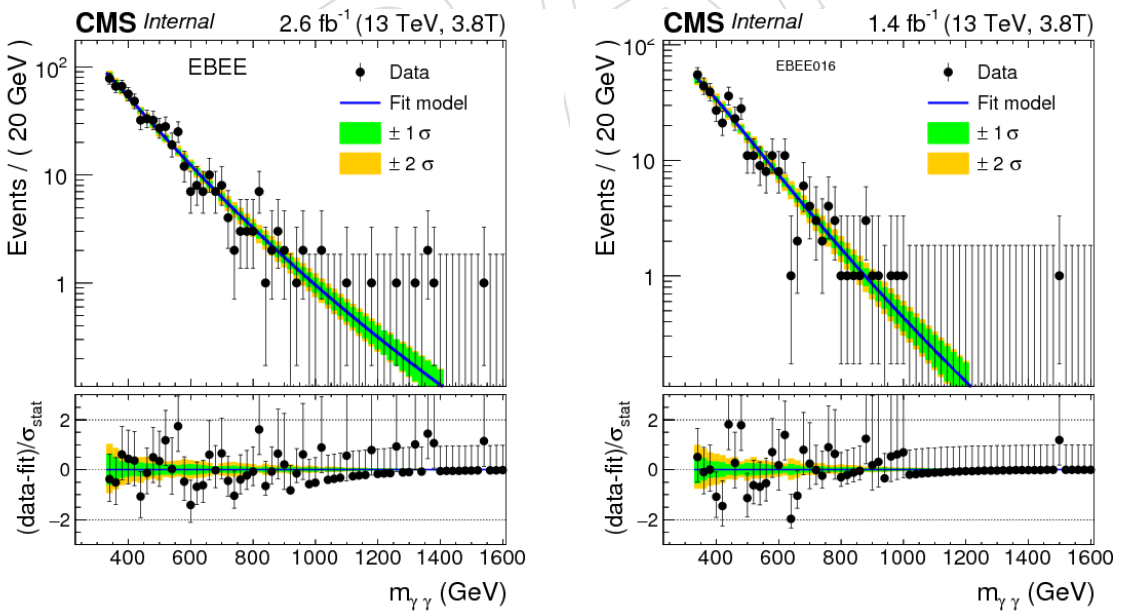


Figure 80: Observed mass spectrum in the EBEE category in the 2.6 fb^{-1} and 1.4 fb^{-1} datasets. The result of the parametric fit is superimposed to the points, together with bands representing the statistical uncertainties on the knowledge of the background shape.

966 E Analysis optimization studies

967 In this appendix, two studies are discussed that attempt to change the analysis selection or
 968 categorization in order to optimize the expected significance. The first concerns the use of the
 969 photon ID MVA from the Standard Model Higgs to diphoton analysis; this yields no improve-
 970 ment in performance, which is consistent with expectations as discussed in Section E.1. The
 971 second concerns the possibility of using the Collins Soper angle θ^* , which is predicted to have
 972 different distributions for the Graviton and spin-0 hypotheses, and for background [26]; this
 973 study investigates improving discrimination of one spin hypothesis or the other against the
 974 background. This study yields improvements of up to 2-5% in the expected significance, de-
 975 pending on the spin and width of the resonance, and suggests further avenues for study of
 976 significance or spin separation.

977 The baseline for both studies is 10fb^{-1} of simulated 2016 events, performing shape-based fits
 978 rather than constructing signal models, for which the expected significance is 4.83σ .

979 E.1 Photon ID MVA

980 For the narrow width graviton, the usual diphoton selection is replaced with cuts on the MVA
 981 trained for [27]. The significance as a function of MVA cut is shown in Figure 81. The expected
 982 significance is very similar to the baseline of 4.83σ for the middle range of values, but becomes
 983 lower for very tight or very loose cuts. This can be understood because the baseline cuts and
 984 mid-range cuts are both quite loose for real photons, and the background is dominated by real
 985 photons. For very high ID MVA cuts, both signal and background are lost; for very low ID
 986 MVA cuts, the ID is so loose that jet fakes increase.

987 E.2 Spin Studies

988 For each of six samples, with two spin hypotheses and three widths, the analysis is run with
 989 the existing categorization and with the EBEB category split into two categories with a cut at
 990 $|\cos(\theta^*)| = 0.5$. The results are shown in Table 25; it has been checked that the improvement is
 991 not a strong function of the expected significance by changing the luminosity. This yields im-
 992 provements of up to 2-5% in the expected significance with 10fb^{-1} , depending on the spin and
 993 width of the resonance. Better separation is obtained for spin-0 than Gravitons, because the dis-
 994 tributions of $\cos(\theta^*)$ after reconstruction are more similar between Graviton and background
 995 than between spin-0 and either, as illustrated in Figure 82.

996 Further studies could yield better performance by:

- 997 1. optimizing the $|\cos(\theta^*)|$ cut;
- 998 2. splitting the EBEB category by the $|\eta|$ of the leading and subleading photon , which is
 999 correlated with $\cos(\theta^*)$ and with expected photon resolution;
- 1000 3. investigation of correlations with the p_T of the diphoton system (or equivalently $\Delta\phi$).

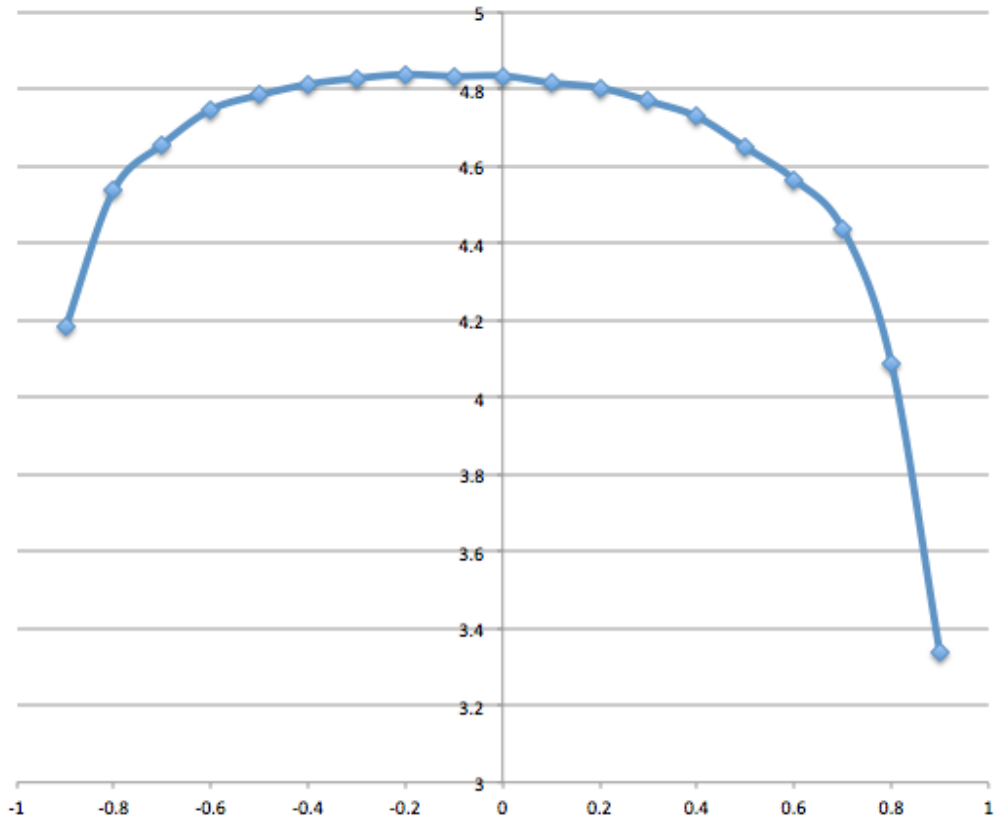


Figure 81: Significance of the analysis as a function of Photon ID MVA cut, compared with a baseline of 4.83σ for the standard analysis.

Table 25: Results yielded by changing the categorization using $|\cos(\theta^*)|$ as described in the text.

Signal	Baseline	$ \cos(\theta^*) $ Cut	Improvement
Graviton $k=0.01$	4.83σ	4.83σ	0%
Graviton $k=0.1$	3.97σ	3.80σ	0.3%
Graviton $k=0.2$	2.57σ	2.63σ	2.3%
spin-0 width=0.014	4.66σ	4.81σ	3.2%
spin-0 width=1.4	3.05σ	3.63σ	3.7%
spin-0 width=5.6	3.63σ	2.34σ	5.4%

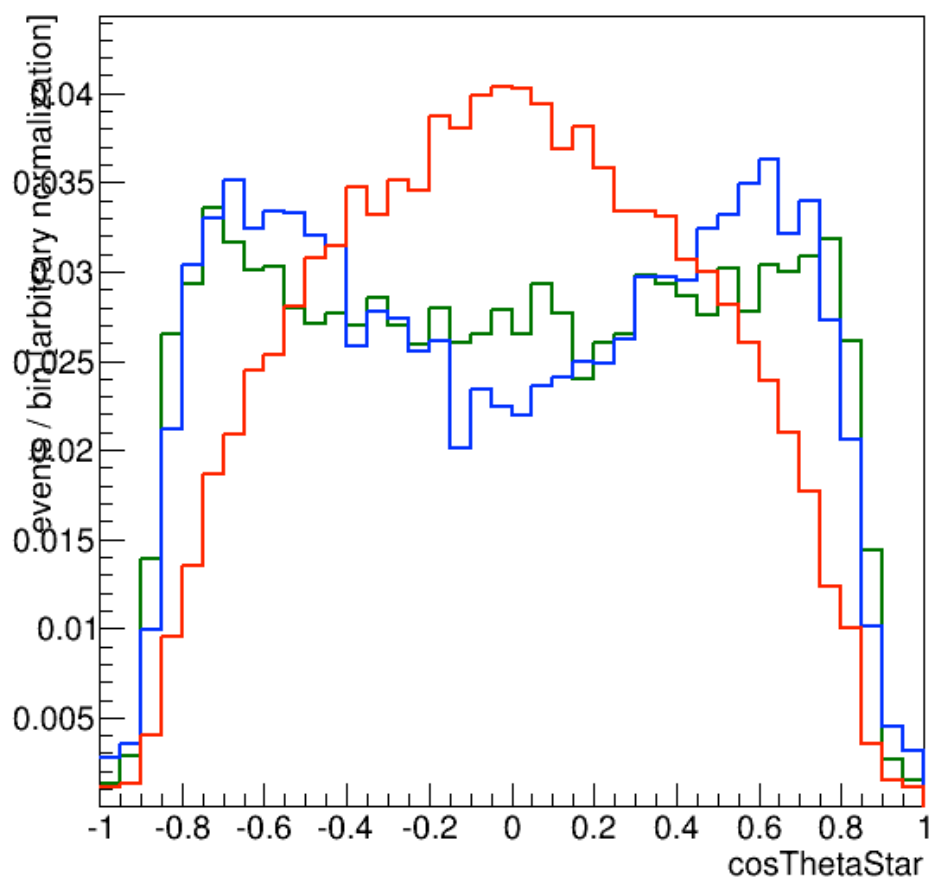


Figure 82: Distributions of $|\cos(\theta^*)|$ for simulated graviton signal (blue), spin-0 signal (red), and background (green). The samples are narrow-width.

F Further studies on the background model accuracy

F.1 Alternative background parametrization

In addition to the chosen background parametrization following

$$g(m_{\gamma\gamma}) = m_{\gamma\gamma}^{a+b \log(m_{\gamma\gamma})}$$

an alternative background model has been studied. The alternative parametrization is defined as

$$g'(m_{\gamma\gamma}) = \left(\frac{m_{\gamma\gamma}}{\sqrt{s}}\right)^a + \left(1 - \left(\frac{m_{\gamma\gamma}}{\sqrt{s}}\right)^b\right)^c$$

and is shown in Fig. 83. The bias study described in Sec. 10.1 was repeated for this functional form and the results are described below.

Figure 84 shows the median of the pull test statistics

$$b^j = |\text{median}(p_i^j)|$$

for the set of test-regions w_j listed in Table 18. The pull shows a larger disagreement between the number of events predicted by the fits to the pseudo-datasets $N_{\hat{g}_i}^{w_j}$ and the ones of the true underlying distribution $N_h^{w_j}$ compared to the chosen background parametrization.

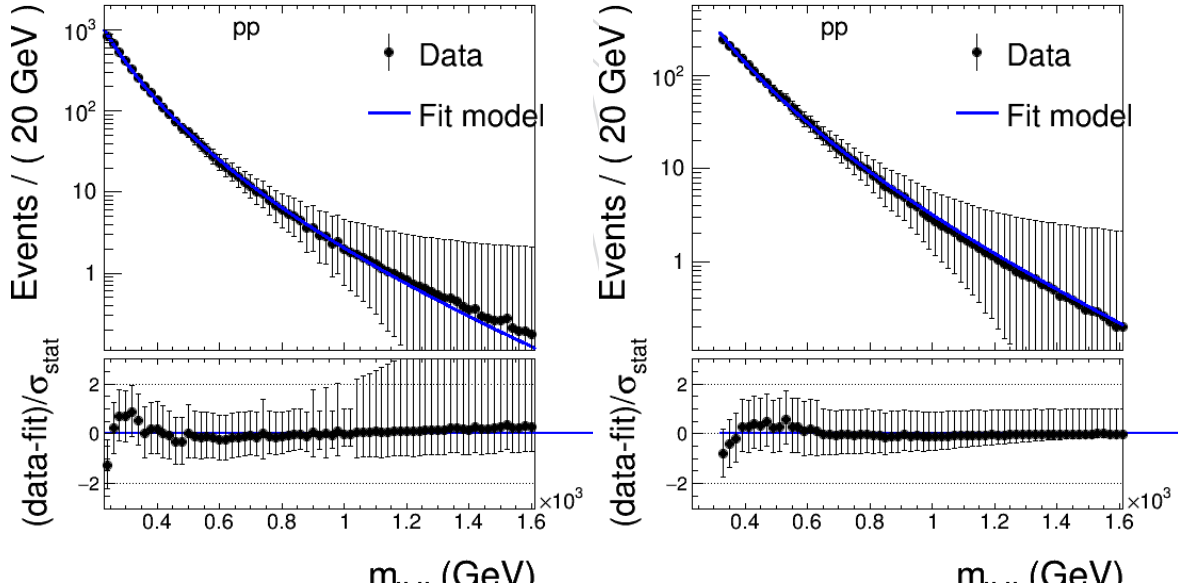


Figure 83: Fit to $\gamma\gamma$ MC spectrum, for the EBEB (left) and for the EBEE category (right) with the background parametrization $g'(m_{\gamma\gamma})$, specified in the text. The statistical uncertainty is reflecting the expected uncertainty in data for 10 fb^{-1} .

F.2 Alternative bias parametrization

An alternative bias parametrization and its impact on the final sensitivity is studied in the following section. The same true underlying distribution $h(m_{\gamma\gamma})$ and the same unbinned maximum likelihood fits to the pseudo-datasets $\hat{g}_i(m_{\gamma\gamma})$ as for the chosen bias parametrization in section 10.1 are used. In several mass windows w_j , the number of events $N_{\hat{g}_i}^{w_j}$ of $\hat{g}_i(m_{\gamma\gamma})$ are

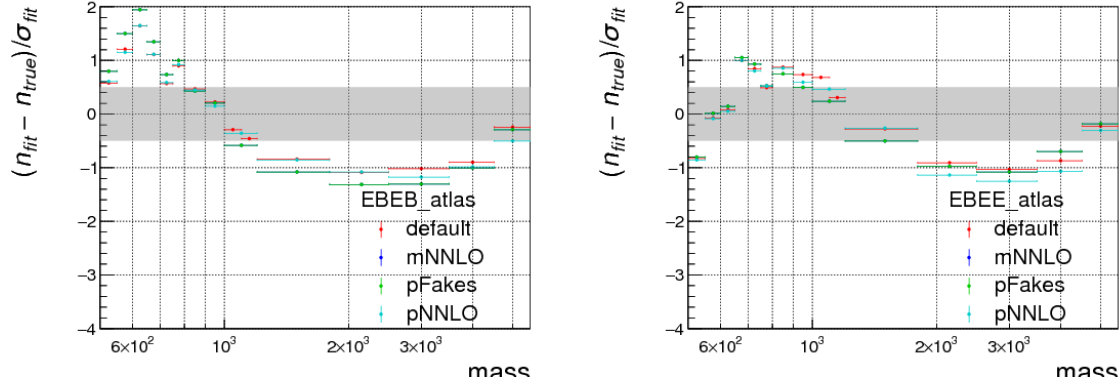


Figure 84: Median of the pull p^j for the alternative fit function for all the considered test regions according to Tab. 18 for EBEB (left) and EBEE (right). Different datasets correspond to different MC shape variations as specified in section 10.1.

compared to the predicted number of events $N_h^{w_j}$ of $h(m_{\gamma\gamma})$. The bias parametrization is considered accurate when it describes correctly the maximum difference

$$d_{max}^j = |\text{median}(\max(N_{\hat{g}_i}^{w_j} - N_h^{w_j}))|$$

for all mass windows w_j . The maximum difference takes all studied variations of the MC shape into account (see section 10.1 for more details). The resulting profile for two different sets of test regions (Table 18 and Table 16 respectively), are depicted in Figure 85.

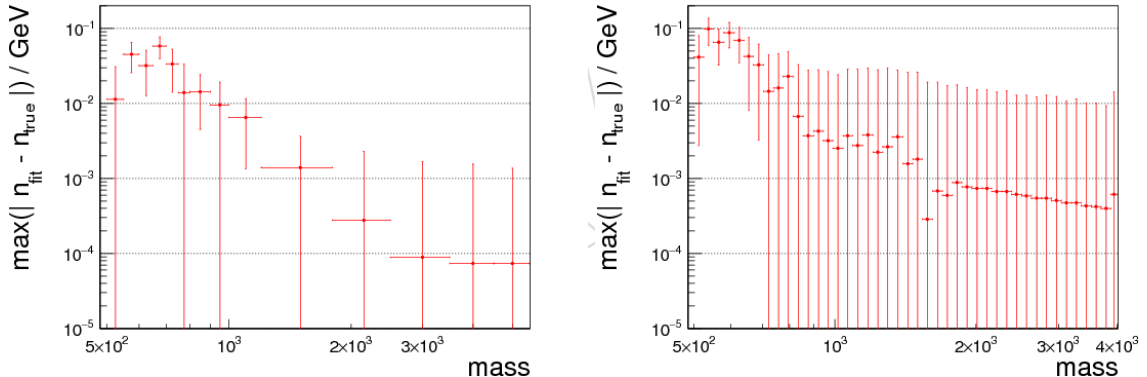


Figure 85: Profile of the maximum difference d_{max}^j for the set of test regions of Table 18(left) and Table 16 (right) for the EBEB category.

1012 F.2.1 Effect of the bias term on the analysis sensitivity

1013 For this preliminary study, only the EBEB category was parametrized with the alternative ap-
 1014 proach as this category has the largest impact on the final sensitivity (see section 13, Figure 58).
 1015 For the EBEE category, the bias term derived in section 10.1 and listed in Table 19 is used. Ta-
 1016 ble 26 shows the median expected limit using the alternative bias parametrization, compared
 1017 to the one applying no bias term at all. The worsening of the sensitivity due to the bias term is
 1018 reduced by roughly 50% compared to the chosen bias parametrization in Table 22.

$m_{\gamma\gamma}$ (GeV)	Γ/M (%)	exp.limit (fb) with bias	exp.limit (fb) without bias	difference (%)
500	0.014	3.18	3.06	4
	5.6	6.16	5.88	5
750	0.014	1.56	1.54	1
	5.6	3.18	3.06	4
1000	0.014	0.96	0.96	< 1
	5.6	1.76	1.75	< 1
3000	0.014	0.31	0.31	< 1
	5.6	0.35	0.35	< 1

Table 26: Comparison of the median expected upper limit on the signal strength for the narrow and large width hypotheses for the Spin-2 hypothesis using the alternative bias parametrization.

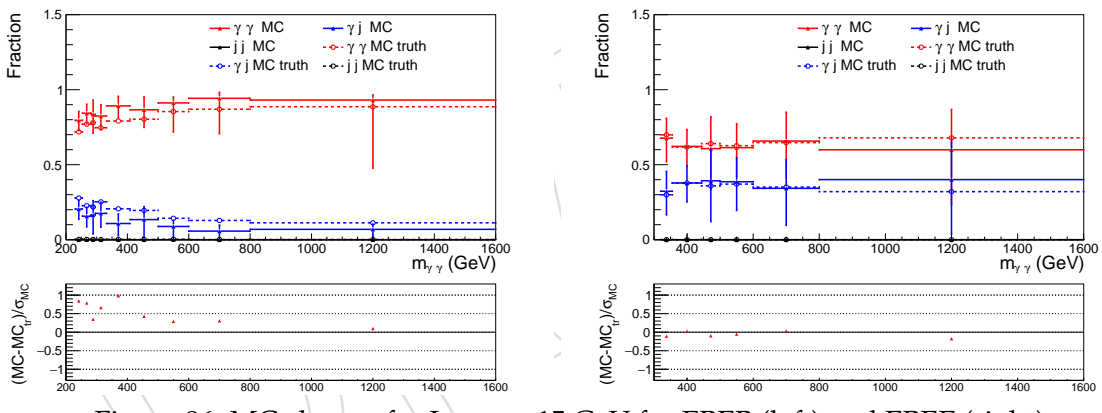
1019 G Systematic uncertainties for the background control

1020 This section lists the systematic uncertainties for the background control (section 7) which
 1021 were derived in Ref. [17] and are part of the final systematic uncertainty of the individual
 1022 background fractions.

1023 G.1 Closure in Monte-Carlo dataset

1024 To verify the method, a closure test, with MC truth and the charged particle flow isolation
 1025 templates built from MC, is performed for the extended Iso_{Ch} range ($\text{Iso}_{\text{Ch}} < 15 \text{ GeV}$). The
 1026 result is depicted in Figure 86 for both categories. The bottom plot depicts the pull-function
 1027 of the $\gamma\gamma$ -MC purity values. The MC truth fraction is derived by fitting the above MC truth
 1028 templates. No uncertainty is added for the MC truth fractions as the exact value of each fraction
 1029 is known and verified with the MC dataset. The background fractions derived by MC templates
 1030 are depicted with their fit uncertainty. The MC truth and MC fractions agree within their errors.
 1031 The difference in scale of the two $\gamma\gamma$ -components in MC and MC truth is one of the most
 1032 dominant systematics and listed in Table 27. The general overestimation of the $\gamma\gamma$ component
 1033 in MC for EBEB (Figure 86) is being investigated.

1034 The method closes within a bias of 7% for EBEB and 5% for EBEE. The statistics for the MC
 1035 datasets are too poor to create a jj -template due to the missing QCD-EM enriched MC samples.
 1036 Thus, the fit on MC truth and MC templates is a two component fit, in contrast to the three
 component fit for data.



1037 Figure 86: MC closure for $\text{Iso}_{\text{Ch}} < 15 \text{ GeV}$ for EBEB (left) and EBEE (right).

1038 G.2 Bias of templates construction due to statistical limitations

1039 The construction of the charged particle flow isolation templates is statistically limited as men-
 1040 tioned above. To estimate this bias, the uncertainty on the template shape is calculated via the
 1041 "jackknife resampling" method and was performed in Ref [17]. The method can be applied to
 1042 estimate the variance of statistical estimators and it proceeds as follows: given an estimator Θ
 1043 and a data sample of n entries, several pseudo-samples $s(j)$ are extracted. Each pseudo-sample
 1044 contains all the events in s except for a subset of size d . Each pseudo sample is generated such
 1045 that each event is removed once and only once. A total number of events g , with $g = n/d$, can
 1046 be extracted in this way. The estimator Θ is then evaluated on each pseudo sample and the
 1047 corresponding values are labelled as $q(j)$.

$$1048 \text{var}_J(\Theta) = \frac{g-1}{g} \sum_{j=1}^g \cdot (\bar{\Theta} - \Theta_j)^2 \text{ where } \bar{\Theta} = \frac{1}{g} \sum_{j=1}^g \cdot (\Theta_i) \quad (9)$$

In this study, this jackknife-method is used to estimate the variance of the $\gamma\gamma$ -fraction and γj -fraction for each mass bin. For the $\gamma\gamma$ -templates $g = 10$ pseudo samples with 90% of the overall data events are fitted to data with the nominal γj and jj component.

For the γj -templates the event mixing has to be taken into account. To describe the statistical limitation of the diphoton dataset, taken as input for the mixing, 10 pseudo samples are created. Additionally, 10 pseudo samples are created from the single photon data set. The γj -pseudosamples are subsequently fitted to data with the nominal $\gamma\gamma$ and jj templates in data. The jj -component is not regarded for this error as the number of events are negligible. For each fit, the final $\gamma\gamma$ -fraction is taken and the variance over all entries calculated according to equation 9. The final variance is then taken as an additional statistical error, describing the statistical limitation of the charged particle flow isolation templates.

The full statistical error is then the square root of the sum in quadrature of the statistical error in data and the total ‘jackknife’ error.

$$\sigma_{tot,stat} = \sqrt{var_{JK} + var_{stat}} \quad (10)$$

1048 G.3 Systematic error on background fractions

1049 The most dominant error for the systematic uncertainty comes from the MC non-closure. The
 1050 bias from the closure test is averaged over all mass bins as the statistics of the γj -samples are
 1051 limited and statistical fluctuations could be picked up if the systematics are included per mass
 1052 bin. The second dominant error is the bias which is created if the templates from the MC dataset
 1053 are fitted to the dataset of 7.6 fb^{-1} . The difference between data and MC is assumed to be 50%
 1054 of the difference when the MC templates are fitted to data. The latter is around 3% and taken
 1055 from Ref. [17]. As an additional check, the fit was performed on only two components, setting
 1056 the jj -component to zero. The results agree within their statistical uncertainty. In general,
 1057 the γj -component describes the jj -component sufficiently well. A full list of all considered
 systematical errors can be found in Table 27. In detail studied are the following systematics:

Table 27: Systematical errors for 7.6 fb^{-1} for $\gamma\gamma$ fraction of overall background in extended charged particle flow isolation range in EBEB and EBEE.

relative systematical error in %	barrel-barrel	barrel-endcap
bias from MC closure	7.5	4.2
template MC fit to data	2.5	3.4
variation of chIso bins	2.5	4.1
variation of kNN algorithm parameters	3.9	7.4
change of $\sigma_{inj\eta}$ cut	1.0	3.9
total systematical error	8.6	11.0

- 1058
- 1059 • the variation of the charged particle flow isolation bins from 9 to 4 bins in the 1-dimensional projection. The 4 bins have their boundary at 5 GeV for the charged
 1060 particle flow isolation of both photons.
 - 1061 • for the event mixing, the correlations between the two photons were varied by roughly 10% in each direction. The values were changed to 70% and 90% for EBEB and 50% and 60% for EBEE.
 - 1062 • the $\sigma_{inj\eta}$ cut was tightened to 0.012 for photons in the barrel and 0.035 for photons in
 1063 the endcaps.

1064 The systematic error, applied to each category, is the arithmetic mean of the systematic errors of
 1065 the mass bins. This is done, because some MC events have very high weights which could lead
 1066

¹⁰⁶⁹ to a non-physical mismatch in the final systematics if taken bin by bin. The sum in quadrature
¹⁰⁷⁰ of all errors lead to a total systematic error of 9% for barrel-barrel and 11% for barrel-endcaps.

DRAFT

1071 H Discrete profiling method for background modelling

1072 The study of the envelope method sensitivity is work in progress and we aim to finalize it
 1073 in time for the Icsep conference. If we manage in finishing it in time, we plan to use it as a
 1074 cross-check of the current strategy. We can eventually move to it in a second time, depending
 1075 on the performance.

1076 H.1 Introduction to the discrete profiling or ‘envelope’ method

1077 An alternative method to treat the background in this analysis is being considered, using a
 1078 strategy analogous to the one reported in the CMS $H \rightarrow \gamma\gamma$ analysis in [28] and [27], namely,
 1079 the discrete profiling or ‘envelope’ method [29].

1080 The discrete profiling method was designed as a way to determine the systematic uncertainty
 1081 associated with choosing a particular analytic function to fit to the background $m_{\gamma\gamma}$ distribu-
 1082 tion in the SM $H \rightarrow \gamma\gamma$ search. The method treats the choice of background function as a
 1083 discrete parameter in the likelihood fit used to produce the final results. The resulting system-
 1084 atic uncertainty is then calculated in an analogous way to systematic uncertainties associated
 1085 with other measurements. For this method to be valid, a complete set of candidate function
 1086 families should be considered. In practice, this analysis considered several families of analytic
 1087 functions:

- Sums of exponentials:

$$f_N(x) = \sum_{i=1}^N p_{2i} e^{p_{2i+1}x},$$

- Sums of polynomials (in the Bernstein basis):

$$f_N(x) = \sum_{i=0}^N p_i b_{(i,N)}, \text{ where } b_{(i,N)} := \binom{N}{i} x^i (1-x)^{N-i},$$

- Laurent series:

$$f_N(x) = \sum_{i=1}^N p_i x^{-4 + \sum_{j=1}^i (-1)^j(j-1)},$$

- Sums of power-law functions:

$$f_N(x) = \sum_{i=1}^N p_{2i} x^{-p_{2i+1}},$$

1088 where for all k , the p_k are a set of floating parameters in the fits.

1089 The method has been modified and adapted to the conditions of the high-mass diphoton reso-
 1090 nance search, in particular by adding four additional families of functions:

- ATLAS function

$$f(x; b; a_k) = (1 - x^{1/3})^b x^{\sum_{j=0}^k a_j (\log x)^j},$$

$$\text{eg } f(x) = (1 - x^{1/3})^{p_0} x^{p_1(\log x)^n + p_2(\log x)^{n+1}}$$

- Phenomenologically motivated modification to ATLAS function,

$$f(x; b; a_k) = (1 - x)^b x^{\sum_{j=0}^k a_j (\log x)^j},$$

$$\text{eg } f(x) = (1 - x)^{p_0} x^{p_1(\log x)^n + p_2(\log x)^{n+1}}$$

- Dijet function

$$f(x) = e^{(\sum_{i=0}^N p_i (\log(x))^i)},$$

1093 $\text{eg } f(x) = e^{(p_0 \log^n(x) + p_1 \log^{n+1}(x))}$

1094 • VV Dijet Function $f(x) = \frac{p_0(1-x/\sqrt{s})^{p_1}}{(x/\sqrt{s})^{p_2}}$

1095 $\text{eg } f(x) = \frac{p_0(1-x/\sqrt{s})^{p_1}}{(x/\sqrt{s})^{p_2}}$

1096 When fitting these functions to the background $m_{\gamma\gamma}$ distribution, the value of twice the negative
 1097 logarithm of the likelihood (2NLL) is minimized. A penalty is added to 2NLL to take into
 1098 account the number of floating parameters in each candidate function. Specifically, the penalty
 1099 is $c \times N_{\text{free}}$ parameters, where $c = 2$ was used for this analysis (this corresponds to the definition
 1100 of the Akaike Information Criterion). More details about the penalty term can be found in [29].
 1101 When making a measurement of some parameter of interest, the discrete profiling method
 1102 determines the envelope of the lowest values of 2NLL (with appropriate penalties) profiled
 1103 as a function of the parameter of interest. The envelope obtained through this method will
 1104 yield a broader curve than the 2NLL curve obtained from a single choice of function. The 1σ
 1105 uncertainty is then obtained by taking the width of the 68% range, or equivalently the points
 1106 where $\Delta 2\text{NLL} = 1$, of this wider curve.

1107 In order to perform the required fits for the discrete profiling method, a representative set of
 1108 functions within each family is selected. First, for a given family, the lowest order function in
 1109 that family is fit to a single category. Then, the next highest order function is fit to the data in the
 1110 same category and the difference $2\Delta NLL_{N+1} = 2(NLL_{N+1} - NLL_N)$, indicates whether or not
 1111 the data support the hypothesis of the higher order function. This is quantitatively expressed
 1112 using the fact that $2\Delta NLL_{N+1}$ should be distributed as a χ^2 with M degrees of freedom where
 1113 M is the difference in the number of free parameters in the $N + 1$ function and N function. For
 1114 example, for exponentials, $M = 4 - 2 = 2$, while for the polynomials $M = 3 - 2 = 1$. A p-value
 1115 is then calculated as

$$\text{p-value} = p(2\Delta NLL > 2\Delta NLL_{N+1} | \chi^2(M)).$$

1116 If the p-value is less than 0.05, the higher order function is supported by the data, meaning it
 1117 is included in the list of functions, and the procedure continues, testing the next ($N = 3$) order
 1118 function in the family. If however, the p-value is more than 0.05, the higher order function is
 1119 assumed too flexible given the data and the procedure terminates having found the highest
 1120 order suitable function. An additional constraint is applied to remove low order functions
 1121 which do not fit the data well. A goodness of fit is determined for each function using a χ^2
 1122 test statistic (calculated with the `RooPlot.chiSquare` function where the number of bins
 1123 is the same as for the fit). This is then converted to a p-value using the `TMath.Prob` function
 1124 where the number of degrees of freedom is taken to be the number of bins minus the number of
 1125 fitted parameters of the function (excluding the normalization term). The fits of these functions
 1126 which are included for each category are shown in Figure 87.

1127 The power of using the discrete profiling method is that in principle it should avoid the need to
 1128 include any additional systematic uncertainty associated with the bias term in the background
 1129 model, as described in Section 10.1, since the uncertainty associated with the choice of back-
 1130 ground function is then handled directly by the discrete profiling method.

1131 Extensive tests were made by the developers of the method and in the CMS $H \rightarrow \gamma\gamma$ analysis,
 1132 using pseudo-experiments. Such tests are described in [29]. To check that the method can safely

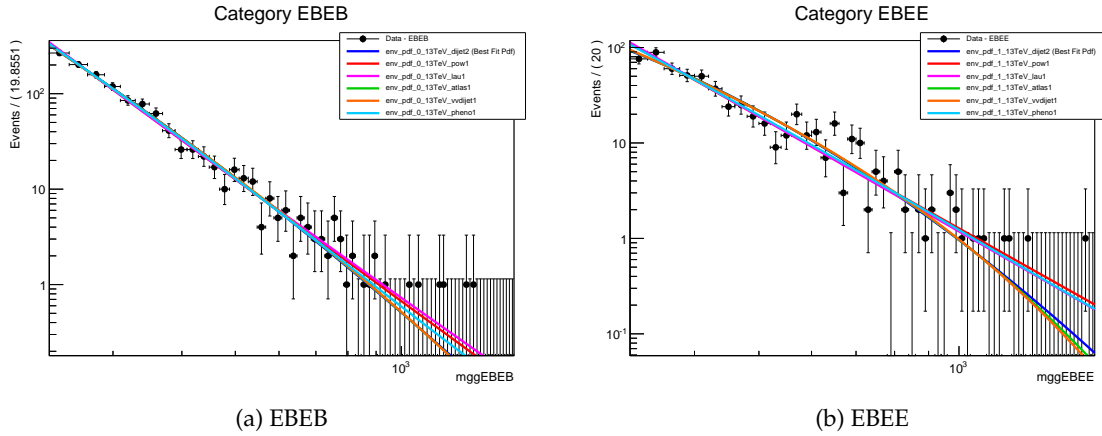


Figure 87: The set of functions chosen to fit the background using the discrete profiling method for each of the two categories considered in this analysis. An F-test is used to select what families of function should be included, and indeed which order from each of these families should be used in order to proceed with the discrete profiling. The choice of function to describe the background is treated as a discrete nuisance parameter in the final 2NLL minimization, and taking the minimum envelope naturally provides a systematic uncertainty on for the choice of function to describe the background. The data points correspond to the 2015 dataset used for the analysis documented in [17].

1133 be extended to the high-mass diphoton resonance search, some of the test were repeated, in
 1134 particular the bias study, although some modifications were needed in order to compare the
 1135 results to the established background method bias study in Section 10.1. This bias study is
 1136 described in Section H.2.

1137 H.2 Alternative bias study

The bias study described in [29] involved using many pseudo-experiments to estimate the bias introduced by fitting a dataset generated from various families of functions using the discrete profiling method. For each candidate function chosen for the discrete profiling method, a toy dataset was generated randomly from the shape of the function. A signal of a given amplitude μ_{true} was then also injected into the toy dataset. Next, a fit to this dataset was performed using either one of the fixed candidate functions or the envelope method. The measured value of the signal amplitude $\mu_{measured}$ was then extracted from the signal component of the fit. The pull is then defined as:

$$\text{pull} := \frac{\mu_{true} - \mu_{measured}}{\sigma_\mu},$$

1138 where σ_μ is the uncertainty on the value of $\mu_{measured}$ from the fit. This procedure was repeated
 1139 many times for various values of μ_{true} and separately using each candidate function as the
 1140 generator. In each case, the mean value of the pull was extracted and used to compare the
 1141 performance of various fitting functions and the envelope method. The result was that the
 1142 envelope systematically gave a bias almost as small as if one had used the function used to
 1143 generate the pseudo-data to perform the fit.

1144 However, this method of estimating the bias has some differences with the established method
 1145 described in Section 10.1. Two key differences in particular need to be addressed before the
 1146 methods can be compared. First, the established bias study used a MC background shape
 1147 normalized to data to generate the pseudo-experiments, while the envelope bias study used

candidate functions fitted to the data instead. Second, the established bias study used the number of background events in various $m_{\gamma\gamma}$ bins to estimate the bias, while the envelope bias study used the amplitude of a known injected signal to do the same.

In order to compare the two methods, the envelope bias study strategy was modified to more closely align itself to the established bias study. First, the same MC background distribution, normalized to the amount of data expected for an integrated luminosity of 10 fb^{-1} , was used to generate the pseudo-datasets for the bias study, in addition to usual checks using each candidate function to generate the pseudo-datasets. Specifically, the MC background used represents the prompt-prompt photon pairs in the background processed using CMSSW_7_4_X. In particular, the MC diphoton background was put into a finely binned histogram, and normalized to match the number of events expected in data. This histogram was then used as a shape from which to generate random pseudo-experiments for the study. Second, the difference in the definitions of the pull needed to be resolved. A proper method to compare the two approaches is still being developed, but as a first approximation, the median pull under the assumption of $\mu_{true} = 0$, i.e. no injected signal, is used to compare to the established bias study.

The results of the modified envelope bias study are shown in Figure 88, where the pseudo-datasets were generated using the normalized MC background shape. The results using other shapes to generate the pseudo-experiments lead to similar plots. In all cases, and for all signal mass hypotheses, using the envelope method introduces a negligible bias, typically somewhat smaller than the bias introduced using ‘dijet2’ alone.

H.3 Conclusions about the use of the Envelope method

The discrete profiling method naturally handles the systematic uncertainty associated with the choice of function to describe the background. It was designed for analyses searching for a peak above a continuously falling background, such as this one. The method, by construction, is therefore expected to yield a negligible bias compared to choosing a particular function. The results of the envelope method bias study indeed suggest that a negligible bias is introduced, as can be seen in Fig. 88. The envelope method is shown to produce a consistently smaller bias than the ‘dijet2’ function alone, regardless of the true shape from which the pseudo-experiments are generated (in particular, the normalized MC background shape). A method to fairly compare the results of the established bias study described in Section 10.1 is still under development.

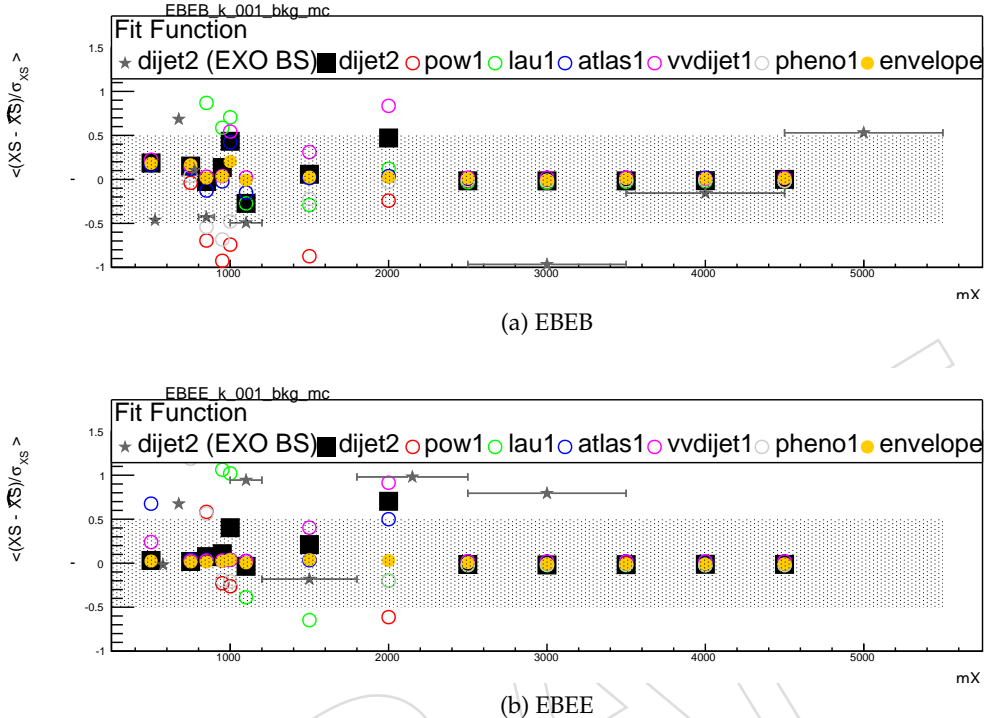


Figure 88: The average pull introduced by fitting pseudo-datasets generated randomly from the MC background shape normalized to the number of events expected from 10 fb^{-1} of data. The grey stars represent the established bias study performed using CMSSW_7_4_X using the ‘dijet2’ function. The black squares represent the bias study performed using the alternative method described in this section, in the case where no signal events were injected into the pseudo-datasets. The other points (red, green, purple, pink and orange circles) correspond to the result of the alternative bias study method described in this section using the various candidate functions selected for the envelope method (respectively power law of order 1, Laurent series of order 1, ATLAS function of order 1, VV-dijet function of order 1, the phenomenologically-motivated modification to the ATLAS function of order 1 and the full envelope method) to fit the background. In particular, the filled orange circle represent the results from the full envelope method. The results from the modified envelope bias study, for all functions are typically much closer to 0 than the established bias study. This suggests that further modifications are needed to make a fair comparison. None the less, the envelope method consistently yields a negligible bias for all signal mass hypotheses, as expected.

References

- [1] L. D. Landau, "The moment of a 2-photon system", *Dokl. Akad. Nauk SSSR* **60** (1948) 207.
- [2] C. N. Yang, "Selection Rules for the Dematerialization of a Particle into Two Photons", *Phys. Rev.* **77** (1950) 242, doi:10.1103/PhysRev.77.242.
- [3] N. Arkani-Hamed, S. Dimopoulos, and G. Dvali, "The Hierarchy problem and new dimensions at a millimeter", *Phys.Lett.* **B429** (1998) 263–272, doi:10.1016/S0370-2693(98)00466-3, arXiv:hep-ph/9803315.
- [4] L. Randall and R. Sundrum, "A Large mass hierarchy from a small extra dimension", *Phys. Rev. Lett.* **83** (1999) 3370–3373, doi:10.1103/PhysRevLett.83.3370, arXiv:hep-ph/9905221.
- [5] G. F. Giudice, R. Rattazzi, and J. D. Wells, "Quantum gravity and extra dimensions at high-energy colliders", *Nucl. Phys.* **B544** (1999) 3–38, doi:10.1016/S0550-3213(99)00044-9, arXiv:hep-ph/9811291.
- [6] E. A. Mirabelli, M. Perelstein, and M. E. Peskin, "Collider signatures of new large space dimensions", *Phys. Rev. Lett.* **82** (1999) 2236–2239, doi:10.1103/PhysRevLett.82.2236, arXiv:hep-ph/9811337.
- [7] T. Han, J. D. Lykken, and R.-J. Zhang, "On Kaluza-Klein states from large extra dimensions", *Phys. Rev.* **D59** (1999) 105006, doi:10.1103/PhysRevD.59.105006, arXiv:hep-ph/9811350.
- [8] J. L. Hewett, "Indirect collider signals for extra dimensions", *Phys. Rev. Lett.* **82** (1999) 4765–4768, doi:10.1103/PhysRevLett.82.4765, arXiv:hep-ph/9811356.
- [9] H. Davoudiasl, J. L. Hewett, and T. G. Rizzo, "Phenomenology of the Randall-Sundrum Gauge Hierarchy Model", *Phys. Rev. Lett.* **84** (2000) 2080, doi:10.1103/PhysRevLett.84.2080, arXiv:hep-ph/9909255.
- [10] N. Craig, J. Galloway, and S. Thomas, "Searching for signs of the second Higgs doublet", (2013). arXiv:1305.2424.
- [11] ATLAS Collaboration, "Observation of a new particle in the search for the Standard Model Higgs boson with the ATLAS detector at the LHC", *Phys. Lett.* **B716** (2012) 1–29, doi:10.1016/j.physletb.2012.08.020, arXiv:1207.7214.
- [12] CMS Collaboration, "Observation of a new boson at a mass of 125 GeV with the CMS experiment at the LHC", *Phys. Lett.* **B716** (2012) 30–61, doi:10.1016/j.physletb.2012.08.021, arXiv:1207.7235.
- [13] P. S. B. Dev and A. Pilaftsis, "Maximally symmetric two Higgs doublet model with natural standard model alignment", (2014). arXiv:1408.3405.
- [14] ATLAS Collaboration, "Search for resonances decaying to photon pairs in 3.2 fb^{-1} of pp collisions at $\sqrt{s} = 13 \text{ TeV}$ with the ATLAS detector", Technical Report ATLAS-CONF-2015-081, Dec, 2015.
- [15] CMS Collaboration, "Search for new physics in high mass diphoton events in 3.3 fb^{-1} of proton-proton collisions at $\sqrt{s} = 13 \text{ TeV}$ and combined interpretation of searches at 8 TeV and 13 TeV ", CMS Physics Analysis Summary CMS-PAS-EXO-16-018, 2016.

- [16] CMS Higgs to $\gamma\gamma$ Group, "Measurements of the Higgs boson at 125 GeV in the two photon decay channel in the Full LHC Run 1 Data at CMS", CMS Analysis Note 2013/253, 2013.
- [17] CMS diphoton EXOTICA Group, "Early search for new physics in the diphoton spectrum at high mass at 13TeV", CMS Analysis Note 2015/241, 2015.
- [18] A. Buccilli et al., "Update on the search for new physics in the diphoton spectrum at high mass at 13TeV", CMS Analysis Note 2016/079, 2016.
- [19] H. working group, "Further measurement of $H \rightarrow \gamma\gamma$ at $\sqrt{s}=13\text{TeV}$ ", CMS AN 2016-209, 2016.
- [20] M. Baak, S. Gadatsch, R. Harrington, and W. Verkerke, "Interpolation between multi-dimensional histograms using a new non-linear moment morphing method", *Nucl. Instrum. Meth. A* **771** (2015) 39, doi:10.1016/j.nima.2014.10.033, arXiv:1410.7388.
- [21] D. Anderson et al., "Search for High Mass Diphoton Resonances at 13 TeV using the 2015 dataset", CMS Analysis Note 2016/191, 2016.
- [22] ATLAS and CMS Collaborations, LHC Higgs Combination Group, "Procedure for the LHC Higgs boson search combination in Summer 2011", ATL-PHYS-PUB/CMS NOTE 2011-11, 2011/005, 2011.
- [23] G. Cowan, K. Cranmer, E. Gross, and O. Vitells, "Asymptotic formulae for likelihood-based tests of new physics", *Eur.Phys.J.* **C71** (2011) 1554, doi:10.1140/epjc/s10052-011-1554-0, 10.1140/epjc/s10052-013-2501-z, arXiv:1007.1727.
- [24] A. Buccilli et al., "Preparation for the search for the exotic production of di-photon pairs in pp collision at $\sqrt{s}=13\text{TeV}$ ", CMS Analysis Note 2015/098, 2015.
- [25] O. Charaf et al., "Updated combination of the results at $\text{sqrt}s=8\text{TeV}$ and 13TeV in the search for exotic production of di-photon pairs, TYPE =", technical report.
- [26] Y. Gao et al., "Spin determination of single-produced resonances at hadron colliders", *Phys. Rev.* **D81** (2010) 075022, doi:10.1103/PhysRevD.81.075022, arXiv:1001.3396.
- [27] CMS Collaboration, "First results on Higgs to $\gamma\gamma$ at 13 TeV", CMS Physics Analysis Summary CMS-PAS-HIG-15-005, 2016.
- [28] CMS Collaboration, "Observation of the diphoton decay of the Higgs boson and measurement of its properties", *Eur. Phys. J.* **C74** (2014), no. 10, 3076, doi:10.1140/epjc/s10052-014-3076-z, arXiv:1407.0558.
- [29] P. D. Dauncey, M. Kenzie, N. Wardle, and G. J. Davies, "Handling uncertainties in background shapes: the discrete profiling method", *JINST* **10** (2015), no. 04, P04015, doi:10.1088/1748-0221/10/04/P04015, arXiv:1408.6865.